Study of alkaline earth metals substitution in bismuth based mixed ion conductors

A

Thesis

Submitted for the award of degree of

Doctor of Philosophy

By

Samita

(Regn. No. 900912017)

Under the supervision of

Dr. Kulvir Singh
Professor

Dr. O. P. Pandey
Senior Professor

School of Physics and Materials Science

Thapar University, Patiala – 147004, Punjab

INDIA

July 2014

CERTIFICATE

This is to certify that the thesis entitled **"Study of alkaline earth metals substitution in bismuth based mixed ion conductors"** which is being submitted by Samita in fulfillment of the requirements for the award of the degree of Doctor of Philosophy in School of Physics and Materials Science, Thapar University, Patiala (Punjab), India is an exclusive record of candidate's own research work under our guidance and supervision. The thesis is part or in full has not been submitted in any other university or institute for the award of any degree. The thesis is fit to be considered for the award of degree of Doctor of Philosophy.

Dr. Kulvir Singh
Professor
School of Physics and Materials Science
Thapar University
Patiala-147004 (INDIA)

Dr. O.P. Pandey
Senior Professor
School of Physics and Materials Science
Thapar University
Patiala-147004 (INDIA)

ACKNOWLEDGMENT

In the name of God, most Gracious, most Merciful.

Working during my Ph.D. course of work has been a wonderful and enjoyable experience accompanied with trust, encouragement and hardships. At this moment of accomplishment, I wish to express my sincere thanks to those who have contributed to this thesis and supported me in one way or the other during this amazing journey.

First and foremost, I am deeply grateful to my supervisors Dr. Kulvir Singh and Dr. O. P. Pandey for their consistent guidance and useful discussions. This work would not have been possible without their guidance, support and encouragement. Their deep insights always helped me at various stages of my research work. I also remain indebted for their understanding and support during the times when I was really down and depressed due to personal problems. Dr. Kulvir Singh has always provided conducive atmosphere and insightful decisions for research. He has always been patient and encouraging in the time of new ideas and difficulties. I always admire his ability to balance research interest and personal pursuits. His personality has always inspired me. I hope that I could be as lively, enthusiastic and energetic like him. Dr. O. P. Pandey has constantly forced me to remain focused on achieving my goal. His observations and comments helped me to establish the overall direction of the research and to move forward with investigation in depth. His commitment towards research and his students will always inspire me.

I am profoundly obliged to Dr. B. N. Chudasama for his valuable suggestions and help during the various stages of my research work. I heartily owe my thanks to Ms. Loveleen Kaur Brar for her constant support and encouragement.

My thanks to Dr. K. K. Raina, Distinguished Professor, Thapar University, Patiala for his encouragement and personal attention during my work. I am also thankful to Dr. P. K. Bajpai and Dr. N. K. Verma for their whole hearted support and blessings.

I would like to express my thanks to my Doctoral committee members, Dr. K. K. Raina, Dr. Puneet Sharma and Dr. Amjad Ali for their helpful suggestions and criticism during my progress report presentations.

I would like to thank administrative and technical staff members of the school who have been kind enough to advise and help in their respective roles.

I gratefully acknowledge the financial assistance from Defense research development organization, New Delhi in the form of junior research fellow which buttressed me to perform work comfortably.

I would like to acknowledge Mr. Ganshyam Morya, SAI Lab, Thapar University and SAIF Centre Chandigarh for characterizations. I also thank to Mrs. Parveen Kumari, Mr. Vijay, Mr. Jant Singh, Mr. Purshottam, Mr. Mani for their help and support.

My special thanks to Dr. Ravi Shukla and Dr. Gurbinder Kaur who have always been a constant source of encouragement and moral support for me for academic and personal fronts. Dr. Gurbinder Kaur has always inspired me to work harder and achieve my goals.

It is my fortune to gratefully acknowledge the support of my friends Rajinder, Chandni, Suninder, Samiksha, Navjot, Sakshi, Pooja, Satwinder, Parveer, Purnima, Suresh Kumar, Parveen Jha, Gaurav Singla, Paramjyot Jha and Ranvir Panwar for their support, generous care and the homely feeling. Many thanks to Dr. Kamalpreet Kaur, Dr. Jasmeet Kaur, Dr. Bhupinder Kaur, Dr. Akshay Kumar, Mr. Sunil Arya, Mr. Kapil, Ms. Mani, Ms. Jagdeep for their help during initial stages of my work.

Words fail to express my deep sense of gratitude towards my mother Smt. Sudesh Kumari, my father Sh. Balbir Singh, my grandma Smt. Shanti Devi, my sister Shivani and my brother Navjot for their love, patience and encouragement throughout my research work.

Above all, I thank to almighty God for his grace, protection and blessings!!!!

Samita

INDEX

Contents *Page no.*

List of Figures

Contents Page no.

Chapter 5: RESULTS AND DISCUSSION - II

List of Tables

Contents Page no.

List of Publications

1. Samita Thakur, O. P. Pandey, K. Singh, Structural and dielectric properties of $Bi_{1-x}Sr_xMnO_3$ ($0.40 \leq x \leq 0.55$), **Ceramics international 39 (2013) 6165-6174.**

2. Samita Thakur, O. P. Pandey, K. Singh, Effect of Ca substitution on structural, magnetic and dielectric properties of $BiFeO_3$, **Phase Transition dx.doi.org/10.1080/01411594.2013.879477.**

3. Samita Thakur, O. P. Pandey, K. Singh, Structural, thermal and electrical study of Ca^{2+}, Sr^{2+} substituted $BiFeO_3$ for IT-SOFC, **ECS Trans. 57(1) (2013) 2125-2132.**

4. Samita Thakur, O. P. Pandey, K. Singh, Electric relaxation behavior of $Bi_{0.5}Sr_{0.5}FeO_3$ ceramic: An electric modulus approach, **AIP conference Proceedings 1536 (2013) 577-578.**

5. Samita Thakur, O. P. Pandey, K. Singh, Structural and optical properties of $Bi_{1-x}A_xFeO_3$ (A=Sr, Ca; $0.40 \leq x \leq 0.55$), **J. Molecular Structure 1074 (2014) 186-192.**

6. Samita Thakur, O. P. Pandey, K. Singh, Influence of Ca^{2+} substitution on structural, thermal and conductivity behavior of $Bi_{1-x}Ca_xFeO_3$ ($0.40 \leq x \leq 0.55$), **J. Thermal analysis and Calorimetry (DOI 10.1007/s10973-014-3981-2)**.

7. Samita Thakur, O. P. Pandey, K. Singh, Structural, thermal and conductivity behavior of $Bi_{1-x}Sr_xFeO_3$ ($0.40 \leq x \leq 0.55$) for SOFC applications, **Ceramics International 40 (2014) 16371–16379.**

8. Samita Thakur, O. P. Pandey, K. Singh, A comparative structural, thermal and electrical study of Ca^{2+}, Sr^{2+} substituted $BiMnO_3$ for IT-SOFC, **Solid State Ionics (accepted).**

9. Samita Thakur, O. P. Pandey, K. Singh, Structural, thermal and electrical study of $Bi_{0.5}Sr_{0.5}MnO_3$ for solid oxide fuel cell (SOFC) applications, **Particulate Science and Technology (accepted).**

10. Samita Thakur, Malti Devi, K.Singh, Structural and optical properties of La and Gd substituted $Bi_{4-x}M_xV_2O_{11-\delta}$ ($0.1 \leq x \leq 0.3$), **Ionics 20 (2014) 73-81.** *(not part of thesis work)*

11. Rupan Kaur, Samita Thakur, K. Singh, Effect of two different sites substitution on structural and optical properties of $Bi_4V_2O_{11-\delta}$, **Physica B 440 (2014) 78–82**. *(not part of thesis work)*

Papers Presented in Conferences

1. Samita Thakur, O. P. Pandey and K. Singh, Effect of sintering temperature on structural and dielectric properties of Bi-Sr-Mn-O system, International conference on energy efficient materials: Manufacturing methods and Machineries for ceramic industries [IC2E4MCI-11] held on December 19, 2011 at Auditorium, Shilpgram, Agra.

2. Samita Thakur, O. P. Pandey, K. Singh, Structural, thermal and electrical study of Sr substituted $BiMnO_3$ system for solid oxide fuel cells applications, National conference on recent trends in materials science and research (RTMSR-2012) held on September 3-5, 2012 at NIT Srinagar, Srinagar.

3. Samita Thakur, O.P Pandey, K. Singh, Electric relaxation behavior of $Bi_{0.5}Sr_{0.5}FeO_3$ ceramic: An electric modulus approach, International conference on recent trends in applied physics and materials science (RAM-2013) held on Feb. 1-2, 2013 at Govt. College of Engineering and Technology, Bikaner.

4. Samita Thakur, O.P Pandey, K. Singh, Structural, thermal and electrical study of Ca^{2+}, Sr^{2+} substituted $BiFeO_3$ for IT-SOFC applications, National conference on innovative molecules for sustainable future held on October 24-26, 2013 at Thapar University, Patiala.

5. Effect of Ca^{2+} substitution on the structural, thermal and electrical properties of $BiYO_3$ for SOFC applications, IVth International Conference on Advances in Energy Research held on December 24-26, 2013 at IIT Mumbai, Mumbai.

ABSTRACT

Solid oxide fuel cells (SOFCs) have gain ample interest in research community due to its high efficiency and fuel flexibility without any requirement of external reforming. Despite of advantages aspects of SOFCs, still it cannot compete with conventional combustion systems in cost and durability. The current interest of researchers is to reduce the operating temperature of SOFCs to make them durable and cost effective. However, lower operating temperature of SOFC (below 800 °C) leads to some other problems such as reduction in electrode kinetics. The most pronounced effect of reduced temperature is felt on oxygen reduction reaction at the cathode side. It is believed that use of mixed electronic-ionic conducting oxides as a cathode could serve the purpose, because, the active sites for oxygen reduction will extend from triple phase boundary region to entire electrode surface in this case.

In order to achieve this, the bismuth based mixed ion conductors have been investigated in the present work as these perovskites exhibit high electrical conductivity. The $Bi_{1-x}M_xMnO_{3\pm\delta}$, $Bi_{1-x}M_xFeO_{3\pm\delta}$, $Bi_{1-x}M_xYO_{3\pm\delta}$ and $Bi_{1-x}M_xCrO_{3\pm\delta}$ (M=Ca, Sr; $0.40\leq x=0.55$) systems have been synthesized by solid state reaction method and investigated for their structural, thermal and electrical properties. Some of the selected samples were also investigated for their chemical compatibility with YSZ (8 mol % Y_2O_3 stabilized zirconia) electrolytes. The entire work in this thesis is organized in the six chapters:

- **Chapter 1** describes the background and fundamentals of different types of fuel cells. The merits, demerits and the potential applications of the fuel cells in different areas have been presented. The role of different components in solid oxide fuel cells has also been explained briefly. Since the present work is confined to develop materials for cathode. Therefore, the main emphasis is given on the cathode electrode of SOFCs. The overall electrode kinetics and the basic structural requirements of a material to be used as a cathode have been discussed. Perovskite and Ruddlesden-Popper structure are also explained as the majority of cathode materials are based on these crystal structures.

- **Chapter 2** provides a detailed literature survey in perspective of different cathode materials that are being investigated for SOFCs. As both A and B-site cations in perovskite (ABO_3) structure play significant role, so, the study carried out so far for both categories

of doping in different systems have been presented. In this chapter, the different cathode materials investigated so far have been categorized on the basis of different A-site and B-site cations. The cell output, limitations and the compatibility of different cathode materials with the other components of SOFC have also been presented. The current state of art of other developed cathodes based on Ruddlesden-Popper structure and composites are also presented in this chapter. The last section of this chapter presents the gaps in the study so far with the main objectives and the plan of undertaking research work.

- **Chapter 3** describes the experimental procedure followed during the course of work to achieve the objectives of the proposed work. The details of the raw materials used and the synthesis procedures followed for different systems have been given in this chapter. The fundamental details and mechanisms of different techniques viz. X-ray diffraction (XRD), X-ray photoelectron spectroscopy, Iodometric titration, Raman spectroscopy, Fourier transform infrared spectroscopy, Scanning electron microscopy (SEM), X-ray dot mapping, Differential thermal analyzer, Thermogravimetric analyzer, Dilatometery and ac impedance spectroscopy employed to characterize the samples for their structural, thermal and electrical properties have been discussed in detail.

- **Chapter 4** deals with the results of the different systems studied in this work. This chapter is further divided into four sections. First section represents the results of the study carried out on $Bi_{1-x}A_xMnO_{3\pm\delta}$ (A=Sr, Ca; $0.40\leq x\leq 0.55$) system. The effect of different substituents Sr^{2+}/Ca^{2+} on the structural, thermal and electrical properties have been discussed. Second, third and fourth section represents the results of $Bi_{1-x}A_xFeO_{3\pm\delta}$ (A=Sr, Ca; $0.40\leq x\leq 0.55$), $Bi_{1-x}A_xYO_{3\pm\delta}$ (A=Sr, Ca; $0.00\leq x\leq 0.20$) and $Bi_{1-x}A_xCrO_{3\pm\delta}$ (A=Sr, Ca; $0.40\leq x\leq 0.55$) systems, respectively. The effect of different substituents (Sr^{2+}/Ca^{2+}) and B-site cation (Mn, Fe, Y, Cr) on different properties have also been discussed. The structural, thermal and electrical properties have been discussed in the light of structural transformation, ordering/disordering created in the systems due to the conversion of B-site cation into higher oxidation state and generation of oxygen vacancies by the lower valence cation.

- **Chapter 5** presents the chemical interaction study of some selected samples of the different series with YSZ electrolyte. The best samples of each series were chosen on the basis of their electrical conductivity and thermal expansion coefficient. The chemical interaction between present studied systems and electrolyte was investigated with the help of XRD, SEM and X-ray dot mapping techniques. The interaction study indicates the

formation of $SrZrO_3$ and m-ZrO_2 phases in all the samples which increase with the increase in the duration of heat treatments. The formation of these phases has been explained on the basis of tolerance factor and stability of B-site cations of these perovskite oxides.

- **Chapter 6** presents the summary of the results obtained from structural, thermal, electrical and interaction study of the different series. At the end of this chapter, future scope of this study has also been given to enrich this work.

Chapter 1

INTRODUCTION

Overview

The current and future requirements of energy have led to develop various alternate energy resources which also include fuel cells. Among the fuel cells, solid oxide fuel cell (SOFC) is being preferred because of its high efficiency with fuel flexibility without any external reforming. However, the problem with existing SOFC is its high operating temperature. So, currently the researchers working in this area are focusing to reduce its operating temperature. Reducing the operating temperature will also reduce the electrode kinetics and increase the polarization resistance of the conventionally used materials. The research is going on to develop new materials for all components of SOFC particularly cathode material. In order to solve this problem, doping of different constituents is done to increase the reaction kinetics of cathode materials at low temperatures. Basically, doping influences the structure which also influences the polarization and ultimately the current carrying capacity of the material. In the present work, these problems with existing categories of materials are discussed. The emphasis is to understand the electrode kinetics and search a remedial solution to address these problems. Among the different components used in SOFCs, the cathode material is one on which this work has been carried out.

All over the world, research is going on to develop new non-conventional energy sources to meet the future energy demands. Depletion of fossil fuels, degradation of electric power industry and polluting byproducts from conventional energy sources have further strengthen this area of research. It is now well recognized that global warming is taking place mainly due to the emission of different gases from conventional energy sources and it is expected that carbon emission will increase by 54 % levels from current data by 2020 [1]. Moreover, conventional energy sources (fossil fuels) are going to exhaust in near future whereas the energy demand is increasing day by day. So, there is need to develop new power generation technologies in near future which should also be the solutions for our environmental related problems.

In response to the critical need for cleaner energy technology, some potential solutions have been considered which includes energy conservation through improved energy efficiency, reduction in consumption of fossil fuels and development of environmental friendly energy sources such as renewable energy sources and fuel cells. The major drawback associated with the use of renewable energy sources is their dependence on the climate conditions. Additionally, still we are not able to store and transport renewable energy on large scale [2]. On the other side, fuel cells in these days are much into interest all over world as they have proved their potential as future energy source due to their high efficiency, simple processing and environment friendly operations [3, 4].

1.1 Fuel cells

A fuel cell is defined as an energy conversion device that directly converts the chemical energy of a fuel into electrical energy and heat without the direct combustion and emission of carbon oxides (CO_x), nitrous oxides (NO_x) and sulphur oxides (SO_x). The energy efficiency of a fuel cell is between 40-60 % and it can be efficient in some cases up to 85 % if waste heat is captured and used [5, 6]. Individual fuel cell produces relatively small potential of only 0.7 V, so, large number of cells are stacked together to increase the voltage and to meet applications requirements. A schematic diagram of a simple fuel cell is shown in figure 1.1.

Fuel cells are classified into different types depending upon their working temperature and the electrolytes used. The different types of fuel cells are shown in figure 1.2 and listed in table 1.1 [7 -9]. The first five categories of fuel cells viz. alkaline fuel cell (AFC), direct methanol (DMFC), phosphoric acid (PAFC), sulphuric acid (SAFC), proton exchange membrane (PEMFC) are characterized by their low to medium temperature of operation i.e.

Table 1.1: Different types of fuel cells depending upon the operating temperature, efficiency, electrolytes, major applications and disadvantages.

Types of fuel cell	Electrolyte used	Fuel	Oxidant	Efficiency	Applications	Disadvantages
Alkaline fuel cell (AFC) (50-200 ˚C)	Aqueous solution of Potassium hydroxide	Pure hydrogen/hydrazine	O_2/Air	50-55%	• Space • Military	• Sensitive to CO_2 in fuel and air • Electrolyte management
Direct methanol fuel cell (DMFC) (60–200 ˚C)	Polymer membrane	Liquid methanol	O_2/Air	20–30%	• Mobile phones, digital cameras or laptops • Military applications	• Low efficiency • The diffusion of methanol and causing a fuel loss of 40%
Phosphoric acid fuel cell (PAFC) (150-200 ˚C)	Phosphoric acid soaked in a matrix	Hydrogen from hydrocarbons and alcohol	O_2/Air	40%	• Distributed generation	• Pt catalyst • Long start up time • Low current and power
Sulphuric acid fuel cell (SAFC) (80-90 ˚C)	Sulphuric acid	Alcohol / Impure hydrogen	O_2/Air	40%	• Distributed generation	• Long start up time • Low current and Power
Polymer exchange membrane fuel cell (PEMFC) (50-100 ˚C)	Perfluoro sulfonic acid	Hydrocarbons/ methanol	O_2/Air	60% transportation 35% stationary	• Backup power • Portable power • Distributed generation • Transportation • Specialty vehicles	• Expensive catalysts • Sensitive to fuel impurities • Low temperature waste • Heat
Molten Carbonate fuel cell (MCFC) (600-700 ˚C)	Solution of lithium, sodium, and/ or potassium carbonates, soaked in a matrix	Hydrogen, carbon monoxide, natural gas, propane, marine diesel	O_2/CO_2/ Air	45-50%	• Electric utility • Distributed generation	• High temperature corrosion and breakdown of cell components • Long start up time • Low power density
Solid oxide fuel cell (SOFC) (800-1000 ˚C)	Yttria stabilized zirconia	Hydrocarbons	O_2/Air	60%	• Auxiliary power • Electric utility • Distributed generation	• High temperature corrosion and breakdown of cell components.

200 °C. In the presence of methanol and hydrocarbons fuels, their efficiency reaches up to 40 %. It could reach up to 50 % when pure hydrogen is used as fuel. In these fuel cells relatively pure hydrogen is supplied at the anode side. Moreover, the use of hydrocarbons or alcohol fuels require an external reforming of fuels which increases the complexity of the system and decreases the overall efficiency [9-10]. The last two types of fuel cells viz. molten carbonates (MCFC) and solid oxide (SOFC) fuel cells are characterized by their high operating temperature i.e. 600-1000 °C. In addition to conventional fuel like hydrogen; hydrocarbons can also be used as fuel without any external reforming. Their efficiency is also quite high (45-60 %) for electrical power and reaches up to 90 % with heat recovery [11, 12].

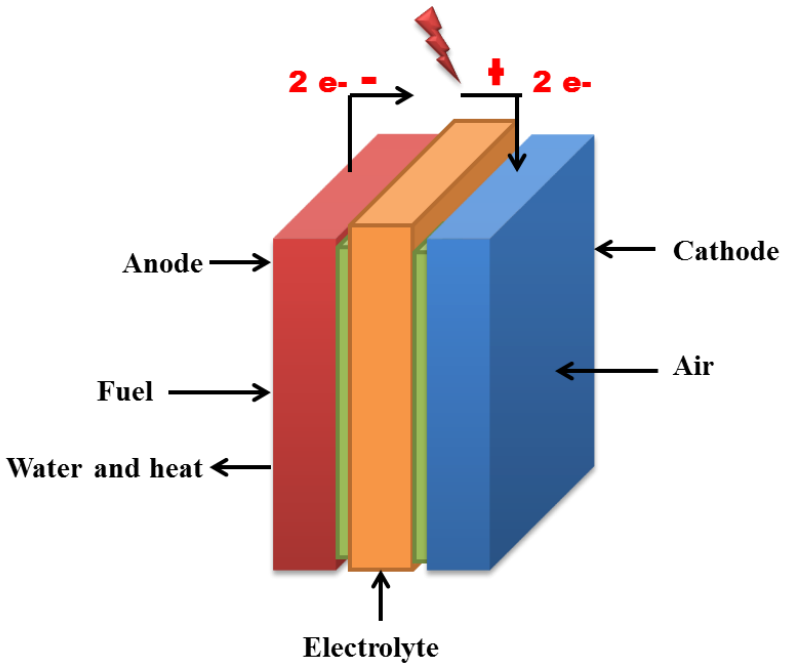

Figure 1.1: Schematic diagram of fuel cell [7].

Different types of fuel cells have different application area e.g. high temperature fuel cells are used in stationary power systems due to their high efficiency and greater fuel flexibility. However, for portable power applications, lower temperature fuel cells are preferred as it enables rapid startup and minimizes stresses due to thermal cycling. Alkali and phosphoric acid fuel cell technology are the most mature whereas; polymer electrolyte membrane and solid oxide fuel cell are most recent technologies. Though substantial progress has been made in each of fuel cell technology. Alkali fuel cells deliver extremely high power densities but are considered as useless because of the need to remove carbon dioxide from both the fuel and oxidant side in order to prevent the formation of non-conducting alkali carbonates after the reaction with CO_2 [13]. Phosphoric acid fuel cells have also been abandoned due to the

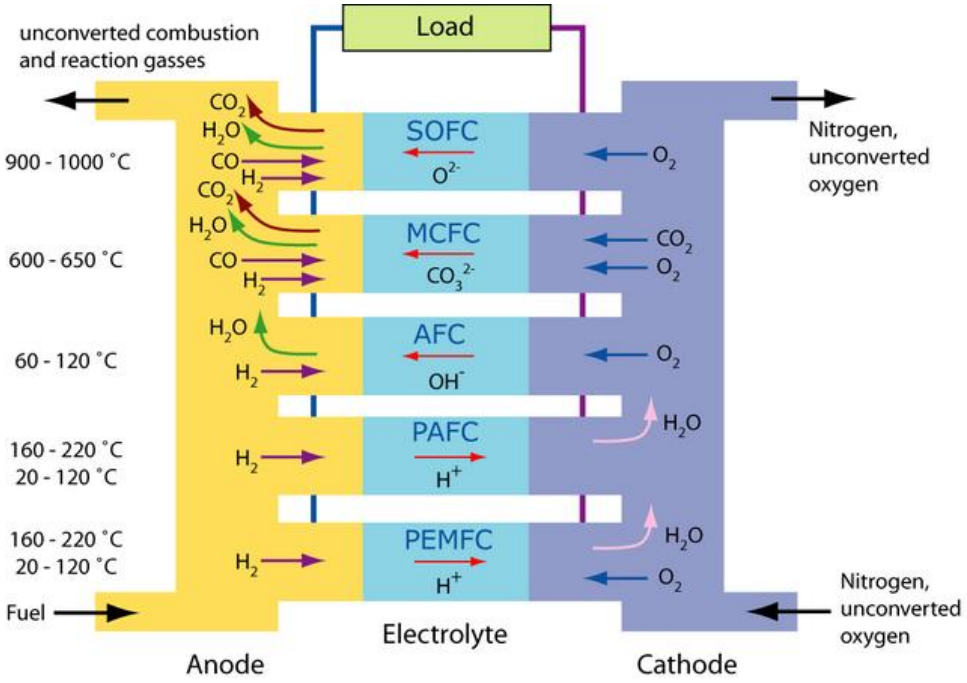

Figure 1.2: Different categories of fuel cells on the basis of operating temperature, fuel and transport ions [9].

inability to reach high power densities and to compete the cost targets on a per watt output basis [14]. Polymeric fuel cells in particular have gained a tremendous amount of attention due to their applicability in transportation system. But the major limitation in their commercialization is to maintain the air and water supply across the polymer membrane to keep it in wet conditions [15]. Solid oxide fuel cells and molten carbonate fuel cells have their greater applicability in stationary power generation. The molten carbonate fuel cells have a liquid electrolyte which increases the chances of corrosion in these fuel cells. In particular, dissolution of NiO at the cathode and precipitation of Ni at the anode can result in electrical short circuit across the electrolyte [16]. In spite of the advantages and disadvantages of all the fuel cells, presently, most of the research throughout the world has focused on the proton exchange membrane fuel cells for the portable applications and solid oxide fuel cells for stationary power systems.

1.2 Solid oxide fuel cells

High temperature solid oxide fuel cell comprises of a solid oxide ion conducting electrolyte and two electrodes. It offers a clean, low pollution technology to generate electrical energy. High efficiency, reliability, modularity, fuel adaptability and very low emissions of SO_x and NO_x make them more efficient over traditional energy conversion systems [17].

The operating temperature of SOFCs is extremely high (800-1000 ˚C). The high operating temperature has two fold effects. For instance, they are able to reform natural gas within the fuel stack and eliminate the need of external reforming systems due to high temperature. They also electrochemically oxidize a mixture of hydrogen and carbon monoxide into water and carbon dioxide which is internally generated from the natural gas. Any external catalyst is not required. The efficiency of these fuel cells can reach up to 60 % with an additional 20 % as heat recovery [18]. However, on the other hand, the high operating temperature leads to corrosion and thermal stability related problems.

The development of SOFC technology has been principally targeted towards the large scale power generation and is expected to produce 1-3 Megawatts (MW) of power [19]. But over the past few decades, it is realized that these systems can also be used to provide heating and electricity for buildings (domestic and small scale commercial units) or provide electrical power for auxiliary function (electric windows/air conditioning) in vehicles etc.

1.2.1 Operation and design of SOFCs

A single cell of SOFC consists of three main components: porous anode (fuel electrode), porous cathode (air electrode) and a dense electrolyte. The electrolyte separates the anode and cathode electrode and facilitates the ionic transport required for the oxidation of fuel. Hydrogen fuel is fed into the anode of fuel cell and oxygen (air) enters into the cell through the cathode. When fuel containing hydrogen burns at the anode side of the electrolyte, the concentration of oxygen is drastically reduced. The oxygen ions will move from the electrolyte and react with the fuel which is oxidized, thereby generating the electrons. On the cathode side, an oxygen concentration gradient is created across the electrolyte, which attracts oxygen ions from the cathode side to anode side (fuel side). Through an external electrical connection, electrons are transferred from anode to cathode side and continuous supply of oxygen ions for electrolyte is maintained. Oxygen ions from the cathode to anode maintains the overall electrical charge balance, thereby generates useful electric power by burning of the fuel. The only byproduct of this process is water molecule (H_2O) and heat [20, 21]. The overall reaction of SOFC is also shown in figure 1.3.

The reactions at the different side of the electrolyte can be written as:

Anode: $H_2 + O^{2-} \rightarrow H_2 + 2e^-$

$$CO + O^{2-} \rightarrow CO_2 + 2e^{-1}$$

$$CH_4 + O^{2-} \rightarrow 2H_2O + CO_2 + 8e^- \quad [1.1]$$

Cathode: $O_2 + 4e^- \rightarrow 2O^{2-}$ [1.2]

Overall reaction: $\frac{1}{2}O_2 + H_2 \rightarrow H_2O$ [1.3]

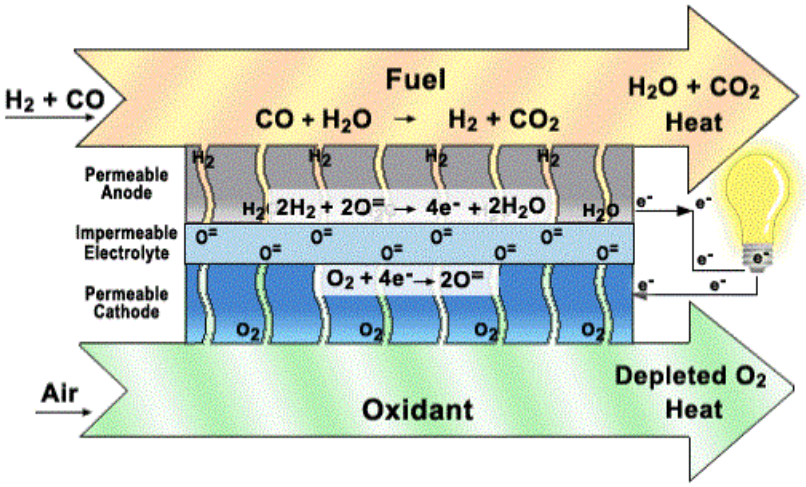

Figure 1.3: Working of solid oxide fuel cell [22].

A single cell of SOFC will provide power of the order of 1 Wcm^{-2} and these cells are combined to form the fuel cell stack. This modularity of fuel cell allows stack size to be increased or decreased to achieve the desired application. However, the stacking of the fuel cell introduces the complexity in the device through the usage of interconnects and the balance of plant is necessary to provide fuel, air and to collect current.

1.2.2 Components of SOFC

Figure 1.4 shows the schematic presentation of SOFC for their stack configuration. The main components of a single cell are electrolyte, anode (fuel electrode) and cathode (air electrode). When cells are stacked together to generate more power; interconnect are also required. Different designs have been proposed for SOFC; these include planar and tubular geometries. The planar design of SOFC requires one another component i.e. glass sealant. The materials for cell components in all the designs are either same or similar in nature. The detailed requirements of all the components of SOFCs are given below:

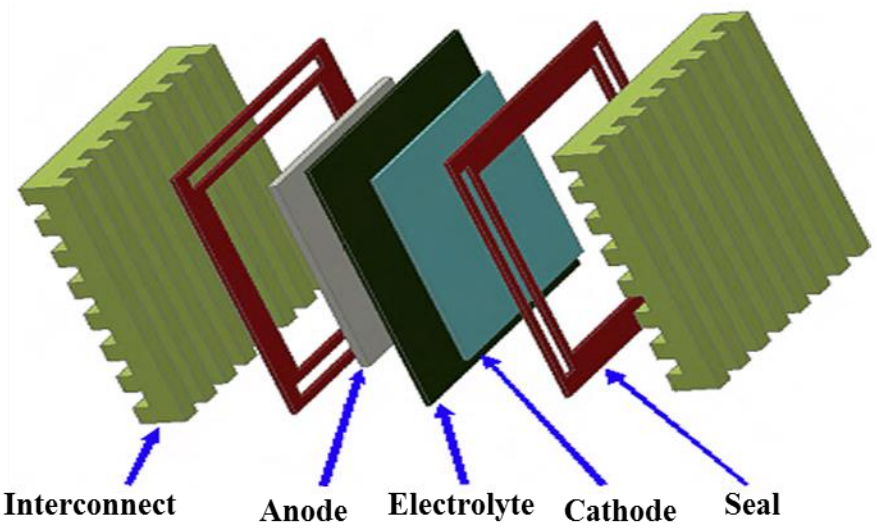

Figure 1.4: Stack configuration of solid oxide fuel cell [23].

1.2.2.1 Solid electrolyte

Electrolyte, an ion conducting ceramic carries oxide ion from cathode side to anode side of SOFC. The basic required properties of a material to be an electrolyte are as follows [24]:

1. High oxide ion or proton conductivity i.e. 0.01-0.1 S cm^{-1} for 1-100 μm thick electrolyte.
2. Low or negligible electronic conductivity. Higher electronic conductivity will cause higher voltage losses and oxygen leakage without producing electricity.
3. As electrolyte in SOFC is exposed to both reducing (anode side) and oxidizing (cathode) atmosphere. So, selected materials should be stable in both the conditions.

Fluorite structure oxide materials such as yittria stabilized zirconia, rare earth doped ceria and rare earth doped bismuth oxides have been widely investigated as electrolytes for SOFCs [25-28]. YSZ (8 mol % Y_2O_3 stabilized zirconia) is widely used as electrolyte for SOFCs. Scandia stabilized zirconia shows higher conductivity and excellent stability under oxidizing and reducing atmosphere than YSZ. However, the main problem with their commercialization is the price and availability of scandia [29]. Gadolinium doped ceria also shows higher conductivity than YSZ but ceria shows mixed conductivity (electronic and ionic) at low oxygen partial pressures [30]. Now a days, the research has been focused on to investigate the perovskite structured Sr and Mg doped lanthanum gallate $La_{1-x}Sr_xGa_{1-y}Mg_yO_3$ ($0.0 \leq x \leq 0.20$; $0.0 \leq y \leq 0.20$) (LSGM)). The maximum conductivity of these materials has been

reported for 10 mol% Sr and 15-20 mol% Mg [31]. The limitation of these materials is the phase stability, Ga evaporation at low oxygen partial pressures and its incompatibility with NiO which is generally, used as anode material [32-34].

1.2.2.2 Electrode

The SOFC consist of two electrodes; anode and cathode. The required parameters for any material to be used as electrode are [35]:

1. Catalytic activity: oxygen dissociation at cathode side and for electrochemical oxidation of fuel at anode side.
2. Electronic conductivity.
3. Chemical stability and compatibility.
4. Matching thermal expansion coefficient (TEC) with other components of SOFC.

Anode

The anode serves as an electrochemical site for the oxidation of fuel. This fuel electrode also provides path for the electrons to move from the anode/electrolyte surface to the interconnect side. Ni-YSZ cermet is most commonly used anode material in SOFC [36, 37]. Ni provides the electronic conductivity and YSZ provides the ionic conductivity. The main drawback of this anode material is degradation of catalytic activity of Ni in the presence of sulphur and carbon in the fuel [38]. Due to these limitations, the Cu-YSZ has also been explored as it is more tolerant to sulphur impurities than Ni-YSZ. However, it is unstable under SOFC operating conditions [39].

Now days, $SrTiO_3$ has also been proposed as an alternative anode materials. It is chemically stable and shows electronic conduction upon reduction of Ti^{3+} to Ti^{4+}. Even it is also chemically stable with YSZ [40]. However, in case of LSGM as an electrolyte, the diffusion of dopant (Ga, Mg) reduces the thermal stability [41].

Cathode

The cathode or air electrode is a thin porous layer on electrolyte. It operates in an oxidizing atmosphere of air or oxygen and participates in oxygen reduction reaction. The air electrode should have high electronic conductivity. Chemical stability, along with sufficient porosity to facilitate the transport of oxygen ions, is required. Alkaline earth and rare earth cations doped

lanthanum manganite are used as conventional cathode materials for SOFCs [42]. The undesirable phases $La_2Zr_2O_7$ and/or $SrZrO_3$ results due to the reaction of this material with YSZ. Ceria based electrolyte is commonly used in between YSZ and $La_{0.8}Sr_{0.2}MnO_3$ (LSM) to prevent its reactivity. Doped $LaFeO_3$, $(BaSr)(CoFe)O_3$, $BiMnO_3$ and $BiFeO_3$ have also been investigated for cathode in SOFCs these days [43-46].

1.2.2.3 Interconnects

Many cells are stacked together for their practical use. So, interconnect is required for connecting the individual cells. In general, interconnect provides electrical connection between anodes of one cell to the cathode of the neighboring cell. It also prevents the mixing of gases from anode side to the cathode and also avoids oxidation of anode and reduction of cathode. These materials should be electronic conductor, stable under reducing and oxidizing atmosphere, less permeable to oxygen and hydrogen. Doped lanthanum chromite satisfy the above conditions and is used as interconnect for SOFCs [47]. The ceramic interconnects are generally used with YSZ. Their high cost and decrease in conductivity at low temperatures is main limitation for their use. So, metallic interconnect have also been developed which typically consists of Cr and Fe based alloys. High electric conductivity, high thermal conductivity and enhancement of the ability to accommodate thermal stresses are the main advantages of metallic interconnects over the ceramic interconnects. However, the metallic interconnects suffer from some drawbacks such as electrical contacts between metallic interconnect and ceramic electrodes, matching of thermal expansion, oxide scale formation on the metallic surface and cathode poisoning [48].

1.2.2.4 Sealants

In planar design of SOFCs, a tight seal is required to keep fuel gas and air separated from each other to prevent direct combustion of fuel. The sealants need to be chemically and thermally stable under reducing and oxidizing atmosphere. The quality of seals must be high. Even small leaks in these seals can affect the cell potential resulting in the reduction of performance. Sealants must possess the wide range of thermal expansion coefficient to have the compatibility with the other components used in a cell. Two types of seals are developed for SOFCs; compressive and rigid seals. Compressive seals are tightly fixed to other components of SOFCs so the exact matching of thermal expansion is not necessary. In case of these seals, the load must be continuously supplied during the operation. These seals are normally the metal gaskets i.e. silver as well as mica based materials. In case of rigid seals,

the TEC should exactly be compatible with other components. Glasses and glass ceramics are mainly used as rigid seals [49].

In spite of all the advantages of the SOFCs, yet they cannot compete with the conventional combustion systems in terms of cost and durability. Their high operating temperature is the main limitation for their commercialization. Because of high operating temperature, alloys are used to house the cell and ceramics are being used for interconnection which increases the cost of the fuel cell substantially. In recent years, great efforts have been made to develop low or intermediate temperature SOFCs (IT-SOFCs) operating at 500-800 ˚C. Lowering the operating temperature can suppress degradation of components and extend the range of acceptable materials selection. This will also improve the cell durability and reduce the system cost. Reducing the operating temperature of SOFCs has advantages for many practical applications [50]. However, 10% drop in temperature results in ~12% drop of the cell performance due to decrease in electrode kinetics and results in large interfacial polarization resistances [51]. This effect is more pronounced for the oxygen reduction at the cathode. In order to lower the polarization resistance of the cathode, a favorable electronic and ionic conductivity as well as high catalytic activity for oxygen reduction must be maintained. The present work is related to the cathode of SOFC. Therefore, the details of cathode materials and the reaction mechanism are given in the following sections.

1.3 Cathode and reaction mechanism

1.3.1 Requirements for cathode materials

In SOFCs, the cathode functions as the site for electrochemical reduction of oxygen. For this reaction, the cathode must have [52]:

1. High electronic conductivity: more than 100 S cm^{-1} under oxidizing atmosphere.
2. Matching thermal expansion coefficient and chemical compatibility with the electrolyte and interconnect materials.
3. Adequate porosity to allow gaseous oxygen to readily diffuse through the cathode to cathode/electrolyte interface.
4. Stability under an oxidizing atmosphere during fabrication and operation.
5. High catalytic activity for the oxygen reduction reaction (ORR).

1.3.2 Electrochemical processes at cathode surface

The overall cell reaction at the surface of cathode can be written as follows:

$$\frac{1}{2}O_2(gas) + 2e^-(cathode) \rightarrow O^{2-}(electrolyte) \quad [1.4]$$

It is believed that the electrochemical reaction occurs at triple phase boundary (TPBs) where cathode (electronic conductor), electrolyte (oxygen ion conductor) and gas phase come in contact [53]. TPB is schematically shown in figure 1.5. If there is a breakdown in connectivity in any of these phases or hindrance at the reaction site due to the excess of electrons, ions or gases; the reaction site becomes inactive. Microstructure and composition directly affect the size and distribution of TPBs. Although the molecular species involved in the above reaction comprises only single diatomic oxygen, but the reaction is quite complex and involves many steps as given below [54]:

1. Adsorption, dissociation, reduction and incorporation of oxygen anion into the lattice of the cathode materials.
2. Ionic transport through the porous cathode towards the electrolyte.
3. Ions hopping into the electrolyte lattice.

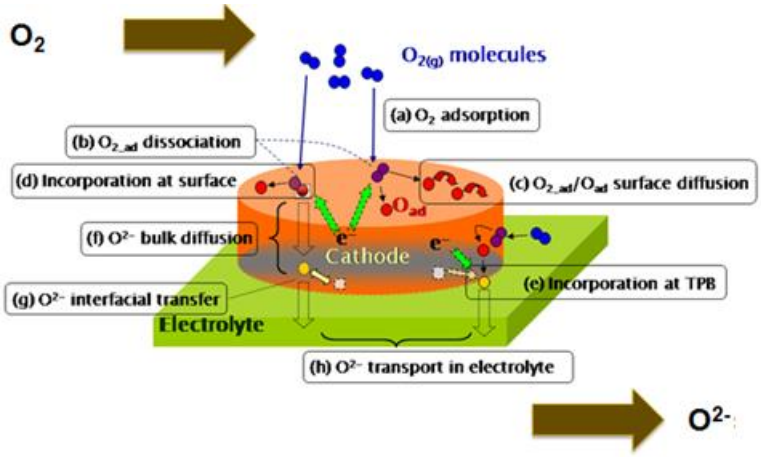

Figure 1.5: Schematic representation of triple phase boundary [55].

Among the above mentioned reaction steps, oxygen reduction step contribute the maximum to the total cell resistance and finally have strong impacts on the fuel cell performance. The three paths are described below through which the reaction can occur at the cathode:

(a) ***Electrode surface path:*** The first step in electrode surface path is to adsorb the oxygen on the cathode surface, second is oxygen diffusion along the surface towards

the triple phase boundary and final step is the complete ionization of oxygen ions and their transfer into the electrolyte. This path is followed by pure electronic conductors such as e.g. $La_{0.8}Sr_{0.2}MnO_3$ (LSM).

(b) ***Electrolyte surface path:*** In this path, all the processes adsorption, diffusion and ionization of the oxygen species occur on the electrolyte surface after that oxygen ions are directly fed into the electrolyte. Only the electrons required for the ionization of oxygen species are provided by the cathode. This path is very much similar to the electrode surface path from geometrical point of view. This path is followed by composite cathode like (LSM-YSZ).

(c) ***The bulk path:*** This path consists of oxygen adsorption; dissociation, ionization and oxide ion transport through electrode and finally transfer of ions into the electrolyte. This path is meant for mixed ionic-electronic cathode (MIEC) materials.

The different paths for the oxygen ion migration at cathode electrolyte interface are shown in figure 1.6.

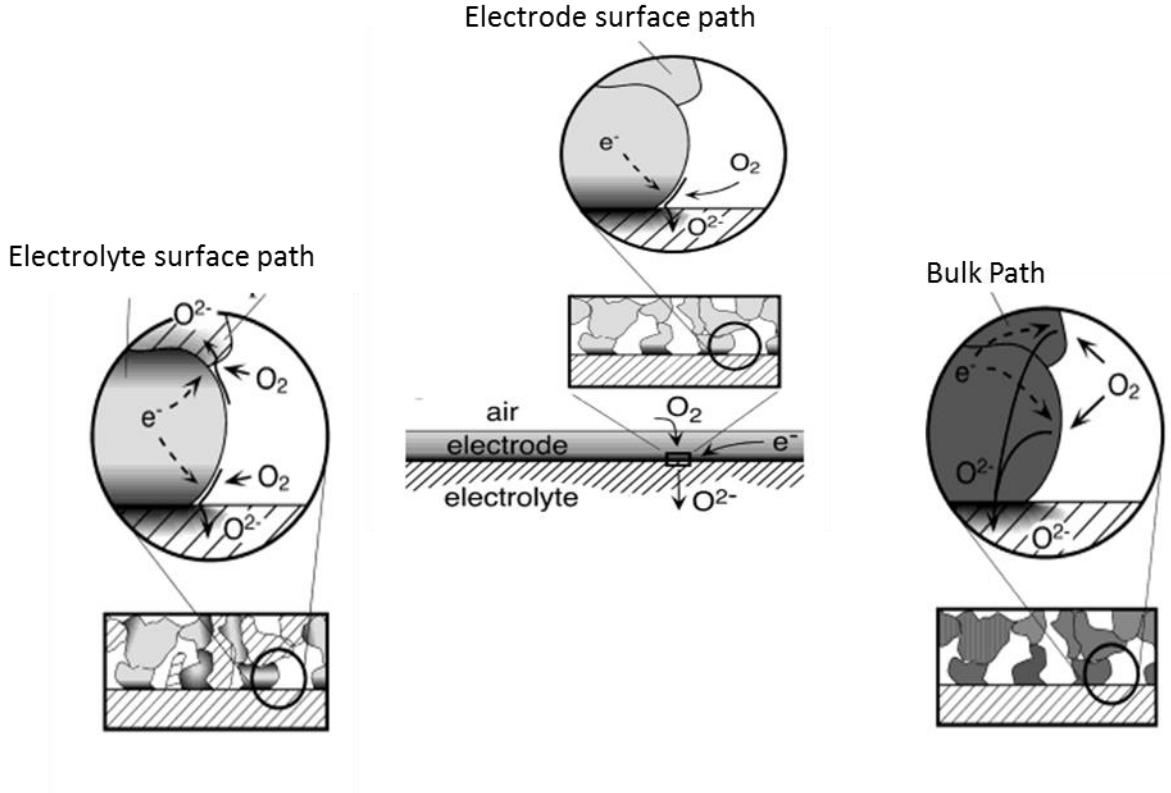

Figure 1.6: Schematic presentation of three different paths for oxygen ions formation and migration at cathode/electrolyte interface [56].

The cathodic reaction can simultaneously occur via all three paths. For each path, one or more elementary steps determine the corresponding reaction rate. Among these, the elementary reaction which will be rate-limiting step is not always predictable and may depend on local conditions like temperature and oxygen partial pressure or on microstructural conditions. It is generally said that SOFCs cathode materials should preferably be mixed ionic-electronic conductor (MIEC). If the cathode material is a pure electronic conductor, oxygen reduction reaction is limited to triple phase boundary and occurs through electrode surface path. In case of MIEC, the oxygen reduction occurs through bulk path and hence the kinetics of reaction will be enhanced. After adsorption of the oxygen, the charge transfer steps occur at the cathode surface, oxygen atoms get transferred into the oxide ions which are transported within the cathode material due to oxide ion conductivity and finally transferred to electrolyte materials. This is similar with an increase of TPB because whole surface will be available for charge transfer [57, 58].

1.4 Structural properties of cathode materials

Perovskite materials have been widely used as cathode material in SOFC because it can tolerate extensive modifications with regard to compositions. Other materials which are of interest for scientific community as cathode materials are Ruddlesden-Popper (RP) type oxides. These compounds have the general formulae $A_2BO_{4-\delta}$. The structure of both perovskite and RP type oxides are similar. RP type structures have the general formulae $A_{n+1}BnO_{3n+1}$ or AO $(ABO_3)_n$. Thus, it can be said that perovskite structures (ABO_3, n=∞) and RP structures (A_2BO_4, n=1) are members of RP series.

In perovskites, the larger A site cation is located at the corners of cube, B-site cation at the body center and oxygen ions at the center of faces. The A-site cation is coordinated by twelve oxygen ions whereas; ion located at B-site has six fold coordination [59]. The more complex RP structures can be derived from the perovskite structures. It has a layered structure having a brick salt layer in between the perovskite layer. The thickness of the each perovskite layer is of one unit cell and these layers are displaced from the each other by half a unit cell [60]. Unit cells of both the materials are schematically presented in figure 1.7.

These oxide structures are distorted and do not have cubic symmetry, the degree of distortion can be determined according to Goldschmidt tolerance factor as follows [61]:

$$t = \frac{r_A + r_B}{\sqrt{2}\,(r_B + r_o)} \qquad [1.5]$$

Where r_A, r_B, and r_o are effective ionic radii of A site, B-site cations and the oxygen ion, respectively. Stable perovskite structures are predicted for $0.77 \leq t \leq 1$. For RP oxides to exist this tolerance factor lies in the range of $0.85 < t < 1.05$. The perfect cubic structure (t=1) is attained when A site cation has the same ionic radii as that of oxygen ion (1.40 Å). In this case B site cations are located in the octahedral vacant sites formed by oxygen.

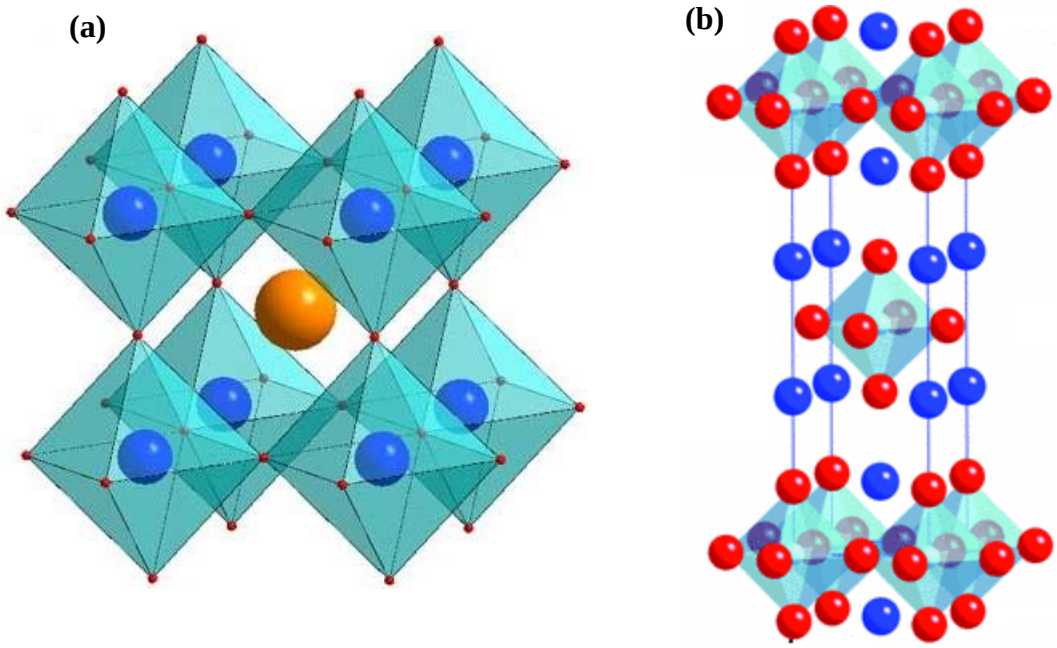

Figure 1.7: (a) Perovskite structure: yellow ball presents A –site cation, blue to B-site cation and red to oxygen [59] (b) Ruddelsden-Popper: dark blue balls to A site cations, translucent blue to B- octahedral and red to oxygen [60].

In a perfect cubic perovskite structure, the B-O-B chains are linear i.e. bond angle is 180˚. Deviation from the cubic symmetry results in tilting of BO_6 octahedra and therefore in reduced B-O-O bond angles. For t<1, the lattice structure changes from cubic to rhombohedral and then to orthorhombic and tetragonal symmetry.

For most of the perovskite and RP cathode materials, the A-site cation is a mixture of rare earth and alkaline earth metals such as La and Sr/Ca while the B-site cation is a transition metal (TM) such as Mn, Fe, Co and Ni or a mixture of these. Divalent acceptor substitution for the trivalent A site cation creates charge imbalance in the system which is compensated either by an increase in valance of the B-site cation (electronic compensation) and/or by the formation of oxygen vacancies (ionic compensation). The change in oxidation state of B-site cation on substitution at A-site create TM^{3+}/TM^{4+} couples which act as hopping site for electrons and holes i.e. for n type or p type conductivity. Higher the amount of available hopping sites, the higher the conductivity values are expected. Therefore, the theoretical

maximum conductivity is expected for 50 mol % divalent acceptor substitution if and only if electronic compensation is assumed. However, the relative proportion between the generation of oxygen vacancies and oxidation of the transition metal ion is dependent upon temperature, partial pressure of oxygen and chosen material [62].

In a mixed (ionic-electronic) conductor, there should be an appropriate ionic with electronic conductivity. The oxygen ions in a crystal system move from one vacancy to another adjacent vacancy (hopping) and generate oxide ion conductivity. Vacancies in the crystal structure can be inherent and also can be generated by proper substitution. However, there is limit for substitution because higher substitution can lead to large number of oxygen vacancies and these vacancies can induce structural deformations or the vacancies can become ordered which can lead to decrease in ionic conductivity [63]. There are even certain transition metal cations who enhance the ionic compensation as compared to electronic compensation e.g. manganese containing perovskites mostly perform electronic compensation but it has also been observed that if manganese is substituted by iron, then electronic conductivity decreases while ionic conductivity increases due to increase in ionic compensation [64]. Temperature and oxygen partial pressure play a very important role to decide the relative generation of oxygen vacancies and oxidation of transition metal cation.

1.4.1 Structural requirements for ionic conductivity

The ionic conductivity is not only dependent upon the presence of oxygen vacancies but is also affected by other structural parameters [65]:

- Goldschmidt tolerance factor (t).
- The size of the smallest dimension of the pathway of oxide ion movement, the critical radius (r_c). where, $r_c = \frac{a_0\left(\frac{3}{4}a_0 - \sqrt{2}r_B\right) + r_B^2 - r_A^2}{2(r_A - r_B) + \sqrt{2}a_0}$ [1.6]
- The lattice free volume (V_f) which is obtained by the subtraction of constituent ion volume from the overall crystallographic unit cell volume.
- The lattice energy or average metal-oxygen bond energy (E_b).

Samells *et al.* [66] have examined various perovskite oxides and concluded that the activation energy for oxide ion conduction has a direct dependence upon V_f and r_c but it varies inversely with E_b. Since, r_c, t and V_f are obtained from two ionic radii of A and B-site cations whereas, E_b depends upon the cation charges and ionic radii so, all these parameters are correlated to

each other. It is impossible to vary one without varying the others. To find an optimum material; some compromises up to certain extent have to be made because specific free volume can be increased at the expense of departure from cubic symmetry whereas, for oxygen ion conductivity material should be perfect cubic. However, the cubic $A^{3+}B^{3+}O_3$ structure does not exist at room temperature, but at elevated temperatures they can transform their crystal structure to higher symmetries [67].

1.4.2 Structural requirements for electrical conductivity

In perovskite structure, BO_6 octahedral build up as three dimensional networks. The electronic conduction proceeds through B-O-B chains by electron/holes and are dependent upon the covalency of B-O-B bond which arises due to the polarization of anions [68]. The degree of polarization further depends upon the polarizing power of cation which can be calculated by Ze^2/r, where Z is formal valence, e is electronic charge and r is the radius of cation. Figure 1.8 shows the orbitals of an oxygen ion and B-site cation. The anionic P_σ orbitals are strongly attracted by the nuclear charge of the cation and combine strongly with P_σ orbitals of cation. The collinear overlap is the major part of the overall B-O bonding and strongly screens the d-orbitals of the B-cation. Thus, the d-orbitals of the B-cation overlap the p-orbitals of the oxygen ion. This condition explains the existence of electronic properties of perovskites [66].

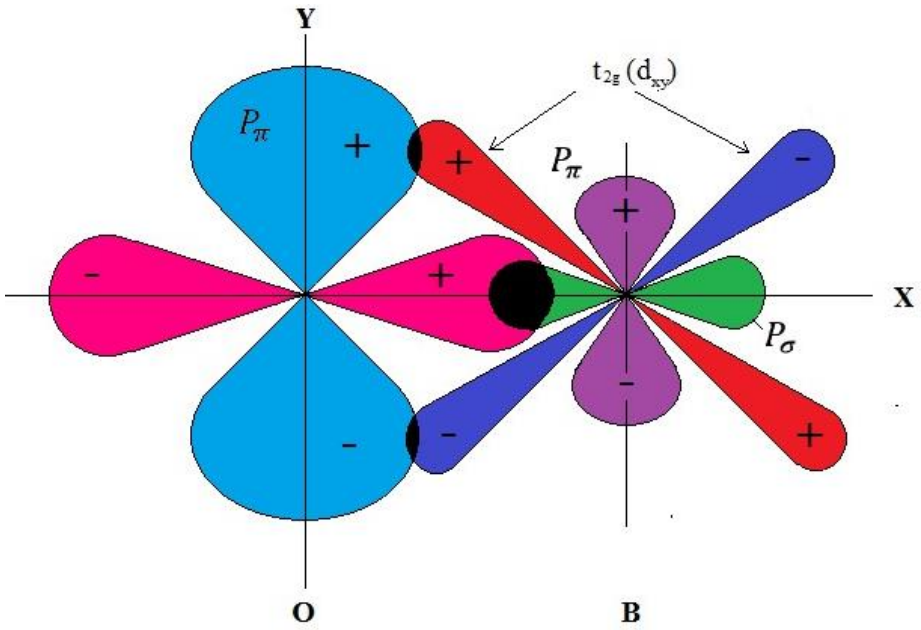

Figure 1.8: Covalent bond between oxygen and B-site cation [69].

The second factor which affects the electrical conductivity is the degree of distortion from ideal cubic structure. It has been already described that the bond angle of linear B-O-B bond

(180˚) in a perfect cubic structure decreases when the structure deviates from ideal cubic symmetry. With the decrease/increase in average radius of the A-site cation, the BO_6 octahedra start to tilt and B-O-B bond angles also decreases. This tilting narrows the conduction band and also increase the band gap that results in semiconducting behavior. However, in materials containing transition metal oxides, the B site cation also get oxidized to higher oxidation state (B^{3+}/B^{4+}) with the substitution. The smaller radius of B^{4+} reduces the B-B distances and results in the B-O-B bond angle approaching 180˚. These structural changes with substitution are responsible for the transition from semiconducting to metallic character in $La_{0.80}Sr_{0.20}MnO_3$, $La_{0.60}Sr_{0.40}Co_{0.20}Fe_{0.8}O_{3-\delta}$, and $Ba_{0.80}Sr_{0.20}Co_{0.20}Fe_{0.80}O_{3-\delta}$ [70-73].

So, it can be concluded that ionic and electronic conductivity is highly dependent upon the formation of oxygen vacancies, free electrons/holes and structural properties of the materials. In case, transition elements are present, the knowledge of the existing valence state of the element in the compound is highly important.

References

[1] A. B. Stambouli, E. Traversa, Renew Sust Energ Rev 6 (2002) 433.

[2] J. W. Eerkens, The Nuclear Imperative Edt. 16 (2010) Springer New York.

[3] S. M. Haile, Acta Mater. 51 (2003) 5981.

[4] B. C. H. Steele, Nature 400 (1999) 619.

[5] N. Q. Minh, T. Takahashi, Science and Technology of Ceramic Fuel Cells (1995) Elsevier Science Amsterdam.

[6] N. Q. Minh, J. Amer. Ceram. Soc. 76 (1993) 563.

[7] J. H. Hirschenhofer, D. B. Stauffer, R. R. Engleman, M. G. Klett, Fuel Cell Handbook Edt. 4 (1998) Parsons Corp. USA.

[8] B. C. H. Steele, A. Heinzel, Nature 414 (2001) 345.

[9] S. Srinivasan, Fuel Cells: From fundamental to applications Edt. 1 (2006) Springer Science & Business Media New York.

[10] J. Larmine, D. Andrews, Fuel Cell Systems (2000) John Wiley & Sons Ltd. USA.

[11] O. Yamamoto, Electrochim. Acta 45 (2000) 2423.

[12] B. C. H. Steele, J. Mater. Sci. 36 (2001) 1053.

[13] E. Gulzow, Fuel Cells 4 (2004) 251.

[14] N. Sammes, R. Bove, K. Stahl, Curr. Opin. Solid State Mater. Sci. 8 (2004) 372.

[15] Y. Wanga, K. S. Chenb, J. Mishler, S. C. Cho, X. C. Adroher, Appl. Energy 88 (2011) 981.

[16] T. A. Hamada, A. A. Agll, Y. M. Hamada, S. Bapat, M. Thomas. K. B. Martinc, J. W. Sheffield, Case Stud Therm. Engg. 1 (2013) 45.

[17] S. C. Singhal, K. Kendall, High temperature solid oxide fuel cells: fundamentals (2000) Elsevier New York.

[18] S. C. Singhal, Solid State Ionics 135 (2000) 305.

[19] S. C. Singhal, MRS Bull. 25 (2000)16.

[20] M. Liu, M. E. Lynch, K. Blinn, F. Alamgir, Y. Choi, Mat. Today Invited Rev. 14 (2011) 534.

[21] N. H. Menzler, P. Batfalsky, Fuel Cell Science and Engineering: Materials, Processes, Systems and Technology (2012) Wiley Science, USA

[22] J. M. Bockris, S. Srinivasan, Fuel Cells: Their Electrochemistry (1969) McGraw-Hill New York.

[23] M. K. Mahapatra, K. Lu, J. Power Sources 195 (2010) 7129.

[24] V. V. Kharton, F.M.B. Marques, A. Atkinson, Solid State Ionics 174 (2004) 135.

[25] K. Otsuka, A. Kuwabara, A. Nakamura, T. Yamamoto, K. Matsunaga, Y. Ikuhara, Appl. Phys. Lett. 82 (2003) 877.

[26] T. H. Etsell, S. N. Flengas, Chem. Rev. 70 (1970) 339.

[27] E. C. Subbarao, H. S. Maiti, Solid State Ionics 11 (1984) 317.

[28] S. Hui, J. Roller, S. Yick, X. Zhang, C. D. Petit, Y. Xie, R. Maric, D. Ghosh, J. Power Sources 172 (2007) 493.

[29] L. Malavasi, C. A. J. Fisher, M. S. Islam, Chem. Soc. Rev. 39 (2010) 4370.

[30] B. Zhu, J. Power Sources 114 (2003)1.

[31] A. C. Tas¸ P. J. Majewski, F. Aldinger, J. Am. Ceram. Soc. 83 (2000) 2954.

[32] K. Huang, R. S. Tichy, J. B. Goodenough, J. Am. Ceram. Soc. 81 (1998) 2565.

[33] T. Ishihara, H. Matsuda, Y. Takita, J. Am. Chem. Soc. 116 (1994) 3801.

[34] M. Feng, J. B. Goodenough, Eur. J. Solid State Inorg. Chem. T31 (1994) 663.

[35] C. Suna, U. Stimming, J. Power Sources 171 (2007) 247.

[36] C. Suciu, A. C. Hoffmann, E. Dorolti, R. Tetean, Chem. Eng. J. 140 (2008) 586.

[37] S. P. Jiang, S. H. Chan, J. Mater. Sci. 39 (2004) 4405.

[38] M. Gong, X. Liu, J. Trembly, C. Johnson, J. Power Sources 168 (2007) 289.

[39] Y. M. Choi, C. Compson, M. C. Lin, M. Liu, J. Alloys Comp. 427 (2007) 25.

[40] R. N. Basu, Materials for Solid Oxide Fuel Cells Edt. 1 (2007) Springer New York.

[41] J. Fergus, JOM J. Minerals, Metals and Materials Society 59 (2007) 56.

[42] S. P. Jiang, J. Mater. Sci. 43 (2008) 6799.

[43] F. Bidrawn, G. Kima, N. Aramrueang, J. M. Vohs, R. J. Gorte, J. Power Sources 195 (2010) 720.

[44] W. Zhou, R. Ran, Z. Shao, J. Power Sources 192 (2009) 231.

[45] Y. Niu, W. Zhou, J. Sunarso, L. Ge, Z. Zhub, Z. Shao, J. Mater. Chem. 20 (2010) 9619.

[46] B. Liu, Z. Jiang, B. Dinga, F. Chen, C. Xia, J. Power Sources 196 (2011) 999.

[47] J. W. Fergus, Solid State Ionics 171 (2004) 1.

[48] J. W. Fergus, Mat. Sci. Engg. A 397 (2005) 271.

[49] J. W. Fergus, J. Power Sources 147 (2005) 46.

[50] S. B. Adler, Chem. Rev. 104 (2004) 4791.

[51] S. Hou, A. Aguadero, J. A. Alonso, J. B. Goodenough, J. Power Sources 196 (2011) 5478.

[52] C. Sun, R. Hui, J. Roller, J. Solid State Electrochem. 14 (2010) 1125.

[53] V. M. Janardhanana, V. Heuvelineb, O. Deutschmann, J. Power Sources 178 (2008) 368.

[54] J. Fleig, Annu. Rev. Mater. Res. 33 (2003) 361.

[55] Y. L. Lee, J. Kleis, J. Rossmeisl, D. Morgan, Phys. Rev. B 80 (2009) 224101.

[56] Y. L. Lee, J. Kleis, J. Rossmeisl, Y. Shao-Horn, D. Morgan, Energy Environ. Sci. 4 (2011) 3966.

[57] V. Brichzin, J. Fleig, H. U. Habermeier, J. Maier, Solid State Ionics 152 (2002) 499.

[58] E. Koep, D. S. Mebane, R. Das, C. Compson, M. L. Liu, Electrochem. Solid-State Lett. 8 (2005) 592.

[59] C. Ederer, N. A. Spaldin, Curr. Opin. Solid State Mater. Sci. 9 (2005) 128.

[60] W. D. Parker, S. M. Nakhmanson, Phys. Rev. B 88 (2013) 035203.

[61] K. Nomura, S. Tanase, Solid State Ionics 98 (1997) 229.

[62] J. C. Boivin, G. Mairesse, Chem. Mater 10 (1998) 2870.

[63] R. Kant, K. Singh, O. P. Pandey, Int. J. Hydrogen Energy 33 (2008) 455.

[64] M. Petitjean, G. Caboche, E. Siebert, L. Dessemond, L. C. Dufour, J. Eur. Ceram. Soc. 25 (2005) 2651.

[65] M. Mogensen, D. Lybye, N. Bonanos, P. V. Hendriksen, F. W. Poulsen, Solid State Ionics 174 (2004) 279.

[66] A. F. Sammells, R. L. Cook, J. H. White, J. J. Osborne, R. C. McDuff, Solid State Ionics 52 (1992) 11.

[67] Y. Wang, F. Guyot, R. C. Liebermann, J. Geophysical Research: Solid Earth 97 (1992) 12327.

[68] N. Orlovskaya, N. Browning, Mixed Ionic Electronic Conducting Perovskites for Advanced Energy Systems (2004) Springer Science & Business Media New York.

[69] L. Lang, J. H. Yang, H. R. Liu, H. J. Xiang, X. G. Gong, Phys. Lett. A 378 (2014) 290.

[70] A. Mineshige, M. Kobune, A. Fujii, Z. Ogumi, M. Inaba, T. Yao, K. Kikuchi, J. Solid State Chem. 142 (1999) 374.

[71] A. S. Harvey, Z. Yang, A. Infortuna, D. Beckel, J. A. Purton, L. J. Gauckler, J. Phys. Condens. Matter. 21 (2009) 312.

[72] A. S. Harvey, F. J. Litterest, Z. Yang, J. L. M. Rupp, A. Infortuna, L. J. Gauckler, Phys. Chem. Chem. Phys. 11 (2009) 3090.

[73] J. Pena-Martinez, D. Marrero-Lopez , J. C. Ruiz-Morales, P. Nunez, C. Sanchez-Bautista, A. J. Dos Santos-Garcıa, J. Canales-Vazquez, Int. J. Hydrogen Energy 34 (2009) 9486.

Chapter 2

LITERATURE REVIEW

Overview

This chapter deals with some of the key developments in cathode materials for SOFC applications. $La_{1-x}Sr_xMnO_3$ ($0.1 \leq x \leq 0.8$) is the conventional cathode for high temperature SOFC. However, their polarization resistance increases as the operating temperature is reduced. It is believed that mixed (ionic- electronic) conductors are the suitable cathode materials for low temperature operation of SOFCs. Various attempts have been made to improve the performance of LSM and to develop new cathode materials. Various cations at the A-site of ABO_3 (perovskite) like Pr, Sm, Gd, Nd and Ba and at B-site Mn, Fe, Ni, Co have been investigated. Even other than perovskites, Ruddlesden-Popper (K_2NiF_4) type structured materials have also been discussed for cathode materials. The disadvantages of these materials are their high thermal expansion coefficient and reactivity with the electrolytes. In this chapter, all these developments and need to address the existing problems have been described and discussed.

Mixed conductors have diverse applications. Since, present work is focused on the application of mixed (ionic- electronic) conductors for the cathode materials of SOFCs. So, in this chapter, literature review regarding the cathode materials developed so far has been presented.

2.1 Manganite cathodes

Prior to 1965, only platinum was used as a cathode material for SOFC. After that transition elements containing oxides were investigated as SOFC cathodes due to their good electrical conductivity and low cost as compared to platinum. Butter and Archer in 1965 proposed $La_{0.80}Sr_{0.20}CoO_{3-\delta}$ (LSC) as a cathode material [1]. The initial performance of LSC was good, but, it degrades with increase in time of operation of SOFC [2]. After that many perovskite oxides were studied as a cathode. In 1975, $La_{0.80}Sr_{0.20}MnO_{3\pm\delta}$ (LSM) became the favorite material for cathode. An appropriate combination of electronic conductivity and thermal expansion coefficient has made this material commercially available for SOFC applications [3-5].

$LaMnO_3$ based oxides are somewhat unusual in comparison to other perovskite oxides due to oxygen excess as well as oxygen deficient non-stoichiometry [6, 7]. These are generally denoted as $La_{1-x}A_xMnO_{3\pm\delta}$ (A=Sr, Ca; $0.1\leq x\leq 0.80$). Anderson *et al.* [8, 9] have investigated in detail the oxygen non-stoichiometry of $La_{1-x}Sr_xMnO_{3\pm\delta}$ ($0.1\leq x\leq 0.80$) as a function of oxygen partial pressure (PO_2), temperature and composition. They have observed that for $La_{1-x}Sr_xMnO_{3\pm\delta}$ ($x<0.40$), this system has oxygen excess ($3+\delta$) at high oxygen partial pressures, and stoichiometric ($\delta=0$) at intermediate oxygen partial pressures (10^{-5}-10^{-10} Pa) and oxygen deficient ($3-\delta$) at low oxygen partial pressures. LSM exists in its oxygen excess non-stoichiometry region under normal fuel cell operating conditions and becomes oxygen deficient at very low partial pressure of oxygen ($< 10^{-10}$ Pa) at 900 ˚C [10, 11]. The electronic conductivity of LSM increases linearly with increasing Sr concentration up to maximum of 50 mol %. On the other hand, its TEC values increases with increasing substituent concentration [12, 15]. Carter *et al.* [16] have claimed that the oxygen diffusion coefficient and oxygen surface exchange coefficient of Sr substituted $LaMnO_3$ increases with an increase in Sr substitution on the A-site. For $La_{0.65}Sr_{0.35}MnO_{3\pm\delta}$, oxygen diffusion coefficient is 4×10^{-14} cm^2 s^{-1} at 900 ˚C and increases to 3×10^{-12} cm^2 s^{-1} for $La_{0.50}Sr_{0.50}MnO_{3\pm\delta}$. The activation energy of the oxygen self-diffusion coefficient is 300–350 kJ mol^{-1} for manganite-based perovskites. As far as the chemical reactivity of lanthanum manganite is concerned, it

reacts with YSZ and forms detrimental phases like $La_2Zr_2O_7$ and $SrZrO_3$ at the electrode-electrolyte interface. Since, these phases have high melting point, low thermal conductivity and high thermal expansion coefficient, so, they are undesirable for SOFC applications. The higher concentration of Sr also facilitates the formation of these phases [17-21]. The LSM cathodes were best for the high temperature SOFC. Whereas, for intermediate temperature SOFC (IT-SOFC), the polarization losses in these materials increase and reduce the overall performance of the cell. At low temperatures, the LSM cathodes have low catalytic activity for oxygen reduction reaction mainly due to low oxygen ion conductivity and low oxygen surface exchange coefficient [22-26].

It is believed that IT-SOFCs cathode materials should exhibit mixed (ionic-electronic) conductors. So, various attempts have been made to improve the performance of LSM and new materials are being searched. The various approaches followed so far include:

(a) Replacing the A-site La with various elements (b) to substitute/replace Mn by Fe, Co and Cr to increase the oxygen exchange rate (c) using composite cathode consisting of LSM and an electrolyte to enhance the triple phase boundary.

A lot of research has been carried out to replace A-site cation by other elements like Pr, Nd, Sm, Gd, Yb and Y. Ishihara *et al.* [27] have systematically studied the $Ln_{0.60}Sr_{0.40}MnO_3$ (Ln=La, Pr, Nd, Sm, Gd, Yb or Y). They found that when A site cation is Y or Yb, the electrical conductivity is very low. For Ln=Pr, Nd, Sm and Gd, the conductivity is comparable to $La_{0.60}Sr_{0.40}MnO_{3\pm\delta}$. Even cathode over potential are low in these materials and decreases with decreasing ionic radii of A-site cation i.e. Y has the largest and Pr has the lowest. Sakaki *et al.* [28] have also investigated the chemical reactivity of Gd, Sm, Pr and Nd and reported that formation of secondary phases $Ln_2Zr_2O_3$ is suppressed as La> Gd> Nd> Sm> Pr. It has also been observed that $Gd_{1-x}Sr_xMnO_3$ ($0.1\leq x\leq 0.80$) showed much better compatibility with YSZ although its electrochemical activity and electrical conductivity is similar to that of $La_{1-x}Sr_xMnO_{3\pm\delta}$. With increase in concentration of Sr, conductivity increases but it also enhances the TEC. So, attempts have made out to optimize the TEC and conductivity values of the system. It has been observed that $Ln_{1-x}Sr_xMnO_3$ (Ln=Nd, Pr) for x=0.40, 0.50 shows a TEC of 12.3×10^{-6} $^{\circ}C^{-1}$ with high conductivity values of 226 S cm^{-1} and can be considered as promising cathode for SOFC applications [29. 30]. Huang *et al.* [31] have also reported that A-site deficient $Pr_{0.60-y}Sr_{0.40}MnO_3$ (y>0) are superior to the symmetric one in respect of electrical conductivity and over potentials. The majority of research is

focused on Sr substituted lanthanide manganite. However, Ca substituted cathodes has also proven their potential. They also show chemical stability and conductivity comparable to Sr substituted cathodes [32-34].

As far as B-site substitution is concerned, many researchers have co-substitute Mn with different elements like Sc, Ce, Co and Fe. Yue *et al.* [35] have studied the substitution of Sc on Mn site. They have reported that in $La_{0.80}Sr_{0.20}Mn_{1-x}Sc_xO_{3-\delta}$ (LSMC) ($0 \leq x \leq 0.4$), substitution of Sc introduces the non-stoichiometric defects in the crystal which helps to promote the oxygen ion mobility. In these materials, minor substitution of Sc is beneficial whereas high concentration of Sc (above 10 mol %) reduces the cell performance because of segregation of Sc_2O_3 especially at low temperatures. The high cost of Sc is main concern for its practical use. Noh *et al.* [36] have studied the effect of Cu substitution at Mn site in $La_{0.8}Sr_{0.2}Mn_{1-x}Cu_xO_3$ ($0 \leq x \leq 0.2$). They have observed that Cu substitution enhances the electronic conductivity by converting the Mn^{3+} into Mn^{4+}.

$Sr_{1-x}Ce_xMnO_{3-\delta}$ ($0 \leq x \leq 0.4$) system has also been investigated as a potential cathode for IT-SOFC. The TEC of these systems varies between 12.4×10^{-6} and 10.1×10^{-6} $^{\circ}C^{-1}$. These materials are more compatible with ceria based electrolytes [37]. To improve its properties, Gu et *al.* [38] have proposed the Co doping at B-site i.e. $Sr_{0.80}Ce_{0.20}Mn_{0.80}Co_{0.20}O_{3-\delta}$. The area specific resistance of these cathodes is in the range of 0.10 Ω cm^2 at 750 $^{\circ}C$ which is about 10 times lower than that of $Sr_{0.80}Ce_{0.20}MnO_{3-\delta}$. But Co doping enhances the catalytic activity of oxygen reduction. Liu *et al.* [39] have studied $Bi_{0.5}Sr_{0.5}MnO_3$ (BSM) as a new cathode material for IT-SOFC. They have observed that the conductivity varies between 82–200 S cm^{-1} over the temperature range of 600–800 $^{\circ}C$, generally satisfying the requirement for an IT-SOFC cathode and comparable to that of $La_{0.9}Sr_{0.1}MnO_3$, which is 110–120 S cm^{-1} over the same temperature range. However, BSM reacts with YSZ electrolytes even at 700 $^{\circ}C$, while it is chemically compatible with Sm doped CeO_2 (SDC) electrolytes up to 1050 $^{\circ}C$. Its TEC is 14×10^{-6} $^{\circ}C^{-1}$, which is close to that of doped ceria electrolyte.

2.2 Cobaltite cathodes

Another family of cathodes consist Co at B-site. These materials exhibit peculiar behavior in regard to oxygen non-stoichiometry, catalytic activity, electrical and magnetic properties depending upon the substituent concentration, temperature and oxygen partial pressure [40].

The catalytic properties of the cobaltites are associated with the occupation of *d* orbital electrons near Fermi level (E_F) and with the buildup of surface charge so as to enhance the electron transfer between a surface cation and a potential catalyzed species [41]. $La_{1-x}A_xCoO_{3-\delta}$ (A=Sr, Ca; $0.1 \leq x \leq 0.40$) has very high electrical conductivity (1600 S cm^{-1}) and ionic conductivity due to high oxygen ion diffusivity and high catalytic activity towards oxygen dissociation. However, the reduction of Co and generation of oxygen vacancies at elevated temperatures lead to very high TEC (21×10^{-6} $^{\circ}C^{-1}$) which results in the delamination at cathode/ electrolyte interface [42-44]. To find a solution for this problem, La cation is replaced by other elements like Pr, Nd, Sm and Gd. The TEC of these materials decreases as: Pr>Nd>Sm>Gd. Among different A-site cations $Pr_{1-x}Sr_xCoO_{3-\delta}$ ($0.05 \leq x \leq 0.7$) exhibits maximum conductivity due to extra contribution from oxidation of Pr^{3+} to Pr^{4+} [45]. Chen *et al.* [46] have also proposed Mn doping at Co-site. They have studied $Ln_{0.60}Sr_{0.40}Co_{0.80}Mn_{0.20}O_{3-\delta}$ (Ln=La, Gd, Sm, Nd) and concluded that maximum electrical conductivity (1400 S cm^{-1}) is exhibited by $La_{0.60}Sr_{0.40}Co_{0.80}Mn_{0.20}O_{3-\delta}$ with 18×10^{-6} $^{\circ}C^{-1}$. For Sm based cathode $Sm_{1-x}Sr_xCoO_{3-\delta}$, ($0 \leq x \leq 0.6$) the maximum conductivity is reported around 1000 S cm^{-1} for x=0.50, but these materials have TEC in the range of 20×10^{-6} $^{\circ}C^{-1}$ [47, 48]. Besides the problem of high TEC, the other drawback associated with these materials is their reactivity with YSZ and CeO_2 based electrolytes [49-51].

Some research groups have also reported the substitution of Cu at Co-site. It is believed that it will enhance the ionic conductivity and catalytic activity. However, the doping of Cu results in reduction of electrical conductivity (1400 S cm^{-1}). Zhu *et al.* [52] have studied $Pr_{1-x}Sr_xCo_{1-y}Cu_yO_{3-\delta}$ ($0.1 \leq x \leq 0.5$; $0.0 \leq y \leq 0.2$) and claimed that for x=0.30 and y=0.05-0.30, these cathodes have lower overpotentials as compared to $Pr_{0.70}Sr_{0.30}CoO_{3-\delta}$. The maximum power density is reported around 0.481 W cm^{-2} for these materials.

2.3 Ferrite cathodes

Due to the drawbacks of Co based cathodes, another B-site cation explored for perovskite cathodes is Fe. Fe based cathodes are expected to be more stable than Co based cathode because Fe^{3+} has stable electronic configuration $3d^5$ and chances of conversion of Fe^{3+} to Fe^{4+} are quite low. The electronic properties of the Fe based cathodes are generally explained on the basis of existence of Hubbard or Hubbard like band gap which arise from the electron-electron repulsion at Fe-site. The disproportion of Fe^{3+}/Fe^{4+} or Fe^{3+}/Fe^{2+} is considered to be responsible for this band gap. Due to this configuration, $LaFeO_3$ has semiconducting /semi

metallic properties at high temperature. These materials are p-type or n-type semiconductors at low pO_2. In addition, ferrite based perovskites have low TEC as compared to cobaltites [53-55]. $La_{0.80}Sr_{0.20}FeO_3$ (LSF) is investigated as a potential cathode material in conjunction with anode supported YSZ electrolyte. The maximum power densities achieved with assembly is of the order of 0.80-0.95 W cm^{-2} at 750 ˚C and 0.7V. However, the reactivity of these cathodes with YSZ is quite high due to inter diffusion of Zr and La. So, a layer of $Ce_{0.80}Sm_{0.20}O_{1.9}$ (SDC) is inserted between YSZ and LSF to prevent the chemical diffusion [56-58]. Anderson *et al.* [59] and Ecija *et al.* [60] have studied the reactivity of different lanthanides $Ln_{0.80}M_{0.20}FeO_3$ (Ln=La, Pr, Nd, Sm; M=Sr, Ca) with YSZ. They observed that the interaction between lanthanides and YSZ results in secondary phase formation or incorporation of Zr on to perovskite B site. Among all the lanthanides, $La_{0.80}Ca_{0.20}FeO_3$ is least reactive since it exhibits decrease in dissolution of Zr into perovskite due to smaller unit cell volume. Vidal *et al.* [61] have studied the effect of A-site cation disorder in $Ln_{0.50}M_{0.50}FeO_{3-\delta}$ perovskites (Ln=La, Nd, Pr; M=Sr, Ca and Ba) on the electronic and electrochemical performance for La based materials. They found maximum conductivity and performance for La based materials and concluded that small cationic radii containing cathode materials will react more vigorously with electrolytes.

Coffey *et al.* [62] and Liu *et al.* [63] have investigated the doping of Cu at Fe site and observed that Cu doping enhances the kinetics of electrochemical reduction of oxygen. The cell fabricated by using these cathodes exhibit high power density of 1.75 W cm^{-2} with YSZ electrolyte. Yu *et al.* [64] have recently studied the substitution of Mo at Fe site in $La_{0.60}Sr_{0.40}Fe_{0.90}Mo_{0.1}O_{3-\delta}$. The total conductivity of 159 S cm^{-1} was observed for these materials. But these materials also react with YSZ and form monoclinic insulating ZrO_2 phase.

2.4 Ferrocobaltite cathodes

Ferrites and cobaltites have their own limitations. However, the presence of both the elements in the compound can compensate the limitation of each cation. Fe promotes the ionic conduction whereas; Co enhances the electronic conduction. So, it is believed that their co-doping at B-site can enhance the properties of the resulting material. It is observed that perovskite oxides having a mixture of Fe and Co exhibits metallic character with high Co concentration and semiconductor like behavior with high Fe content [65, 66]. Petric *et al.* [67] have investigated systematically the electrical and thermal expansion data of

$La_{1-x}Sr_xCo_{1-y}Fe_yO_{3-\delta}$ ($0.1 \leq x \leq 0.9$; $0.1 \leq y \leq 1$). The conductivity observed for y=0.1 was maximum and after that it decreases with increasing Fe content. The oxygen self-diffusion coefficient of these cathodes is 2.6×10^{-9} cm^2 s^{-1} at 500 ˚C which is much better than conventionally used LSM cathodes. They also claimed that Sr concentration mainly controls the ionic conductivity. On the other hand TEC of the samples and electronic conductivity depends on the Fe and Co content. These materials are also not compatible with YSZ electrolytes due to undesirable interfacial reaction. Generally, a layer of $Ce_{0.80}Gd_{0.20}O_{1.9}$ (CGO) is introduced between the cathode and electrolyte to prevent the formation of desirable phases [68, 69]. Yokokawa *et al.* [70] have observed that degradation rate of these materials depend upon the diffusion of Sr, so, lower concentration of Sr can decrease the reactivity. Hansen *et al.* [71] have tested the A site non stoichiometric materials $(La_{0.60}Sr_{0.40})_{1-x}Fe_{0.8}Co_{0.2}O_{3-\delta}$ ($0.01\leq x\leq0.20$) as cathode for SOFC applications. They observed that TEC decreases with increase in A –site deficiency. The lowest TEC was observed for x=0.20 i.e. 17.3×10^{-6} ˚C^{-1}. Lowering of A site stoichiometry also reduces area specific resistance (ASR.). The highest electrocatalytic activity was achieved for x=0.85 concentration with ASR of 14.8 Ω cm^2. This reduction was thought to be due to the lowering of surface segregation of A-site cations. Due to higher TEC and high reactivity, La based cathodes are not desirable for long duration [72]. Moreover, these materials are also found to be prone to Cr poisoning after 10,000 h SOFC stack testing [73]. Meng *et al.* [74, 75] have replaced the La by Pr and studied the performance of $Pr_{1-x}Sr_xCo_{0.80}Fe_{0.20}O_{3-\delta}$ (PSCF; $0.20\leq x\leq0.60$). The highest conductivity for x=0.40 was observed around 1040 S cm^{-1}. the ASR of the cells were observed around 0.046 Ω cm^2 and power density of the cells were about 303 mW cm^{-2} at 700 ˚C. Despite of the higher power density and low ASR, the problem of reactivity with electrolyte was also not solved in these systems.

From the above points, it is clear that lanthanides did not give satisfactory results. Haile and Shao [76, 77] proposed a cathode containing alkaline earth metal at A site. They employed $Ba_{0.50}Sr_{0.50}Co_{0.80}Fe_{0.20}O_{3-\delta}$ (BSCF) as a cathode material first time in IT-SOFC. The power density of these materials was obtained around 402 mW cm^{-2} for anode supported cell consisting of a NiO-SDC anode and SDC electrolyte. The ASR values of these materials were 0.055-0.071 Ω cm^2 at 600 ˚C. The higher power density and lower ASR values as compared to conventional LSM made these materials as a potential candidate for SOFC applications. The major disadvantage associated with these cathodes is their high TEC 20×10^{-6} ˚C^{-1} which is common problem of cobalt containing materials. Zhou *et al.* [78] have

reported that TEC of BSCF can be reduced by introducing A-site deficiency $(Ba_{0.5}Sr_{0.5})_{1-x}Co_{0.8}Fe_{0.2}O_{3-\delta}$ ($0.05 \leq x \leq 0.20$). They observed that TEC decreases with increasing A-site deficiency. Li *et al.* [79, 80] have also reported the effect of doping of a rare earth metal ion at A-site of BSCF with the formation of $(Ba_{0.5}Sr_{0.5})_{1-x}Sm_xCo_{0.8}Fe_{0.2}O_{3-\delta}$ ($0.05 \leq x \leq 0.20$). The conductivity was improved up to 21.3 % and total resistance values also decreases up to 50 % by these substitutions. However, high TEC problem still persists, infact it increases with substitutions. Kuroda *et al.* [81] have studied the $GdBa_{0.5}Sr_{0.5}Co_{2-x}Fe_xO_{5+\delta}$ ($0 \leq x \leq 0.2$) perovskites. The conductivity of the order of 1000 S cm^{-1} was observed for these materials. Simultaneously, these materials also exhibit high TEC values. Sarra *et al.* [82] and Sweirczek [83] have studied the several elements at A-site in $A_{0.68}Sr_{0.3}FeO_{0.8}Co_{0.2}O_{3-\delta}$ (A=La, Pr, Sm, Nd, Er, Eu, Gd, Dy and Ba). They observed that at high temperatures (900 ˚C) La and Pr are the best performing materials achieving values of 1.4 and 1.25 A cm^{-2} at 0.8 V and 900 ˚C. However, at low temperatures (650 ˚C), Ba, Sm and Pr shows almost similar behavior. The activation energy is lower for Ba and Sm as compared to Pr. This may be due to the catalytic activity of surface species involved in oxygen reduction and incorporation into crystal lattice. Liu *et al.* [84] have also studied the A-site deficient $Ba_{1-x}Co_{0.7}Fe_{0.2}NiO_{3-\delta}$ ($0 \leq x \leq 0.2$) cathode for IT-SOFCs. These materials exhibit very low polarization resistance of 0.283 and 0.046 Ω cm^2 at 500 and 600 ˚C. These materials are compatible with the Gd doped CeO_2 and no secondary phase was observed at 1050 ˚C.

Moreover, the main problem with BSCF materials is the high reactivity of alkaline metals with CO_2 [85, 86]. These cathodes are susceptible to vigorous reaction at very low content of CO_2. It was observed that presence of CO_2 reduces the oxygen reduction process over BSCF cathode and decreases the cell performance. When hydrocarbons are used, large amount of CO_2 is produced so, these materials are not suitable for single chamber SOFC [87-90].

2.5 Nickelate cathodes

All the materials containing Co have overall high TEC and are very reactive towards CO_2. Researchers are trying hard to get adequate ionic conductivity from Co free cathodes. To solve this problem Ni based cathodes have been developed. These materials have significant electronic conductivity and low TEC as compared to cobaltites. The nickel based materials also do not under go any interfacial reaction with YSZ as Ni-YSZ based anodes are being used in SOFC [91]. Undoped $LaNiO_{3-\delta}$ is stable only below 950 ˚C. Further heating leads to the formation of complex K_2NiF_4-type structure [92-94]. So, Fe is substituted at Ni site to

make these structures stable. $LaFe_{1-x}Ni_xO_{3-\delta}$ ($0 \leq x \leq 0.2$) exhibits a conductivity of 580 S cm^{-1} and TEC in the range of 11.4×10^{-6} $^{\circ}C^{-1}$ [95-97]. Zhang *et al.* [98] have studied $La_{0.60}Sr_{0.40}Fe_xNi_{1-x}O_{3-\delta}$ (LSNF) ($0 \leq x \leq 0.20$) compound for cathode material. The maximum conductivity of 160 S cm^{-1} is obtained for x=0.10 concentration. The maximum power densities of 0.405 W cm^{-2} at 700 ˚C, 0.238 W cm^{-2} at 650 ˚C and 0.140 W cm^{-2} at 600 ˚C, respectively was obtained. Addition of Fe makes these materials more reactive towards ZrO_2 based electrolytes [99, 100]. Wang *et al.* [101] have also studied the Co doping at Ni- site. The conductivity of these materials is above 1150 S cm^{-1} with average TEC of 17.22×10^{-6} $^{\circ}C^{-1}$. However, these materials are susceptible to Cr poisoning.

2.6 K_2NiF_4 structured cathodes

Other than perovskite based oxides, materials belonging to K_2NiF_4 structure are also being developed for SOFC cathode. Many materials of formulae $A_2BO_{4+\delta}$ (A=La, Ba; B=Co, Ni) have been studied for cathode [102-107]. A high concentration of oxygen interstitials offer the possibility of rapid exchange transport and thus provide a new type of mixed ionic electronic conductor. These materials show a conductivity of about 100 S cm^{-1} at 800 ˚C under high oxygen partial pressures. Doping at La site with alkaline earth metals (Sr, Ca and Ba) and doping of Cu or Co at B-site may lead to improvement in the structural and electrical properties [108, 109]. $La_2Ni_{1-x}Cu_xO_{4+\delta}$ ($0 \leq x \leq 0.2$) has been evaluated as a cathode material. The TEC and conductivity are in the range of 13×10^{-6} $^{\circ}C^{-1}$ and 87 S cm^{-1}, respectively. Lower ASR values 0.17 Ω cm^2 is obtained for these materials. These materials are susceptible to reactions with YSZ and CO_2.

2.7 Composite cathodes

As discussed above, no single material is able to give satisfactory results for long duration in SOFCs. So, researchers are now also working on the composite cathodes. Composites of cathode materials and electrolytes are fabricated and studied for their performance as cathode material. To improve the electrocatalytic activity of LSM cathodes, an ion conducting secondary phase of YSZ or GDC (Gd doped CeO_2) was introduced to form a composite cathode. It has been observed that resistance values can be lowered up to a quarter by adding 50 wt % YSZ to LSM cathode [110, 111]. It has been reported that 50 wt % addition of GDC instead of YSZ reduces the resistance to 0.49 Ω cm^2 which is two times lower than for LSM-YSZ composite [112, 113]. Yi and Choi [114] have studied $La_{0.9}Sr_{0.1}MnO_3/La_{0.9}Sr_{0.1}Ga_{0.8}Mg_{0.2}O_3$. In these composite cathodes electrode resistance and

cathode overpotential both increase due to reduction in porosity in composite cathode as compared to LSM cathode. $La_{0.60}Sr_{0.40}Co_{0.20}Fe_{0.8}O_{3-\delta}$-$Ce_{0.80}Sm_{0.20}O_{1.9}$ (LSCF-SDC) and LSCF-$Gd_{0.1}Ce_{0.9}O_{1.9}$ composite cathodes have also been developed and studied for IT-SOFC. The ASR values obtained for these cathodes are in the range of 0.1Ω cm^2 and a power density of 0.311 W cm^{-2} was obtained [115-117]. (LaSr)$Fe_{1-x}Ni_xO_{3-\delta}$ ($0.0\leq x\leq 0.2$)-$Ce_{0.90}Gd_{0.10}O_{2-\delta}$ composites were also developed. The electrical conductivity of the order of 84 S cm^{-1} was obtained for these compounds [118]. $Ba_{0.5}Sr_{0.5}Co_{0.8}Fe_{0.2}$-$O_{3-\delta}$-$Sc_{0.1}Zr_{0.9}O_{1.95}$ composite cathodes have also been developed for zirconia based electrolytes. The polarization resistance of about 0.08 Ω cm^2 was observed in these materials [119]. Yang *et al.* [120] and Wu *et al.* [121] have reported high performance of $Sm_{0.5}Sr_{0.5}CoO_{3-\delta}$–$BaZr_{0.1}Ce_{0.7}Y_{0.2}O_{3-\delta}$ (SSC–BZCY) and $Sm_{0.5}Sr_{0.5}CoO_{3-\delta}$–$BaCe_{0.8}Sm_{0.2}O_{3-\delta}$ (SSC–BCS) composite cathodes for SOFCs with $BaZr_{0.1}Ce_{0.7}Y_{0.2}O_{3-\delta}$ (BZCY) and $BaCe_{0.8}Sm_{0.2}O_{3-\delta}$ (BCS) being used as the respective electrolytes. The main drawback of these cathodes is the reduction in their performance and low electrical conductivity. Moreover, presence of alkaline earth metal is also susceptible to CO_2 and H_2O reactivity.

The addition of noble metals such as Ag, Pd and Pt to the cathode materials can enhance the catalytic activity and reduce the electrode polarization losses. Several cathodes like [LSM-Ag], [$Bi_2V_{0.9}Cu_{0.1}O_{5.95}$-Ag], [$La_{0.6}Sr_{0.4}Co_{0.8}Fe_{0.2}O_3$-CGO-Ag], [LSCF-Pd], [$La_{0.8}Sr_{0.2}FeO_{3-\delta}$-$Ce_{0.8}Sm_{0.2}O_{1.9}$], [(BaSr)(CoFe)$O_3$-Ag] have been investigated [122-127]. The performance of cathode noble metals strongly depends upon their particle size, distribution and crystallinity. However, the stability and life time of these cathodes under SOFC operating conditions are main concerns [128].

The basic properties and limitations of some of the key cathode materials are summarized in table 2.1.

From the above discussion, it can be concluded that there is no single material which can fulfill the requirement of SOFC as cathode material. Researchers have investigated many materials for this purpose. However, still there are some gaps in the study which requires further investigations. These gaps are given below:

- Limited work is done with bismuth based cathode materials.
- Effect of doping at the A-site of $BiMnO_3$ have not been explored fully which can be more useful to improve their properties.

- B site cation can be replaced by other transition elements to improve their electrical and structural properties.

Table 2.1: Cathode materials: thermal expansion coefficient (TEC), electronic conductivity (σ_e), ionic conductivity (σ_i) and their limitations.

Composition	**TEC ($\times 10^{-6}$) $^{\circ}C^{-1}$**	**T ($^{\circ}C$)**	**σ_e (S cm^{-1})**	**σ_i (S cm^{-1})**	**Limitations**
$La_{1-x}Sr_xMnO_{3-\delta}$ ($0.2 \leq x \leq 0.8$)	11.8	900	300	5.93×10^{-7}	• High cathode overpotentials for IT SOFC applications. • Low ionic conductivity. • Undesirable phases $La_2Zr_2O_7$, $SrZrO_3$ are formed during operation.
$Pr_{1-x}Sr_xMnO_{3-\delta}$ ($0.05 \leq x \leq 0.7$)	12	950	220	-	• Low ionic conductivity. • Not compatible with GDC and YSZ electrolytes.
$Bi_{0.5}Sr_{0.5}MnO_{3-\delta}$	14.7	800	180	4.97×10^{-4}	• Reacts with YSZ. • High thermal expansion coefficient.
$La_{0.8}Sr_{0.2}CoO_{3-\delta}$	20.5	800	1650	2.2×10^{-1}	• High TEC. • Reacts with most of the electrolytes.
$La_{0.8}Sr_{0.2}FeO_{3-\delta}$	12.2	750	155	-	• Low power density. • High TEC. • Reacts with YSZ.
$La_{0.8}Sr_{0.2}Fe_{0.8}Co_{0.2}FeO_{3-\delta}$	15.4	600	125	-	• High TEC. • Reacts with all electrolytes. • High ASR.
$La_{0.8}Sr_{0.2}Fe_{0.2}Co_{0.8}FeO_{3-\delta}$	20.1	600	1050	-	• High TEC. • Reacts with all electrolytes.
$La_{0.8}Sr_{0.2}Mn_{0.2}Co_{0.8}FeO_{3-\delta}$	18.1	500	1400	5.8×10^{-2}	• High TEC. • Low catalytic reaction. • Reacts with YSZ.
$Pr_{0.8}Sr_{0.2}Co_{0.2}Fe_{0.8}FeO_{3-\delta}$	14.8	800	76	1.5×10^{-3}	• Low electronic conductivity. • High ASR • Reacts with electrolytes. • High TEC.
$Pr_{0.8}Sr_{0.2}Co_{0.2}Mn_{0.8}FeO_{3-\delta}$	11.1	800	200	4.4×10^{-5}	• Low ionic conductivity. • High ASR. • Reacts with electrolytes.
$Ba_{0.5}Sr_{0.5}Co_{0.8}Fe_{0.2}O_{3-\delta}$	20	500	30	-	• Low electronic conductivity • High TEC • Reacts with electrolytes. • Highly susceptible to CO_2 and H_2O.
$La_{1.2}Sr_{0.8}NiO_{4+\delta}$	13.7	800	100	-	• High TEC. • High polarization resistance • Low catalytic activity.

2.8 Plan of the work

Based on above discussion on literature, it can be observed that La based materials are the promising candidate for the high temperature SOFC applications. However, these materials suffer from high polarization losses and low oxygen reduction rate at low temperatures. Since Bi^{3+} and La^{3+} have almost same ionic radii, so, replacement of La^{3+} (1.16 Å) by Bi^{3+} (1.17 Å) can be helpful because bismuth based compounds are mixed conductors and also have high catalytic reactivity towards oxygen reduction. Moreover, despite of the same ionic radii of Bi^{3+} and La^{3+}, bismuth based perovskites have different properties due to high polarizable lone electron pair of bismuth. Apart from this, the work on $BiMnO_3$ as a cathode material is also limited. By considering these facts, in this work, it has been planned to investigate the bismuth based materials and check the feasibility as a possible cathode materials for SOFC applications. The effect of different substituents at A-site has been investigated. Even the effect of different B-site cations on structural and thermal properties has also been studied. The main objectives of the present work are:

- To synthesize $Bi_{1-x}M_xMnO_{3\pm\delta}$, $Bi_{1-x}M_xCrO_{3\pm\delta}$, $Bi_{1-x}M_xFeO_{3\pm\delta}$ and $Bi_{1-x}M_xYO_{3\pm\delta}$ samples (M=Ca, Sr; x=0.40, 0.45, 0.50, 0.55) by solid state reaction method.

- These materials have been characterized for phase identification, thermal stability, conductivity and thermal expansion using different techniques.

- Selected samples were investigated for their suitability as a cathode material using interaction study with YSZ electrolyte.

To achieve the above mentioned objectives, the samples were synthesized by solid state reaction method and characterized by different techniques. The synthesis conditions and characterization techniques used in this work are discussed in the next chapter. The results of the present system and discussions related to them are presented in chapter 4 and 5. In the end of the thesis, the conclusion and future scope of the present studied systems is given.

References

[1] H. H. Mobius, J. Solid State Electrochem. 1 (1997) 2.

[2] S. K. Lau, S. C. Singhal, Corrosion 85 (1985) 1.

[3] S. B. Adler, Chem. Rev. 104 (2004) 4791.

[4] J. M. Ralph, A. C. Schoeler, M. Krumpelt, J. Mater. Sci. 36 (2001) 1161.

[5] N. Q. Minh, T. Takahashi, Science and technology of ceramic fuel cells (1995) Elsevier Amsterdam.

[6] J. Mizusaki, H. Tagawa, K. Naraya, T. Sasamoto, Solid State Ionics 49 (1991) 111.

[7] J. Mizusaki, Solid State Ionics 52 (1992) 79.

[8] J. H. Kuo, H. U. Anderson, D. M. Sparlin, J. Solid State Chem. 83 (1989) 52.

[9] H. U. Anderson, Solid State Ionics 52 (1992) 33.

[10] J. Mizusaki, N. Mori, H. Takai, Y. Yonemura, H. Minamiue, H. Tagawa, M. Dokiya, H. Inaba, K. Naraya, T. Sasamoto, T. Hashimoto, Solid State Ionics 129 (2000) 163.

[11] S. Miyoshi, J. Hong, K. Yashiro, A. Kaimai, Y. Nigara, K. Kawamura, T. Kawada, J. Mizusaki, Solid State Ionics 154 (2002) 155.

[12] S. P. Jiang, J. Mater. Sci. 43 (2008) 6799.

[13] Z. Li, M. Behruzi, L. Fuerst, D. Stover, In: S. C. Singhal, H. Iwahara, SOFC-III Edt. 3 (1993) The Electrochemical Society Inc. Pennington New Jersey.

[14] Z. T. Zhang, O. Y. Lin, Z. L. Tang, In: M. Dokiya, H. Tagawa, S. C. Singhal, SOFC-IV Edt. 3 (1995) The Electrochemical Society, Pennington New Jersey.

[15] J. Mizusaki, Y. Yonemura, H. Kamata, K. Ohyama, N. Mori, H. Takai, H. Tagawa, M. Dokiya, K. Naraya, T. Sasamoto, H. Inaba, T. Hashimoto, Solid State Ionics 132 (2000) 167.

[16] S. Carter, A. Selcuk, R. J. Chater, J. Kajda, J. A. Kilner, B. C. H. Steele, Solid State Ionics 53 (1992) 597.

[17] S. P. Jiang, J. P. Zhang, Y. Ramprakash, D. Milosevic, K. Wilshier, J. Mater. Sci. 35 (2000) 2735.

[18] C. Clausen, C. Bagger, J. B. Bildesorensen, A. Horsewell, Solid State Ionics 70 (1994) 59.

[19] G. Stochniol, E. Syskakis, A. Naoumidis, J. Amer. Ceram. Soc. 78 (1995) 929.

[20] T. Setoguchi, T. Inoue, H. Takebe, K. Eguchi, K. Morinaga, H. Arai, Solid State Ionics 37 (1990) 217.

[21] A. Mitterdorfer, L. J. Gauckler, Solid State Ionics 111 (1998) 185.

[22] A. Orera, P.R. Slater, Chem. Mater. 22 (2010) 675.

[23] B.C.H. Steele, Solid State Ionics 129 (2000) 95.

[24] Y. Zheng, R. Ran, H.X. Gu, R. Cai, Z.P. Shao, J. Power Sources 185 (2008) 641.

[25] Y. Zheng, C.M. Zhang, R. Ran, R. Cai, Z. P. Shao, D. Farrusseng, Acta Mater. 57 (2009) 1165.

[26] Y. Zheng, R. Ran, Z. P. Shao, J. Phys. Chem. C 112 (2008) 18690.

[27] T. Ishihara, T. Kudo, H. Matsuda, Y. Takita, J. Am. Ceram. Soc. 77 (1994) 1682.

[28] Y. Sakaki, Y. Takeda, A. Kato, N. Imanishi, O. Yamamoto, M. Hattori, M. Iio, Y. Esaki, Solid State Ionics 118 (1999) 187.

[29] G. Ch. Kostogloudis, C. Ftikos, J. Eur. Ceram. Soc. 19 (1999) 497.

[30] G. Ch. Kostogloudis, N. Vasilakos, C. Ftikos, J. Eur. Ceram. Soc. 17 (1997) 1513.

[31] K. Q. Huang, M. Feng, J. B. Goodenough, M. Schmerling, J. Electrochem. Soc. 143 (1996) 3630.

[32] W. Lee , J. W. Han, Y. Chen, Z. Cai, B. Yildiz, J. Am. Chem. Soc. 135 (2013) 7909.

[33] H. Rim, S. Jeung, E. Jung, J. Lee, Mat. Chem. Phy. 52 (1998) 54.

[34] X. Ding, L. Gau, Y. Liu, Y. Zhen, L. Guo, J. Electroceram. 18 (2007) 317.

[35] X. L. Yue, A. Y. Yan, M. Zhang, L. Liu, Y. L. Dong, M. J. Cheng, J. Power Sources 185 (2008) 691.

[36] T. Noh, J. Ryu, R. O. Hayre, H. Lee, Solid State Ionics 260 (2014) 30.

[37] S. Hashimoto, H. Iwahara, J. Electroceram. 4 (1999) 225.

[38] H. Gu, H. Chen, L. Gao, Y. Zheng, X. Zhu, L. Guo, Int. J. Hydrogen Energy 33 (2008) 4681.

[39] B. Liu, Z. Jiang, B. Ding, F. Chen, C. Xia, J. Power Sources 196 (2011) 999.

[40] W. Zhou, R. Ran, Z. Shao, J. Power Sources 192 (2009) 231.

[41] I. Kojima, H. Adachi, I. Yasumori, Surf. Sci. 130 (1983) 50.

[42] A. N. Petrov, O. F. Kononchuk, A. V. Andreev, V. A. Cherepanov, P. Kofstad, Solid State Ionics 80 (1995) 189.

[43] Y. Takeda, R. Kanno, M. Noda, O. Yamamoto, Bull. Inst. Chem. Res. 64 (1986) 157.

[44] A. Weber, E. Ivers-Tiffee, J. Power Sources 127 (2004) 273.

[45] F. Riza, C. Ftikos, F. Tietz, W. J. Fischer, J. Eur. Ceram. Soc. 21 (2001) 769.

[46] W. X. Chen, T. L. Wen, H. W. Nie, R. Zheng, Mater. Res. Bull. 38 (2003) 1319.

[47] H. Fukunaga, M. Koyama, N. Takahashi, C. Wen, K. Yamada, Solid State Ionics 132 (2000) 279.

[48] I. Park, J. Im, J. Choi, J. Ahn, D. Shin, Solid State Ionics 184 (2011) 35.

[49] T. Ishihara, M. Honda, T. Shibayama, H. Minami, H. Nishiguchi, V. Takita, J. Electrochem. Soc. 145 (1998) 3177.

[50] C. Rossignol, J. M. Ralph, J. M. Bae, J. T. Vaughey, Solid State Ionics 175 (2004) 59.

[51] E. H. Kim, H. J. Jung, K. S. An, J. Y. Park, J. Lee, D. Hwang, J. Y. Kim, M. J. Leed, Y. Kwona, J. H. Hwang, Ceram. Int. 40 (2014) 7817.

[52] C. J. Zhu, X. M. Liu, D. Xu, D. T. Yan, D. Y. Wang, W. H. Su, Solid State Ionics 179 (2008) 1470.

[53] X. D. Zhou, H. U. Anderson, SOFC-IX: Solid oxide fuel cells IX, Electrochemical Society Proceedings Quebec PQ Canada (2005) 1479.

[54] S. P. Simner, J. F. Bonnett, N. L. Canfield, K. D. Meinhardt, J. P. Shelton, V. L. Sprenkle, J. W. Stevenson, J. Power Sources 113 (2003) 1.

[55] A. Chainani, M. Mathew, D. D. Sarma, Phys. Rev. B 48 (1993) 14818.

[56] S. P. Simner, J. F. Bonnett, N. L. Canfield, K. D. Meinhardt, V. L. Sprenkle, J. W. Stevenson, Electrochem. Solid-State Lett. 5 (2002) A173.

[57] S. P. Simner, M. D. Anderson, L. R. Pederson, J. W. Stevenson, J. Electrochem. Soc. 152 (2005) A1851.

[58] A. M. Amesti, A. Larranaga, L. M. Rodriguez-Martínez, A. T. Aguayo, J. L. Pizarro, M. L. No, A. Laresgoiti, M. I. Arriortua, J. Power Sources 185 (2008) 401.

[59] M. D. Anderson, J. W. Stevenson, S. P. Simner, J. Power Sources 129 (2004) 188.

[60] A. Ecija , K. Vidal, A. Larranaga, A. Martinez-Amesti , L. Ortega-San-Martin , M. I. Arriortua, Solid State Ionics 201 (2011) 35.

[61] K. Vidal, L. M. Rodriguez-Martinez, L. Ortega-San-Martin, M. L. No, T. Rojo, M. I. Arriortua, Fuel Cells 11 (2011) 51.

[62] G. Coffey, J. Hardy, O. Marina, L. Pederson, P. Rieke, E. Thomsen, Solid State Ionics 175 (2004) 73.

[63] J. Lu, Y. M. Yin, Z. F. Ma, Int. J. Hydrogen Energy 38 (2013) 10527.

[64] T. Yu, X. Mao, G. Ma, Ceram. Int. 40 (2014) 13747.

[65] Y. Guo, Y. Zhou, D. Chen, H. Shi, R. Ran, Z. Shao, J. Power Sources 196 (2011) 5511.

[66] J. Pena-Martinez, D. Marrero-Lopez, J. C. Ruiz-Morales, P. Nunez, C. Sanchez-Bautista, A. J. Dos Santos-Garcia, J. Canales-Vazquez, Int. J. Hydrogen Energy 34 (2009) 9486.

[67] A. Petric, P. Huang, F. Tietz, Solid State Ionics 135 (2000) 719.

[68] V. A. C. Haanappel, J. Mertens, A. Mai, J. Fuel Cell Sci. Technol. 3 (2006) 263.

[69] S. Uhlenbruck, T. Moskalewicz, N. Jordan, H. J. Penkalla, H. P. Buchkremer, Solid State Ionics 180 (2009) 418.

[70] H. Yokokawa, H. Sakai, T. Horita, K. Yamaji, M. E. Brito, H. Kishimoto, J. Alloys Compd. 452 (2008) 41.

[71] K. K. Hansen, K. V. Hansen, Solid State Ionics 178 (2007) 1379.

[72] Z. Zhao, L. Liu, X. Zhang, W. Wua, B. Tu, D. Cui, D. Ou, M. Cheng, Int. J. Hydrogen Energy 38 (2013) 1536.

[73] J. A. Schuler, Z. Wuillemin, A. H. Wyser , C. Comminges, N. Y. Steinere, J. V. Herle, J. Power Sources 211 (2012) 177.

[74] X. W. Meng, S. Q. Lv, Y. Ji, W. Tao, Y. L. Zhang, J. Power Sources 183 (2008) 581.

[75] G.C. Kostogloudis, C. Ftikos, Solid State Ionics 135 (2000) 537.

[76] Z. P. Shao, S. M. Haile, Nature 431 (2004) 170.

[77] Z. P. Shao, S. M. Haile, J. Ahn, P.D. Ronney, Z. L. Zhan, S. A. Barnett, Nature 435 (2005) 795.

[78] W. Zhou, R. Ran, Z. P. Shao, W. Q. Jin, N.P. Xu, J. Power Sources 182 (2008) 24.

[79] S. Li, Z. Lu, X. Huang, B. Wei, W. Su, Solid State Ionics 178 (2007) 417.

[80] S. Li, Z. Lü, N. Ai, K. Chen, W. Su, J. Power Sources 165 (2007) 97.

[81] C. Kuroda, K. Zheng, K. Swierczek, Int. J. Hydrogen Energy 38 (2013) 1027.

[82] J. M. Serra, V. B. Vert, M. Betz, V. A. C. Haanappel, W. A. Meulenberg, F. Tietz, J. Electrochem. Soc. 155 (2008) B207.

[83] K. S. Wierczek, J. Power Sources 196 (2011) 7110.

[84] Z. Liu, L. Cheng, M. F. Han, J. Power Sources 196 (2011) 868.

[85] V. V. Kharton, A. A. Yaremchenko, A. V. Kovalevsky, A. P. Viskup, E. N. Naumovich, P. F. Kerko, J. Membrane Sci. 163 (1999) 307.

[86] M. F. Carolan, P. N. Dyer, J. M. LaBar, R. M. Thorogood, US Patent 5 (1993) 473.

[87] C. Xia, Y. Lang, G. Meng, Fuel Cells 4 (2004) 41.

[88] A. Y. Yan, M. J. Cheng, Y. L. Dong, W. S. Yang, V. Maragou, S. Q. Song, P. Tsiakaras, Appl. Catal. B 66 (2006) 64.

[89] A. Yan, M. Yang, Z. Hou, Y. Dong, M. Cheng, J. Power Sources 185 (2008) 76.

[90] A. Yan, B. Liu, Y. Dong, Z. Tian, D. Wang, M. Cheng, Appl. Catal. B 80 (2008) 24.

[91] S. W. Jung, J. M. Vohs, R. J. Gorte, J. Electrochem. Soc. 154 (2007) B1270.

[92] M. Zinkevich, F. Aldinger, J. Alloys Compd. 375 (2004) 147.

[93] R. Chiba, F. Yoshimura, Y. Sakurai, Solid State Ionics 124 (1999) 281.

[94] E. V. Tsipis, E. A. Kiselev, V. A. Kolotygin, J. C. Waerenborgh, V. A. Cherepanov, V. V. Kharton, Solid State Ionics 179 (2008) 2170.

[95] R. Chiba, F. Yoshimura, Y. Sakurai, Solid State Ionics 124 (1999) 281.

[96] R. Chiba, F. Yoshimura, Y. Sakurai, Solid State Ionics 152 (2002) 575.

[97] H. Orui, K. Watanabe, R. Chiba, M. Arakawa, J. Electrochem. Soc. 151 (2004) A1412.

[98] F. Zhang, Z. Yang, H. Wang, W. Wang, G. Ma, Fuel Cells 12 (2012) 749.

[99] T. Komatsu, H. Arai, R. Chiba, K. Nozawa, M. Arakawa, K. Sato, Electrochem. Solid-State Lett. 9 (2006) A9.

[100] T. Komatsu, H. Arai, R. Chiba, K. Nozawa, M. Arakawa, K. Sato, J. Electrochem. Soc. 154 (2007) B379.

[101] F. Wang, D. Yan, W. Zhang, B. Chi, J. Pu, L. Jian, Int. J. Hydrogen Energy 38 (2013) 646.

[102] S. J. Skinner, J. A. Kilner, Solid State Ionics 135 (2000) 709.

[103] F. Zhao, X. F. Wang, Z. Y. Wang, R. R. Peng, C. R. Xia, Solid State Ionics 179 (2008) 1450.

[104] M. Daroukh, V. V. Vashook, H. Ullmann, F. Tietz, I. A. Raj, Solid State Ionics 158 (2003) 141.

[105] A. Aguadero, J. A. Alonso, M. J. Esudero, L. Daza, Solid State Ionics 179 (2008) 393.

[106] Y. Rao, Z. Wang, L. Chen, R. Wu, R. Peng, Y. Lu, Int. J. Hydrogen Energy 38 (2013) 14329.

[107] Y. Hua, Y. Bouffanais, L. Almar, A. Morata, A. Tarancon, G. Dezanneau, Int. J. Hydrogen Energy 38 (2013) 3064.

[108] C. Jin, J. Liu, J. Alloys Compd. 474 (2009) 573.

[109] S. L. Ping, L. Qiang, H. L. Hua, Z. Hui, Z. G. Ying, L. Nan, J. P. Viricelle, C. Pijolat, J. Power Sources 196 (2011) 5835.

[110] T. Kenjo, M. Nishiya, Solid State Ionics 57 (1992) 295.

[111] E. P. Murray, T. Tsai, S. A. Barnett, Solid State Ionics 110 (1998) 235.

[112] E. P. Murray, S. A. Barnett, Solid State Ionics 143 (2001) 265.

[113] M. Balaguer, V. B. Vert, L. Navarrete, J.M. Serra, J. Power Sources 223 (2013) 214.

[114] J. Y. Yi, G. M. Choi, J. Eur. Ceram. Soc. 24 (2004) 1359.

[115] Y. M. Park, J. H. Kim, H. Kim, Int. J. Hydrogen Energy 36 (2011) 9169.

[116] J. G. Lee, M. G. Park, J. H. Park, Y. G. Shul, Ceram. Int. 40 (2014) 8053.

[117] E. Zhao, Z. Jia, X. Liu, K. Gao, H. Huo, Y. Xiong, Ceram. Int. (2014) DOI: 10.1016/j.ceramint.2014.06.084.

[118] F. Zhang, Z. Yang, H. Wang, W. Wang, G. Ma, Fuel Cells 12 (2012) 749.

[119] S. O. Lee, D. Lee, I. Jung, D. Kim, S. H. Hyun, J. Kim, J. Moon, Int. J. Hydrogen Energy 38 (2013) 9320.

[120] L. Yang, C. D. Zhou, S. Z. Wang, Z. Cheng, M. L. Lui, Adv. Mater. 20 (2008) 3280.

[121] T. Z. Wu, R. R. Peng, C. R. Xia, Solid State Ionics 179 (2008) 1505.

[122] C. R. Xia, M. L. Liu, Adv. Mater. 14 (2002) 521.

[123] S. R. Wang, T. Kato, S. Nagata, T. Honda, T. Kaneko, N. Iwashita, M. Dokiya, Solid State Ionics 146 (2002) 203.

[124] Y. Sakito, A. Hirano, N. Imanishi, Y. Takeda, O. Yamamoto, Y. Liu, J. Power Sources 182 (2008) 476.

[125] S. P. Simner, J. F. Bonnett, N. L. Canfield, K. D. Meinhardt, J. P. Shelton, V. L. Sprenkle, J. W. Stevenson, J. Power Sources 113 (2003) 1.

[126] R. Su, Z. Lu, S. P. Jiang, Y. Shen, W. Su, K. Chen, Int. J. Hydrogen Energy 38 (2013) 2413.

[127] Z. Wang, C. Xu, Z. Lou, J. Qiao, B. Ren, K. Sun, Int. J. Hydrogen Energy 38 (2013) 1074.

[128] V. A. C. Haanappel, D. Rutenbeck, A. Mai, S. Uhlenbruck, D. Sebold, H. Wesemeyer, B. Röwekamp, C. Tropartz, F. Tietz, J. Power Sources 130 (2004) 119.

Chapter 3

EXPERIMENTAL PROCEDURE

Overview

This chapter describes the details of the materials used in synthesis followed by their processing and different characterization techniques used for the analysis. The samples were synthesized by conventional solid state reaction method. The as synthesized samples were characterized by X-ray diffraction for phase identification. The Rietveld refinement of all the samples were performed to confirm the symmetry and to calculate unit cell parameters. Raman and Fourier transform infrared spectroscopy were performed to get an insight into the structural changes. The X-ray photoelectron spectroscopy was used to know the oxidation state of the transition elements. The concentration of the oxygen vacancies and the mixed state of the transition element was determined by iodometric titration. The thermal stability of all the samples was studied by differential thermal analyzer, thermogravimetric analysis and dilatometery. The morphology and interfacial study during the interaction study was done by scanning electron microscopy and X-ray dot mapping. The conductivity data with respect to temperature was obtained by two probe set up using impedance analyzer.

3.1 Raw materials

In the present study, the initial materials used for sample preparation were Bi_2O_3, CaO, SrO, $MnCO_3$, Fe_2O_3, Y_2O_3 and Cr_2O_3. All the materials were of 99.99 % purity and were procured from Sigma Aldrich. The YSZ powder was procured from TZ-8YS, Tosoh for interaction study. All these materials were used without any further purification.

3.2 Sample preparation

The samples were prepared by conventional solid state reaction method. For each system, required amount of raw materials as per their stoichiometry ratio were taken. The powders were mixed thoroughly in an agate mortar pestle for 2 h in acetone media to obtain a homogeneous powder. The resulting ground mixtures were dried and calcined at appropriate temperatures and time durations. The calcined powders were again ground and palletized into circular discs of 20 mm diameter by applying 12 kN cm^{-2} of pressure. The as prepared pellets were given double stage heat treatment at different temperatures followed by intermediate grinding. Different sample compositions with their levels, calcination and sintering temperature are given in table 3.1.

Table 3.1: Sample compositions, calcination and sintering temperatures.

Composition	**Calcination temperature (˚C)**	**Sintering temperature (˚C)**	
		Ist stage	**IInd stage**
$Bi_{1-x}Sr_xMnO_3$ (0.40≤ x ≤0.55)	750	1050	1200
$Bi_{1-x}Ca_xMnO_3$ (0.40≤ x ≤0.55)	750	900	950
$Bi_{1-x}Sr_xFeO_3$ (0.40≤ x ≤0.55)	750	900	1050
$Bi_{1-x}Ca_xFeO_3$ (0.40≤ x ≤0.55)	750	900	950
$Bi_{1-x}Sr_xYO_3$ (0.0≤ x ≤0.20)	700	800	850
$Bi_{1-x}Ca_xYO_3$ (0.0≤ x ≤0.20)	700	800	850
$Bi_{1-x}Sr_xCrO_3$ (0.40≤ x ≤0.50)	750	850	900
$Bi_{1-x}Ca_xCrO_3$ (0.40≤ x ≤0.50)	750	850	900

3.3 Characterization techniques

The prepared samples have been characterized by using different techniques for their phase identification, thermal stability and conductivity properties. The details of the different techniques used are given below:

3.3.1 Density measurements

Density of the samples was measured by the buoyancy method based on the Archimedes principle. The apparent weight of the sample i.e. weight reduced by the buoyancy force in a reference liquid was measured by a precision balance. The value of the weight of the sample in air combined with the weight of sample in reference liquid was used to calculate the density of the sample. Xylene was used as the reference liquid for measurement. The density measurements were carried out at least five times to average out the variation in values measured. The formulae used for density measurements are as follows:

$$d = \frac{d_L m_s}{m_L} = \frac{d_L m_s}{m_s - m_{liq}} \qquad [3.1]$$

Where, m_L and m_s are the weight of the sample weighed in liquid and in air, respectively. m_{liq} is the displaced weight of the liquid. d and d_L are the density of sample and liquid, respectively.

The relative density (in %) is given by $\frac{d}{d_{th}} \times 100$; d and d_{th} are experimental and theoretical densities, respectively. The theoretical density is measured by $d_{th} = \frac{MZ}{N_a V}$, where, M is molar mass of material, N_a is Avogadro constant, Z is number of atoms per unit cell and V is volume of unit cell.

3.3.2 Tolerance factor and specific free volume

The tolerance factor $\left(t = \frac{r_a + r_0}{\sqrt{2}(r_b + r_0)}\right)$ gives rough idea about the deviation of crystal structure from most symmetric cubic structure. However, for the stoichiometric oxides having A and B cations in +3 oxidation state, the prediction of tolerance factor is easy. On the other hand, when some dopants such as aliovalent cations are substituted in the system, the tolerance factor is calculated by considering all possible components like cation/anion vacancies, oxidation state of B site cation (in case of transition elements) corresponding to their molar concentrations in formula unit. In the present studied systems, for the calculation of tolerance factor, the molar ratio of Bi and Sr/Ca at A –site was known from their formula unit and the concentration of oxygen vacancies and concentration of B^{3+}/B^{4+} was calculated experimentally from iodometric titration. The effective ionic radii of different components were calculated as follows [1]:

By considering the anionic vacancies and mixed oxidation state (B^{3+}/B^{4+}) of B –site cations, the formulae unit can be written as:

$$A_{1-a}A'_aB^{3+}_{1-a+2\delta}B^{4+}_{a-2\delta}O_{3-\delta}V_{o,\delta} \quad [3.2]$$

Where $A = Bi, A' = Sr/Ca, B = Mn, Fe\ and\ V_{o,\delta}$ is oxygen vacancies

So, $r_A = (1-a)r_A + ar'_A$; $r_B = (1-a+2\delta)r_{B^{3+}} + (a-2\delta)r_{B^{4+}}$ [3.3]

$$r_0 = \left(1-\frac{\delta}{3}\right).140 + \left(\frac{\delta}{3}\right).r_{V_o}\ ;\ r_{V_o} = 1.40.\sqrt[3]{V_f} \quad [3.4]$$

Where, r_{V_o} is the ionic radii of the vacancies and V_f is free volume which is defined as V_f= unit cell volume – occupied space. For the Y containing system, oxygen vacancies are the only possible defects, as yttrium will not change its oxidation state, so the ionic radii have been calculated accordingly.

Other than tolerance factor, specific free volume of all the oxides have also been calculated by using the relation: $V_{f,s} = \frac{\text{unit cell volume} - \text{occupied space}}{\text{unit cell volume}}$ [3.5]

3.3.3 X-ray diffraction

The X-ray diffraction is analytical non- destructive technique that uses X-rays to characterize the crystalline phases present in a sample. This technique is primarily used for phase identification of a crystalline material and can also provide information for crystallite size, lattice parameters, lattice strain and crystal orientation. In X-ray tube, a beam of electrons generated by a heated tungsten filament is accelerated towards a metal target commonly molybdenum, copper, iron, cobalt and chromium. The high energy incident electrons can eject core electrons from the metal target. When outer shell electrons fill an inner shell vacancy, an X-ray photon with the characteristic energy of the target material will be emitted. When an incident beam of X-ray strikes the surface of a crystal, the angle of the scattered beam can be used to determine the distance between layers of atoms in a sample using Bragg's law: which is $2d\ sin\theta = n\ \lambda$; where, d is lattice spacing (Å), θ is angle of incidence (degree), λ is wavelength of X-rays (Å) and n is an integer [2]. From this consideration, the positions of the reflections can be predicted for a given periodic solid and for an unknown solid sample; the periodicity can be obtained from observed reflection positions.

The relative intensities of the observed reflections, I_{hkl} are proportional to $|F_{hkl}|^2$, where, F_{hkl} is the structure factor for *(hkl)* reflections and is defined as [3]:

$$F_{hkl} = \sum_{j=1}^{n} f_j\ exp\left[2\pi i(hx_j + ky_j + lz_j)\right] \exp\left[-B_j(\sin^2\theta)/\lambda^2\right] \quad [3.6]$$

Where, F_{hkl} is the summation over all the atoms within the unit cell, f_j is the scattering factor or form factors for X-rays of atoms; j, x_i, y_j and z_j are the fractional coordinates of atom j in the unit cell. The thermal motion of the atoms is taken into account by Debye-Waller factor where, B_j is the atomic temperature factor which is related to mean square thermal displacement factor U_j by $B = 8\pi^2 U$. In this way, the observed diffraction pattern can provide information about only the symmetry and lattice parameter of a particular crystalline material, but also the atomic contents and position within the unit cell. For the present study, the X-ray powder diffraction (XRD) measurements was performed at room temperature using a PANalytical X'Pert PRO system with Cu Kα radiations (1.54 Å) and Ni filter. During the experiment the step size was 0.017°.

3.3.4 Rietveld refinement

The Rietveld method is widely used to refine crystal and magnetic structures from obtained X-ray or neutron powder diffraction patterns. In Rietveld method, the XRD patterns are decomposed by using Pawley and/or Le Bail algorithms [4].

This method performs a curve fitting procedure by considering the observed intensity y_i *(obs)* of each equally spaced steps *i* over the entire pattern including the background intensity and sum of the contribution of reflection close to *i* powder pattern step:

$$y_i(obs) = y_i(background) + \sum y_i(Bragg) \quad [3.7]$$

The Rietveld method is a refinement technique to minimize the residual between the observed intensity y_i *(obs)* and calculated intensity y_i *(calc)* by the best least square fits as:

$$S_y = \sum w_i \left[y_{i(obs)} - y_{i(calc)} \right]^2 \quad [3.8]$$

Where, w_i is statistical weight that equals $1/y_{i(obs)}$ and $y_{i(calc)}$ is the intensity of each step which can be calculated by a mathematical expression that includes the factors related to both the structure and non-diffraction terms and is expressed as:

$$y_{i(calc)} = S \sum_{hkl} L_{hkl} |F_{hkl}|^2 \emptyset(2\theta_i - 2\theta_{hkl}) P_{hkl} A + y_{i(background)} \quad [3.9]$$

Here, S is scale factor, L_{hkl} contains the Lorentz, polarization and multiplicity factors, F_{hkl} is structure factor which includes nuclear and magnetic structure factors if applicable, $\emptyset(2\theta_i - 2\theta_{hkl})$ is the peak shape function which describes the effects of the instrument and the sample on reflection profile, P_{hkl} is preferred orientation factor, *A* is absorption factor and

$y_{i(background)}$ is the background intensity at step *i* of the diffraction pattern. Therefore, a good initial structure model is required including information about space group, unit cell lattice parameters, atomic positions and instrumental details.

During the refinement cycles, each of these terms and its parameters are varied to improve the match between observed and calculated diffraction patterns i.e. to minimize S_y value. The fitting results can be estimated by examining a plot of the difference between observed and calculated reference patterns. On the other hand, several numerical terms can be used to estimate the goodness of the least square refinements. These residual values are defined as:

$$R_p = \sum \left[\frac{y_{i(obs)} - y_{i(calc)}}{y_{i(obs)}}\right]^2 \quad [3.10]$$

$$R_{wp} = \left|\frac{\sum w_i \left(y_{i(obs)} - y_{i(calc)}\right)^2}{\sum w_i \left(y_{i(obs)}\right)^2}\right|^{\frac{1}{2}} \quad [3.11]$$

$$\chi^2 = \frac{\sum w_i \left(y_{i(obs)} - y_{i(calc)}\right)^2}{n-p+c};\ \chi^2 = \left[\frac{R_{wp}}{R_{exp}}\right]^2 \quad [3.12]$$

where, n is number of observation, *P* is number of parameters and c is number of constraints in the definition of goodness of fit. A good fit with the refined structure model will accompany with a low residual value. The R_{wp} is commonly considered since it contains by which quantity to be minimized by the least square refinements. The goodness of fit χ^2 which is directly proportional to S_y is also regarded as key parameter and is ideally to be unity.

For the present work, the X-ray diffraction patterns were fitted by Pseudo-voigt method using the following equation [3]:

$$\Omega(x) = pV(x) = \eta L(x) + (1-\eta)G(x) \quad [3.13]$$

Where *pV(x)* function is a linear combination of a Lorentzian (*L*) and a Gaussian (*G*) of the same full width at half maximum (FWHM) of XRD peaks. η varies from 0 to 1. A full profile analysis included a refinement of background, scaling factor, lattice parameters, Bragg peak profile, position and thermal parameters which have been performed for all samples.

3.3.5 X-ray photoelectron spectroscopy

X-ray photoelectron spectroscopy (XPS) is the most widely used surface sensitive quantitative technique that measures the chemical composition at the parts per thousand

range, empirical formula, chemical state and electronic state of the elements that exist within the material. X-ray photoelectron spectra are obtained by irradiating a material with a beam of X-rays and measuring the energy of photoelectrons to be emitted from the sample surface. An electron energy analyzer determine the binding energy of photoelectrons. Momentum and energy of photoelectrons give direct information on the electronic structure of matter from which they were excited. With XPS, it is possible to measure the shell structure of atoms and electronic band structure of solid in a direct manner [5].

The X-ray photoelectron spectroscopy (XPS) analyses were carried out with the CLAM2 electron spectrometer using Mg Kα X-ray source (20 mA, 10 kV). The instrument work function was calibrated to give an Au $4f_{7/2}$ metallic gold binding energy of 84 eV. The spectrometer dispersion was adjusted to give a binding energy of 932.6 eV for metallic Cu $2p_{3/2}$. Instrument base pressure was 1×10^{-9}Torr density measurements.

3.3.6 Iodometric titration

The average oxidation state of transition metals (M) and oxygen content in the studied samples was determined by iodometric titration. Around 20-30 mg of sample was dissolved in 10 ml of HCl and 10 ml of 10% KI solution in argon atmosphere. The following reaction occurs during the whole experiment.

$$2M^{3+} + 2Cl^{-} \rightarrow Cl_2 + 2M^{2+}$$

$$M^{4+} + 2Cl^{-} \rightarrow Cl_2 + M^{3+}$$

$$Cl_2 + I^{-} \rightarrow 2Cl^{-} + I_2 \qquad [3.14]$$

The iodine formed by above reaction is titrated against 0.01molar sodium thiosulphate solution by using starch as an indicator. If α is the fraction of M^{3+} in the studied system, then $\alpha = 2 - \frac{V.C.M}{m}$, where, *V* is volume of thiosulphate solution used in titration, *m* is weight of the sample, *M* is molecular weight of the sample and *C* is concentration of sodium thiosulphate solution. The number of oxygen vacancies is calculated by using the relation [6]:

$$3 \pm \delta = [oxidation\ state\ of\ A\ site\ cation + 3\alpha + (1-\alpha)4]/2 \qquad [3.15]$$

3.3.7 Fourier transform infrared spectroscopy (FT-IR)

FT-IR spectroscopy is a rapid and relative inexpensive technique for the analysis of solids that are infrared active. Infrared spectroscopy is the study of interaction between the matter

and electromagnetic (em) fields in the IR region. In this spectral region, the em waves mainly couple with the molecular vibrations. In other words, a molecule can be excited to higher vibrational state by absorbing IR radiation. The probability of a particular IR frequency being absorbed depends upon the actual interaction between this frequency and the molecule. In general a frequency will be strongly absorbed if its photon energy coincides with the vibrational energy levels of the molecule. IR spectroscopy is therefore, a very powerful technique which provides fingerprint information on the chemical composition of the sample. A typical IR spectrum consists of the following information: (1) the fundamental bands of relatively heavy metal ions, torsional modes and other low frequency excitations in the far IR region. (2) Strong fundamental vibrations of aluminosilicates framework of minerals and glasses in mid IR region. (3) Moderately intense overtones and combination bands due to even lighter group e.g. H_2O, OH- etc. in the near IR region [7]. To study the changes in bond lengths, FTIR spectra were obtained at room temperature by using Perkin Elmer model RZX spectrometer in the region 400-1200 cm^{-1}. 2 mg of each sample was ground with 100 mg of KBr into fine powder and after that pressed into pellets for IR study. The spectrum of each sample was normalized to the spectrum of blank KBr.

3.3.8 Raman spectroscopy

Raman spectroscopy is a spectroscopic technique based on inelastic scattering of monochromatic light usually from a laser source. Inelastic scattering means that the frequency of photons in monochromatic light changes upon interaction with a sample. Photons of the laser light are absorbed and reemitted by the sample. Frequency of the reemitted photons is shifted up or down in comparison with the original monochromatic frequency which is called Raman effect. This shift provides information about the vibrational, rotational and other low frequency transition in molecule. The Raman effect is based on the molecular deformation in electric field *E* determined by molecular polarizability. The laser beam can be considered as an oscillating em wave. Upon interaction with the sample, it induces electric dipole moment which deforms the molecule. Because of periodical deformation, molecules start vibrating with characteristic frequency. Amplitude of vibration is called a nuclear displacement. In other words, monochromatic laser light excites molecules and transforms them into oscillating dipoles such oscillating diploes emit light of three types: Rayleigh scattered light, stokes and antistokes [8]. To study the changes in local structures, the present samples were studied by Raman spectroscopy. Raman spectra of the powder samples were collected using a Renishaw in Via Raman spectrometer with the 514.5 nm line

of an Ar^+ laser at 20 mW power. The instrument was calibrated using silicon as a reference at 520 cm^{-1} within ±1 cm^{-1}.

3.3.9 Scanning electron microscopy

Scanning electron microscope is an electron microscope that produces images of a sample by scanning it with a focused beam of electrons. It has the magnification up to 10^6 times with higher depth of field which allows larger area of sample to focus at one time. The electron beam is generated by a tungsten filament or lanthanum hexaborate on which voltage is applied. The electron so generated from heated filament beam is accelerated towards the sample surface by focusing it through several electromagnetic lenses. Finally, a fine beam of electrons is allowed to fall on the sample surface. When the electron beam interacts with the specimen, its energy is converted into alternative forms and leads to emission of secondary electrons, back scattered electrons and X-ray emission. These signals carry the information about the topography and morphology of the specimen. Different detectors are used to detect these emitted signals from the samples and convert them to electrical signals for manipulations. Secondary electrons and backscattered electrons are commonly used for imaging samples. Secondary electrons are most valuable for studying the morphology and topography of the samples and backscattered electrons are most valuable for illustrating contrast in composition in multiphase samples [9]. The microstructural study was carried out on gold sputtered fractured surfaces of pellets by scanning electron microscope (JSM-6510LV, JEOL) for all the samples.

3.3.10 X-ray dot mapping

X-ray dot mapping is a quantitative and qualitative chemical microanalysis technique performed in conjunction with a scanning electron microscope. Its characterization capabilities rely on the fact that each element has a unique atomic structure allowing unique sets of peaks on its X-ray spectrum. To simulate the emission of characteristic X-rays from a specimen, a high energy beam of electrons is focused on the sample under investigation. The incident beam excite the electrons from the inner shell and after that electrons from the outer shell fills the hole and the difference in energy between high energy shell and the lower energy shell is released in the form of characteristic X-rays. The number and energy of X-rays emitted from the specimen are measured as a function of their position in this technique. As the energy of X-rays is characteristic of the difference in energy between the two shells and the atomic structure of the elements from which they are emitted, so, their concentration

is easily detected. This allows the chemical composition of the specimen to be measured [9]. X-ray intensities are measured by counting the photon and the precision obtainable is limited by statistical error. For major elements, it is usually not difficult to obtain a precision of better than ±1% but the overall analytical accuracy is commonly nearer ±2%. Some correction factors such as uncertainties in composition of the standards and errors in the various corrections are also applied to raw data to increase the accuracy of results. In the present work the X-ray dot mapping analysis was carried out using an INCA attachment with the SEM instrument.

3.3.11 Thermal Analysis

3.3.11.1 Thermogravimetric analysis (TGA)/ differential thermal analysis (DTA)

Thermogravimetric analysis (TGA) is an analytical technique used to determine the thermal stability of materials and its fraction of volatile components by monitoring the weight change that occurs when a specimen is heated in a controlled furnace. TGA consists of a sample pan that is supported by a precision balance. Pan resides in a furnace and is cooled/heated during the experiment. A sample purge gas controls the sample environment. This gas may be inert or reactive gas that flows over the sample and exits through an exhaust.

A DTA consists of a heating chamber which holds two sample pans/crucibles. One crucible contains the sample and other contains a reference material which does not undergo any physical/chemical change during analysis. When any change occurs in the sample; it either evolves or absorbs energy. The DTA measures the difference in energy supplied to the sample crucible and reference crucible to maintain the zero heat difference between the two.

The TGA/DTA of sintered samples were performed with Diamond Pyris TG/DTA (Perkin Elmer) in air atmosphere at 5 °C/min heating rate from 50 °C to 900 °C for both heating and cooling cycles by taking Al_2O_3 powders as reference material. The flow of air during the experiment was 5 kg cm^{-2}. The temperature and weight change detection limit of the instrument are ± 1ºC and 0.001 mg, respectively.

3.3.11.2 Dilatometry

Thermal expansion is the tendency of the materials to change their volume in response to the change in temperature. The degree of expansion divided by change in temperature is called thermal expansion coefficient of the material. The lattice of array can be considered as an assembly of harmonic oscillators. The force acting on the vibrating atoms is directly

proportional to the atomic displacements. As the temperature increases the average amplitude of the vibration also increases, resulting in the thermal expansion. The expansion process is a direct consequence of asymmetry of potential energy curve. The thermal expansion coefficient (TEC) is an important parameter for any material to be used in SOFC. As thermal expansion mismatch can cause thermal stresses in the materials and degrade the overall performance. The thermal expansion coefficient of all the samples was determined by using pushrod Netzsch DIL 402 PC dilatometer in the temperature range 30 - 900 ºC at a heating rate of 5 °C/min in air at atmospheric pressure. The polished rectangular bars of dimensions 1.5-2mm were used for the measurements. The resolution limit of the instrument is 9 nm.

3.3.12 Electrical conductivity

Impedance spectroscopy is probably the most important tool for investigating the electrical transport and electrochemical properties of ionic solids. In a typical impedance spectroscopy measurement, a small alternating electrical signal is applied to the sample and the response (the resulting impedance) is measured. By varying frequency *'w'*, over several decades of magnitude, one can in many cases distinguish individual resistive processes due to difference in their relaxation time. Every electrochemical process is characterized by a specific relaxation frequency. These relaxation frequencies are sufficiently different that impedance spectroscopy can measure them separately.

To display experimental impedance data, different kinds of plots based on impedance, admittance, modulus and complex capacitance are used. In solid state ionics most commonly cole –cole plots (imaginary vs real part of Z) are used. These spectra are interpreted with the help of equivalent circuits consisting of resistance (R), Capacitor (C) and other elements depending upon the shape of the plot. The simplest case is a single RC element i.e. one resistor and capacitor in parallel. The impedance in this case is given by: $= \frac{R}{1+iwRC}$. In the complex impedance plane, such impedance yields a semicircle with diameter R. It is clear that in the limit $w \rightarrow 0$ the influence of the capacitance has to vanish and the resistance R is obtained. Two series RC elements leads to two well separated semicircles in the complex impedance if their relaxation frequencies are sufficiently different. Hence, if measurement yields one or several well separated semicircles, the resistances and relaxation frequencies of the underlying processes can immediately be read from the cole-cole plot and thus a capacitance can be calculated for each process. The magnitude of a capacitance is a strong indication of its physical origin. Typical orders of magnitude of some capacitances in solid

state electrochemistry are given in table 3.1 [10]. The electrical conductivity measurements were performed on impedance analyzer (Solatron: S1260) in the frequency range of 0.1 Hz-32 MHz and in temperature range of 300-800 ºC. For conductivity measurements, circular discs of diameter 15 mm and thickness 1.5 mm approximately were used and gold sputtered to get good electrical contacts between platinum electrodes and sample surface. The obtained impedance data was fitted with Z-view software to get the capacitance and resistance values at different temepartures.

Table 3.2: Different capacitance values corresponding to different physical processes.

Corresponding physical process	**Typical value per area (F cm^{-2})**
Dielectric relaxation in bulk (C_{bulk})	10^{-12}
Grain boundary polarization in a polycrystalline material (C_{gb})	10^{-8}
Electrical double layer polarization at solid/solid interface (C_{dl})	10^{-5}
Oxygen stoichiometry in the bulk of a mixed conducting thin film electrode (C_{chem})	10^{-2}

3.4 Interaction study

The selected samples were studied for their chemical interaction with YSZ. The as procured YSZ powders were heat treated at 1200 ˚C before use. For interaction study, the slurry of oxides in ethanol media were deposited over the YSZ pellets. After that the as prepared samples were heat treated for 5 h, 50 h and 100 h in a tubular furnace. After heat treatments these samples were characterized by different techniques like XRD, scanning electron microscope and X-ray dot mapping to study the phases formed after heat treatments.

References

[1] H. Ullmann, N. Trofimenko J. Alloys Compd. 316 (2001) 153.

[2] B. D. Cullity, Elements of X Ray Diffraction Edt. 1 (2001) Prentice Hall New Jersey.

[3] Brian H. Toby, Powder Diffraction 21 (2006) 68.

[4] F. S. Nchez-Bajo and F. L. Cumbrera, J. Appl. Cryst. 30 (1997) 427.

[5] John F. Watts, John Wolstenholme, An Introduction to Surface Analysis by XPS and AES (2003) John Wiley & Sons Inc. Hoboken New Jersey.

[6] C. Vazquez, M. C. Blanco, M. A. Lopez-Quintela, R. D. Sanchez, J. Rivas, S. B. Oseroff, J. Mater. Chem. 8 (1998) 991.

[7] B. C. Smith, Fundamentals of Fourier Transform Infrared Spectroscopy Edt. 2 (2003) CRC Press USA.

[8] J. R. Ferraro, Introductory Raman Spectroscopy (2003) Academic Press New Jersey.

[9] B. L. Gabriel, SEM: A user's manual for Materials Science Amer. Soc. Metals (1985) Metals Park Ohio USA.

[10] E. Barsoukov J. R. Macdonald, Impedance Spectroscopy: Theory, Experiment, and Applications Edt. 2 (2005) John Wiley & Sons New Jersey.

Chapter 4

RESULTS AND DISCUSSION-I

Overview

This chapter presents the experimental results of different series studied in this work. The Sr^{2+} and Ca^{2+} substituted $BiMnO_3$, $BiFeO_3$, $BiYO_3$ and $BiCrO_3$ systems have been synthesized and studied for their physical, structural, thermal and electrical properties. The different experimental techniques viz. XRD, XPS, iodometric titration, FT-IR, Raman, TGA/DTA, SEM and impedance spectroscopy has been employed to study their properties. The effect of different substituents Sr^{2+}/Ca^{2+} on A-site and different B-site cations which influences the properties have been studied. The results are discussed in the light of change in oxidation state of B-site cation, oxygen vacancies and ordering/disordering in the systems.

On the basis of literature survey, the proposed plan of work has been presented in the previous chapter. It has been observed that mixed ionic–electronic conductors can fulfill most of the requirements of cathode materials for IT-SOFC applications. To meet these requirements, samples of $Bi_{1-x}A_xMO_3$ (M=Mn, Fe, Cr; A=Sr, Ca; $0.40 \leq x \leq 0.55$, M=Y; $0.0 \leq x \leq 0.20$) have been synthesized and characterized for structural, thermal and conductivity properties. In this chapter these properties are presented and discussed in the light of disordering, phase transition, change in oxidation state of B-site cations and oxygen vacancies formation due to different physical and chemical properties of different substituents and B-site cations.

4.1 $Bi_{1-x}A_xMnO_3$ (A=Sr, Ca; $0.40 \leq x \leq 0.55$)

It is expected that highly polarizable lone electron pairs of bismuth along with the ability of Mn to change its oxidation state can modify some of the properties. Moreover, it is well reported in literature that the best properties of these systems are observed around x=0.50 [1, 2]. So, it will be interesting to study the effect of two different cations substitution; one (Sr^{2+}) having the higher ionic radii (1.26 Å) and other (Ca^{2+}) lower (1.12 Å) than parent cation Bi^{3+} (1.17 Å) on structural, thermal and electrical properties of these systems.

4.1.1 Physical properties

Density of all the samples was measured by Archimedes Principle (details of measurement has already been described in experimental section). All the samples have density more than 95% of their theoretical density as given in table 4.1 which indicates that all the samples are well sintered with very low porosity.

Specific free volume and tolerance factor of all the samples along with their labels and compositions have also been calculated and summarized in table 4.1. Specific free volume and tolerance factor of BSM system is higher than BCM system. This may be due to the higher unit cell volume of BSM as compared to BCM and larger ionic radii of Sr^{2+} (1.26 Å) as compared to Ca^{2+} (1.12 Å) [3]. Consequently, the specific free volume of BSM leads to higher oxide ion conductivity than BCM system. The high tolerance factor of BSM than that of BCM is also well supported by XRD data (discussed in next section). BSM is more symmetric structurally having tetragonal structure as compared to BCM having orthorhombic structure.

Table 4.1: Composition along with sample label, density, tolerance factor and specific free volume of $Bi_{1-x}A_xMnO_3$ (A=Sr, Ca; 0.40≤x≤0.55).

Composition	Sample Label	Density			Tolerance factor	Specific free volume
		Theoretical density (d_{th}) (g cm^{-3})	Experimental density (d) (g cm^{-3})	(d/d_{th}) (%)		
$Bi_{0.60}Sr_{0.40}MnO_3$	BSM-40	7.48	7.27	97.2	0.860	0.262
$Bi_{0.55}Sr_{0.45}MnO_3$	BSM-45	7.37	7.14	96.9	0.862	0.253
$Bi_{0.50}Sr_{0.50}MnO_3$	BSM-50	7.23	7.02	97.1	0.866	0.245
$Bi_{0.45}Sr_{0.55}MnO_3$	BSM-55	7.07	6.83	96.7	0.889	0.252
$Bi_{0.60}Ca_{0.40}MnO_3$	BCM-40	7.24	6.95	96.0	0.843	0.244
$Bi_{0.55}Ca_{0.45}MnO_3$	BCM-45	7.03	6.76	96.2	0.843	0.248
$Bi_{0.50}Ca_{0.50}MnO_3$	BCM-50	6.78	6.53	96.4	0.845	0.258
$Bi_{0.45}Ca_{0.55}MnO_3$	BCM-55	6.58	6.36	96.8	0.839	0.246

4.1.2 X-ray diffraction

The Rietveld refined XRD patterns of $Bi_{1-x}Sr_xMnO_3$ (0.40≤x≤0.55) are shown in figure 4.1. A full profile analysis including a refinement of background, scaling factor, lattice parameters, Bragg peak profile, positions and thermal parameters have been performed for all samples. The overall good agreement between the calculated and observed patterns was observed for

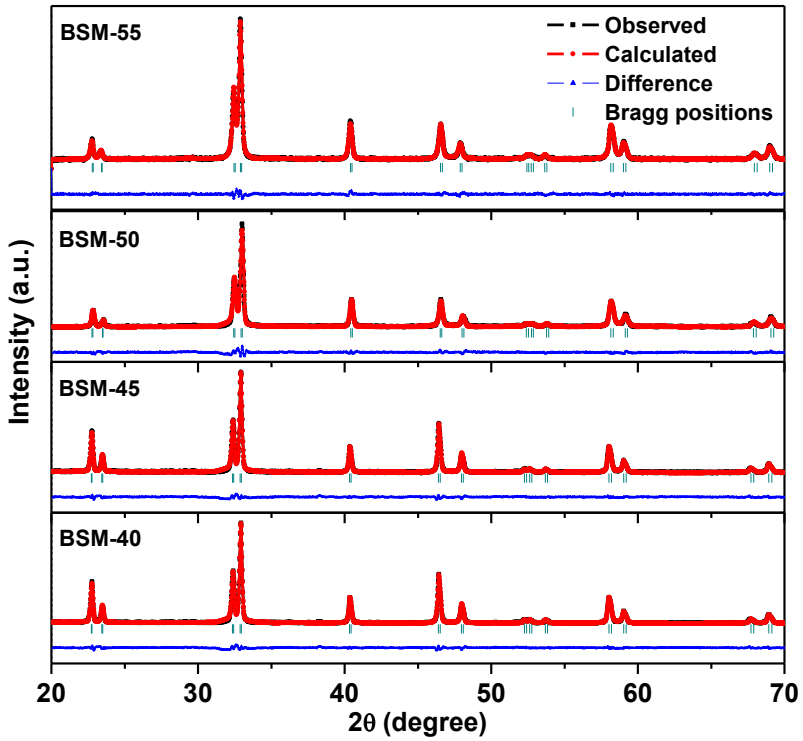

Figure 4.1: Rietveld refined X-ray diffraction pattern of $Bi_{1-x}Sr_xMnO_3$ (0.40≤x≤0.55).

BSM system as shown in figure 4.1. All the goodness of fit parameters and crystallographic data obtained after the refinement are summarized in table 4.2. All the BSM samples are

single phase and exhibit tetragonal structure with *p4mm* symmetry. The lattice parameters and unit cell volume show a decreasing trend with increasing concentration of Sr^{2+}. Whereas, unit cell volume should increase because Sr^{2+} (1.26 Å) has larger ionic radii as compared to Bi^{3+} (1.17 Å). But surprisingly, it shows opposite trend. This anomaly can be related to the charge imbalance created in the system due to the substitution of Sr^{2+} in place of Bi^{3+}. Change imbalance will be maintained in the system by two ways: (a) Mn^{3+} ions will get converted into Mn^{4+} and (b) oxygen vacancies will be created. Ionic radii of Mn^{4+} (0.67 Å) are smaller than that of Mn^{3+} (0.78 Å) which will reduce the unit cell volume. So, it may be possible that in BSM system, the smaller ionic radii of Mn^{4+} influences the system more strongly as compared to larger ionic radii of Sr^{2+} ion. In addition to this, according to Pauling's rule, Mn^{4+} ions strengthen the Mn-O bonds in MnO_6 octahedral, which also reduces the unit cell volume [4].

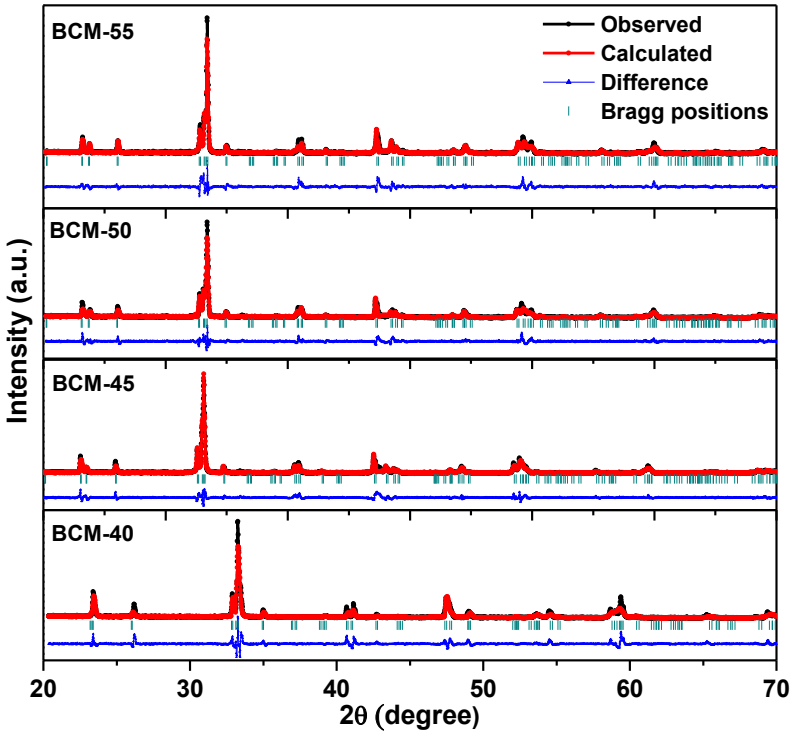

Figure 4.2: Rietveld refined X-ray diffraction pattern of $Bi_{1-x}Ca_xMnO_3$ ($0.40 \leq x \leq 0.55$).

The Rietveld refined X-ray diffraction patterns of $Bi_{1-x}Ca_xMnO_3$ ($0.40 \leq x \leq 0.55$) are shown in figure 4.2. All the samples of BCM exhibit orthorhombic structure with *pbnm* symmetry. The crystallographic and refinement parameters for all the samples are also given in table 4.2. In BCM system, each cell of dimensions $a \times b \times c$ is built up of four small distorted perovskite unit cells. In ideal situation the small unit cell is cubic with a lattice parameter a_p then $a=b=$

$\sqrt{2}a_p$ and $c=2a_p$ which implies that $a = b = \frac{c}{\sqrt{2}}$ [5]. The pseudo cubic lattice constant a' which represents the lattice parameter of a cubic unit cell containing one ABO_3 unit cell can be defined as $a' = (\frac{V}{Z})^{\frac{1}{3}}$ where, V is unit cell volume, Z is number of ABO_3 units in one unit cell [5-6]. The values of a' are tabulated in table 4.2. The decrease of a' with increase of Ca^{2+} concentration is related to smaller ionic radii of Ca^{2+} than Bi^{3+}. Moreover, generation of Mn^{4+} and oxygen vacancies will also contribute to reduce the unit cell parameters.

To understand the difference between the crystal structure of Ca^{2+}/Sr^{2+} substituted $BiMnO_3$, it is essential to discuss the structure of undoped $BiMnO_3$. Undoped $BiMnO_3$ exhibits monoclinic structure [6]. The presence of highly polarizable $6s^2$ lone electron pair in $BiMnO_3$ is responsible for the displacement of Bi^{3+} from its centrosymmetric position and formation of monoclinic structure. When alkali earth cations such as Sr^{2+} and Ca^{2+} are substituted in place of Bi^{3+}, this polar displacement can be suppressed due to lattice distortion or formation of oxygen vacancies [7]. This results in formation of a more symmetric environment around Bi^{3+} and leads to more symmetric structure as observed in present systems. The John-Teller ordering due to the generation of Mn^{4+} can also be responsible for the more symmetric structure [8]. However, these changes in local environment depend on chemical nature of solutes. Since the size of Ca^{2+} (1.12 Å) is almost same as that of Bi^{3+} (1.17 Å), so in case of BCM system, there is less distortion in the structure and Bi^{3+} remains displaced from its centrosymmetric position and exhibit orthorhombic structure. Whereas, size of Sr^{2+} (1.26 Å) is greater than Bi^{3+} (1.17 Å) which creates more lattice distortion and have higher space to accommodate oxygen vacancies as compared to BCM. Consequently, lone pairs are directed in such a way to create more symmetric structure (tetragonal) as compared to orthorhombic structure of BCM. This fact is also well supported by tolerance factor as discussed in section 4.1.1. High values of tolerance factor in case of BSM indicate that this system is more symmetric as compared to BCM. Symmetric structures have usually positive influence on the overall conductivity. So, it can be expected that BSM system will exhibit high conductivity than BCM system.

Table 4.2: Lattice parameters and refined parameters of $Bi_{1-x}A_xMnO_3$ (A=Sr, Ca; $0.40 \leq x \leq 0.55$).

Sample Label	Lattice parameter (Å)	a´ (Å)	Wyckoff positions	Goodness of fit paraemters		Grain size (μm)
				R_{wp} (%)	χ^2	
BSM-40	a =3.91507(6) c =3.81583(9)	-	Bi/Sr: (0,0,0) Mn: (0.5,0.5, 0.5443(6)) O1: (0.5, 0.5, 0.1547(7)) O2: (0.5, 0, 0.5835(1))	1.98	1.67	3.44
BSM-45	a = 3.91070(4) c = 3.79083(1)	-	Bi/Sr: (0,0,0) Mn: (0.5,0.5, 0.4550(9)) O1: (0.5, 0.5, 0.1043(5)) O2: (0.5, 0, 0.5437(1))	2.68	1.52	2.61
BSM-50	a = 3.90175(4) c = 3.78681(5)	-	Bi/Sr: (0,0,0) Mn: (0.5,0.5, 0.5037(8)) O1: (0.5, 0.5, 0.1670(5)) O2: (0.5, 0, 0.6018(2))	2.01	1.98	1.97
BSM-55	a = 3.89522(5) c = 3.79284(7)	-	Bi/Sr: (0,0,0) Mn: (0.5,0.5, 0.4993(2)) O1: (0.5, 0.5, 0.0442(4)) O2: (0.5, 0, 0.6075(3))	3.23	1.32	1.44
BCM-40	a = 5.39101(2) b = 5.45321(3) c = 7.61720(3)	3.82967	Bi/Ca: (0.0024(3), 0.0430(1), 0.25) Mn: (0.5, 0, 0) O1: (0.6059(8), 0.1251(1), 0.2941(7)) O2: (0.0446(8), 0.5695(1), 0.25)	3.17	1.98	2.75
BCM-45	a = 5.42321(5) b = 5.48652(5) c = 7.56511(8)	3.82682	Bi/Ca: (0.0056(2), 0.0378(6), 0.25) Mn: (0.5, 0, 0) O1: (0.4677(6), 0.2974(8), 0.6108(7)) O2: (0.0676(2), 0.4578(7), 0.25)	4.17	2.01	2.65
BCM-50	a = 5.40877(3) b = 5.47156(3) c = 7.50960(2)	3.81945	Bi/Ca: (0.0059(5), 0.0374(5), 0.25) Mn: (0.5, 0, 0) O1: (0.66385(4), 0.0991(4), 0.4071(2)) O2: (0.0517(2), 0.5309(7), 0.25)	4.98	2.35	2.29
BCM-55	a = 5.39991(7) b =5.46241(7) c =7.50001(1)	3.80946	Bi/Ca: (0.0062(9), 0.0405(3), 0.25) Mn: (0.5, 0, 0) O1: (0.4567(3), 0.2599(7), 0.8098(1)) O2: (0.0294(5), 0.4190(1), 0.25)	2.67	2.67	2.24

4.1.3 X-ray photoelectron spectroscopy

As discussed in XRD section, Mn^{3+} will get converted into Mn^{4+} to compensate the charge imbalance created by the Sr^{2+}/ Ca^{2+} substitution. To confirm the oxidation state of Mn, X-ray photoelectron spectroscopy (XPS) was performed. Typical XPS spectra of BSM-50 and BCM-50 are shown in figure 4.3. Mn 2p spectra of both samples consist of three main peaks around 641, 653 and 647 eV for spin orbit doublet $2p_{3/2}$, $2p_{1/2}$ and a satellite structure, respectively. The interpretation of $2p_{3/2}$ spectra of Mn is quite complicated because

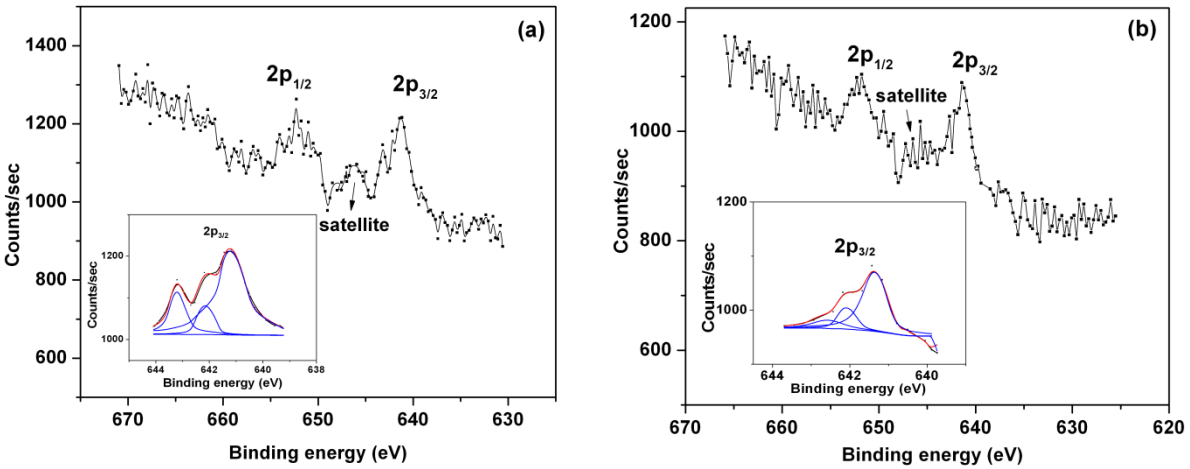

Figure 4.3: XPS spectra of (a) $Bi_{0.50}Sr_{0.50}MnO_3$ (b) $Bi_{0.50}Ca_{0.50}MnO_3$.

each single oxidation state of Mn has four or five multiple emission lines separated by an energy gap of 0.7-1.2 eV [9]. So, the spectra are deconvoluted using Lorentzian-Gaussian sum function after Shirley background subtraction (other details are given in experimental section). Deconvoluted spectra of $2p_{3/2}$ peak are shown in inset of figure 4.3 (a) and (b). The deconvoluted $2p_{3/2}$ spectrum of BSM-50 comprises of three main peaks at 643.17, 642.18 and 641.2 eV. The peak at 641.2 eV corresponds to Mn^{3+} state and other two remaining peaks can be attributed to the Mn^{4+} state. The spectra of BCM-50 also consist of three main peaks at 642.16, 642.6 and 641.4 eV but at different positions than BSM-50 sample. In BCM-50 sample, the peak at 641.4 eV can be credited to the Mn^{3+}. Whereas the peaks at 642.16 and 642.6 eV are arised due to the Mn^{4+} state of Mn [10]. The existence of satellite peak in both the samples also confirms the presence of Mn in mixed state (Mn^{3+} / Mn^{4+}). It is well reported that if satellite peak is present between the $2p_{1/2}$ and $2p_{3/2}$ in Mn spectra, the Mn is present in more than one state [11]. From the above discussion of XPS, it is clear that Mn is present in mixed state in present sample. The

existence of Mn in both the states will help to enhance the overall conductivity of the present studied systems.

4.1.4 Iodometric titration analysis

As described in the previous section, XPS confirms the existence of Mn in mixed oxidation state. So, to calculate the concentration of Mn^{3+}/Mn^{4+} and oxygen content, iodometric titration was performed for the present studied samples. The complete details of titration are given in experimental section. The results of titration are tabulated in table 4.3. The iodometric results also supports the XPS results and confirms the presence of Mn in Mn^{3+} and Mn^{4+} state. With the increase in concentration of substituent cations (Sr^{2+}/Ca^{2+}), the concentration of Mn^{4+} and oxygen vacancies also increases to maintain the charge neutrality in the system. From the iodometric data, it is also clear that in these systems, charge imbalance is mainly compensated by the oxidation of Mn^{3+} into Mn^{4+} state than creation of oxygen vacancies. These results also indicate that these materials will predominantly be electronic conductor at low temperatures.

Table 4.3: Oxygen and Mn^{4+} content as calculated from iodometric titration.

Composition	**x=0.40**		**x = 0.45**		**x=0.50**		**x=0.55**	
	Oxygen content (3- δ)	**Mn^{4+} content [(1-α) %]**	**Oxygen content (3- δ)**	**Mn^{4+} content [(1-α) %]**	**Oxygen content (3- δ)**	**Mn^{4+} content [(1-α) %]**	**Oxygen content (3- δ)**	**Mn^{4+} content [(1-α) %]**
$Bi_{1-x}Sr_xMnO_3$	2.98	37	2.97	40	2.96	45	2.92	39
$Bi_{1-x}Ca_xMnO_3$	2.99	38	2.98	41	2.97	43	2.94	40

4.1.5 Analysis of Raman spectra

Raman spectra of $Bi_{1-x}A_xMnO_3$ (A=Sr, Ca; x=0.40, 0.50) are given in figure 4.4. The spectra are deconvoluted into individual Lorentzian components and the peak position of each Raman mode was calculated. All the peak positions of Raman mode are given in table 4.4. In BSM system three peaks at 470-478, 302-359 and 640-654 have been observed. Whereas, in BCM system, these peaks are observed in the range of 475-481, 255-270 and 637-654 cm^{-1}. According to literature, undoped $BiMnO_3$ is expected to have 27 Raman active phonon modes for c2/c space group and 60 modes for c2/m symmetry [12, 13]. However, in Sr^{2+}/Ca^{2+}

substituted $BiMnO_3$, these modes become totally different due to occurrence of charge ordering. Major peaks in Raman spectra of BSM/BCM are analyzed using checkboard model, Zener polaron ordering and double strips model. In case of double strip model, if band around 630 cm^{-1} is missing then this model cannot be considered [14]. Conventional and Zener polaron model mostly differ in the sites of O (O_{pl}) in the Mn-O_2 plane. In conventional model, all O_{pl} have the same site symmetry but in Zener polaron model, there are two different sites for O_{pl} in terms of site symmetry. Conventional checkboard ordering model have $4A_g+4B_{1g}$ Raman active modes whereas in Zener polaron model, $2A_g+2B_{1g}$ active modes are possible [15-17].The peak positions corresponding to each model are given in table 4.4. If the present observed spectra is compared with both the models, it can be concluded that Zener polaron model is more appropriate for the present systems as it only contains peak around 200-300 cm^{-1}, while it is missing in another model. Among all the three models discussed above, in Zener polaron model Mn^{3+} and Mn^{4+} are most uniformly distributed in the lattice.

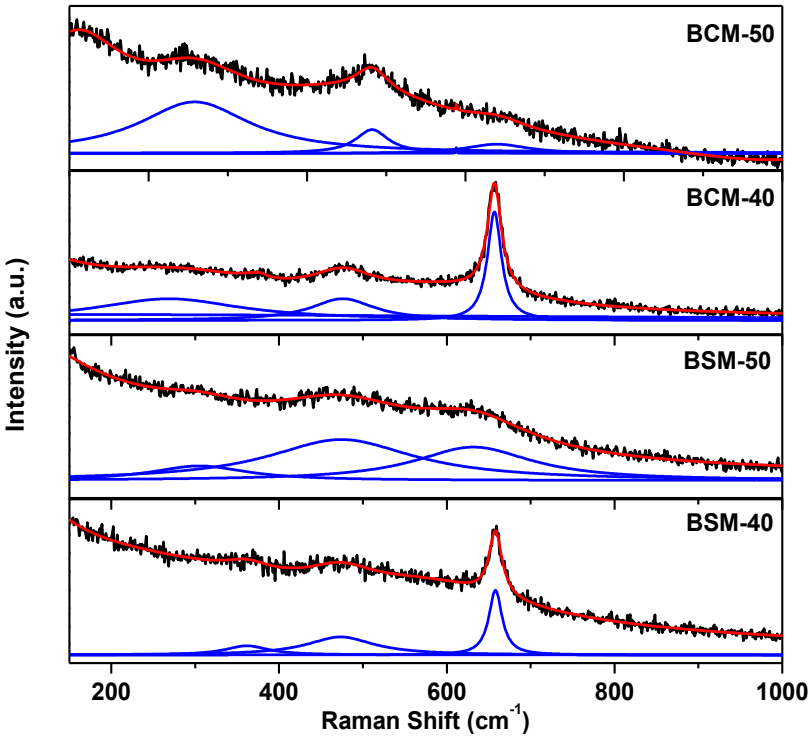

Figure 4.4: Raman spectra of $Bi_{1-x}A_xMnO_3$ (A=Sr, Ca; x=0.40, 0.50).

The changes in Raman spectra as compared to undoped $BiMnO_3$ can be explained on the basis of fact that (1) substitution at Bi^{3+} site disturbs the stereochemical activity of lone electron pair and change the Bi-O covalent bonds. (2) The different atomic weights of Sr^{2+}

(87.62 g) / Ca^{2+} (40.04 g) and Bi^{3+} (208.98 g) also affect the modes as the mode frequency is proportional to $(k/M)^{1/2}$, k is force constant and M is reduced mass. (3) Sr^{2+} /Ca^{2+} also creates defects which change the local environment around the cations and anions results in spectra modification [18-20]. The effect is more prominent in BSM with the substituent concentration as compared to BCM. This variation can be due to larger ionic radii and mass of Sr^{2+} as compared to Ca^{2+}. The Raman study also supports our earlier observations of XRD that Sr^{2+} has modified the crystal structure more strongly as compared to Ca^{2+} substitution.

Table 4.4: Comparison of Raman peak positions for the studied samples $Bi_{1-x}A_xMnO_3$ (A=Sr, Ca; x=0.40, 0.50) and reported data [14].

Raman modes (cm^{-1})	**Conventional model**	**Zener polaron model**	**BSM-40**	**BSM-50**	**BCM-40**	**BCM-50**
Ag(1)	630	480	470	478	475	481
Ag(2)	480	200-300	359	302	270	255
Ag(3)	630	-	-	-	-	-
Ag(4)	480	-	-	-	-	-
B1g(1)	635	635	654	640	654	637
B1g(2)	470	470	-	-	-	-
B1g(3)	635	-	-	-	-	-
B1g(4)	470	-	-	-	-	-

4.1.6 Fourier transform infrared analysis

To study the effect of substitution of different cations on the bond lengths and bond vibrations, FT-IR spectra of all the samples were recorded. The FT-IR spectra of BSM samples are shown in figure 4.5 (a). Four main bands around 400-420, 460, 550-580 and 1020 cm^{-1} have been observed in all the samples. The bands around 400 and 460 cm^{-1} can be attributed to the stretching vibrations of Bi-O bond in BiO_6 octahedral units [21, 22]. The another band around 580 and 1020 cm^{-1} is due to the vibrations of tetrahedrally connected Mn-O ions [23]. With the increase in substituent concentration, the band shifts towards the higher wavenumber side. This shift can be explained on the basis of low atomic weights of Sr^{2+} as compared to Bi^{3+} as vibrational frequency is inversely proportional to atomic masses of the elements. The FT-IR spectra of BCM samples are shown in figure 4.5(b). The bands are almost in the same range as observed in BSM samples. Even in this case, the bands also shift to higher wavenumber side with substituent concentration but the shift is small as compared to Sr^{2+} substituted system. This variation can be simply attributed to the different

sizes and atomic weights of both the substituent cation. Thus FT-IR spectra also reflect that Sr^{2+} substitution has affected crystal structure more strongly as compared to Ca^{2+} substitution.

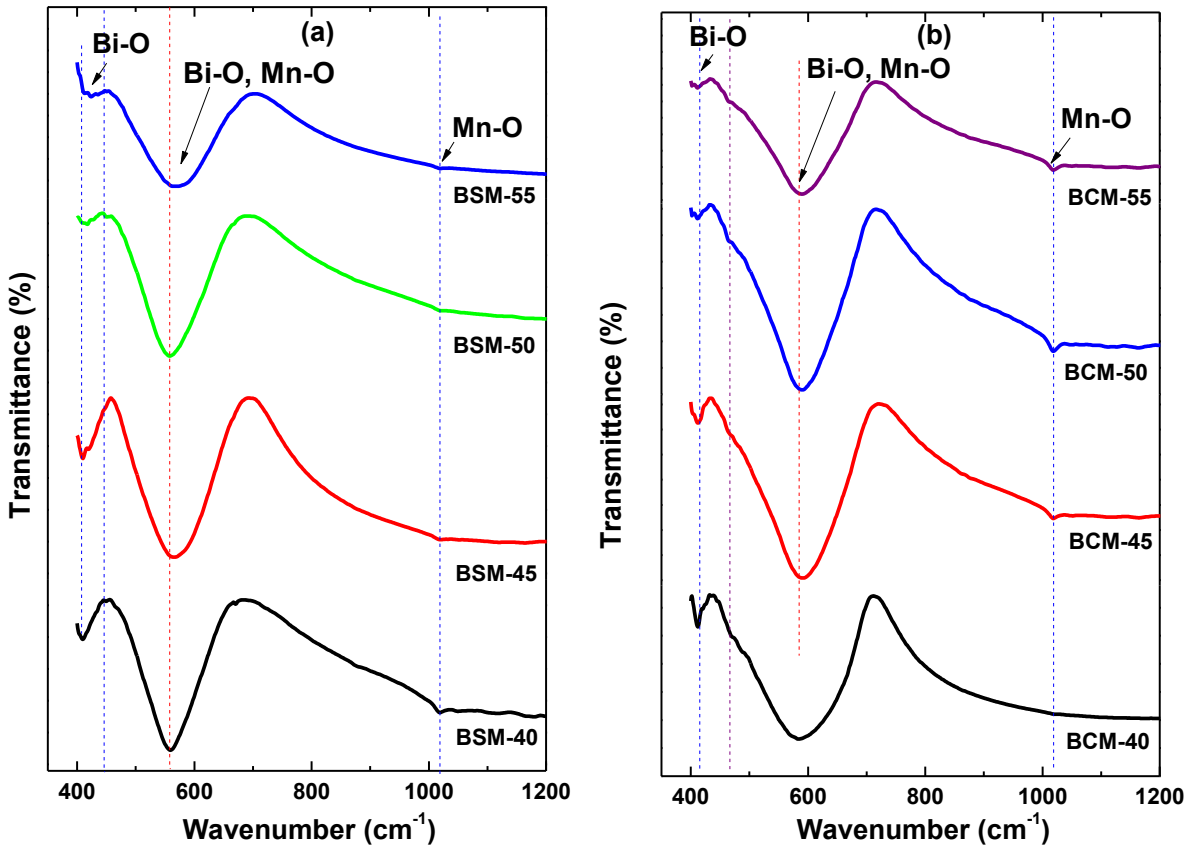

Figure 4.5: FT-IR spectra of (a) $Bi_{1-x}Sr_xMnO_3$ (b) $Bi_{1-x}Ca_xMnO_3$; $0.40 \leq x \leq 0.55$.

4.1.7 Microstructural study

The different morphologies of the grains can strongly affect the total conductivity of the system. So, the morphology of these systems has been discussed in this section. Figure 4.6(a) shows the SEM micrographs of $Bi_{1-x}Sr_xMnO_3$. The grains are equiaxed faceted type having variation in sizes for all the samples. The distribution of grains is uniform and well connected to each other due to better sinterability of the samples. The pores are non-uniform in all the samples. All the samples exhibit liquid phase sintering. The shining features appearing along the grain boundaries indicate the liquid phase sintering where the grain acquires a curvature shape (indicated by arrow in figure 4.6 (a) in BSM-40). A glassy layer is also formed along grain boundaries when the materials undergo liquid phase sintering. The liquid phase sintering is prominent in BSM-40 sample which can be due to the lower melting point of Bi_2O_3 as compared to SrO as Sr content in this sample is low as compared to other samples of

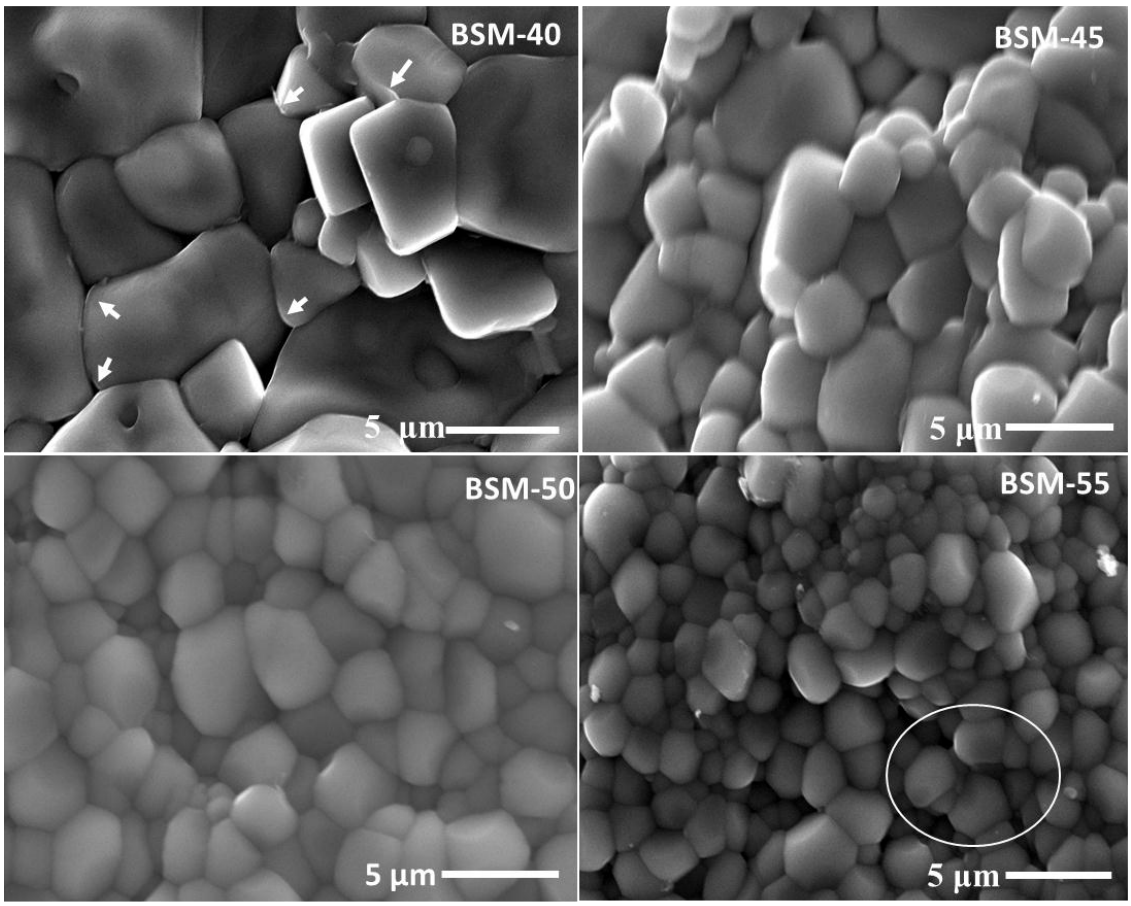

Figure 4.6 (a): Scanning electron micrographs of $Bi_{1-x}Sr_xMnO_3$ ($0.40 \leq x \leq 0.55$).

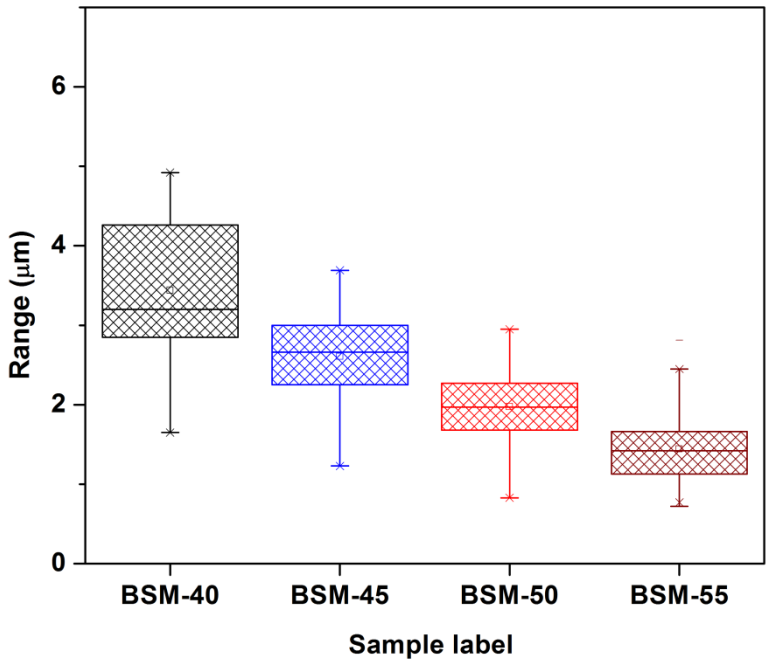

Figure 4.6 (b): Grain size distribution of $Bi_{1-x}Sr_xMnO_3$ ($0.40 \leq x \leq 0.55$). The central lines in the boxes represent the mean value.

the BSM system. Whereas, in other samples as shown in figure 4.6 (a), it can be observed that the small grains are dissolving to form the bigger grains (shown in BSM-55 with the circle). But simultaneously the increasing concentration of Sr will suppress the grain growth. The range of the grain sizes for different substituent concentrations are also shown in figure 4.6 (b) and the average value of grain size for each sample is given in table 4.2. It is also clear from the grain size data that BSM-40 sample exhibit highest grain size because of complete liquid phase sintering in this particular sample. It is also observed that with the increase of substituent concentration, the grain size decreases. It is also well reported in literature that addition of alkaline earth metals suppress the necking of grains due to reduced grain boundary mobility and decreases the grain size [24].

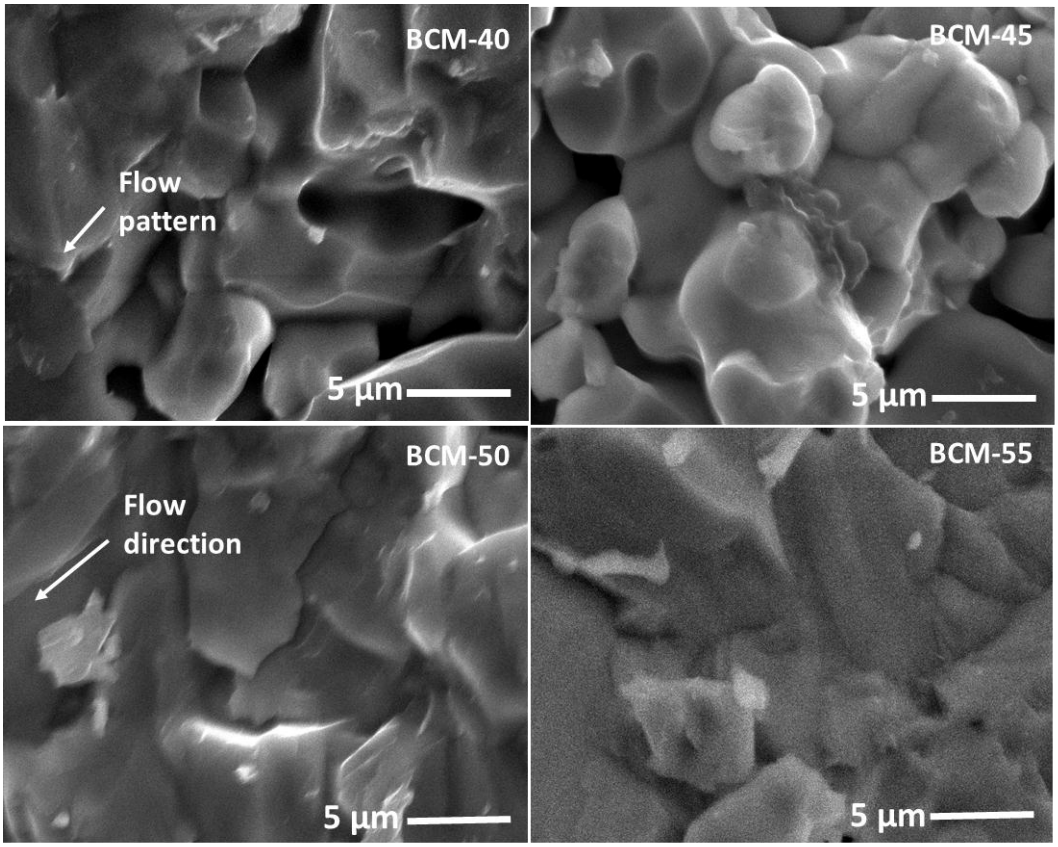

Figure 4.7 (a): Scanning electron micrographs of $Bi_{1-x}Ca_xMnO_3$ ($0.40 \leq x \leq 0.55$).

The micrographs of BCM samples are shown in figure 4.7 (a). The grains in all the BCM samples are unevenly distributed with higher porosity and larger grain size as compared to BSM samples. The grain size variation of all the samples with increasing substituent concentration is also given in figure 4.7 (b) and the average value of grain size for each sample is shown in table 4.2. The larger grains along with flow pattern are observed in all the

represented in figure 4.7 (b) and table 4.2, respectively. The average grain size of BCM samples is greater than as compared to BSM samples except BSM-40 sample. This can be due to the higher melting in BCM samples as compared to BSM sample. Moreover, Sr^{2+} substitution will more effectively exhibit the necking effect as compared to Ca^{2+} due to different ionic radii and polarization of two cations. It is well reported in literature that grain shape and grain size strongly affects the conductivity of the samples. Contrary to this, there is also conflicting statements regarding the effect of grains and grain sizes. However, in our systems the uniform and appropriate sizes of the grains in BSM system have positive influence on the conductivity and results in the higher conductivity of these samples as compared to BCM system (discussed in conductivity section).

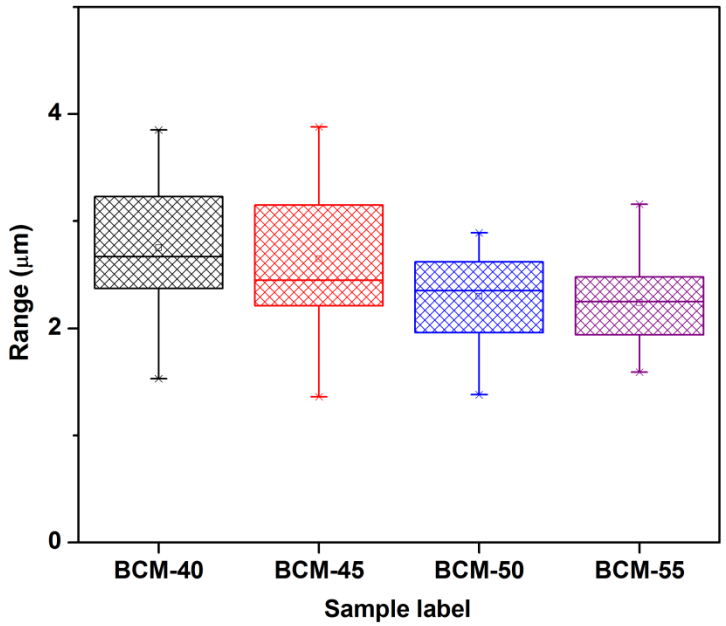

Figure 4.7(b): Grain size distribution of $Bi_{1-x}Ca_xMnO_3$ ($0.40 \leq x \leq 0.55$). The central lines in the boxes in above graph represent the mean value.

4.1.8 Thermal analysis

Figures 4.8 (a) and (b) show the thermogravimetric analysis of $Bi_{1-x}Sr_xMnO_3$ and $Bi_{1-x}Ca_xMnO_3$ ($0.40 \leq x \leq 0.55$) in the temperature range of 50 °C to 900 °C in both heating and cooling cycles in air. All the samples undergo weight loss up to 250 °C due to loss of moisture content from the sample. After that up to 600 °C, no weight change is observed for all the samples. After 600 °C, the samples again show weight loss which can be attributed to the generation of oxygen vacancies due to the conversion of Mn^{4+} into Mn^{3+}. In perovskite

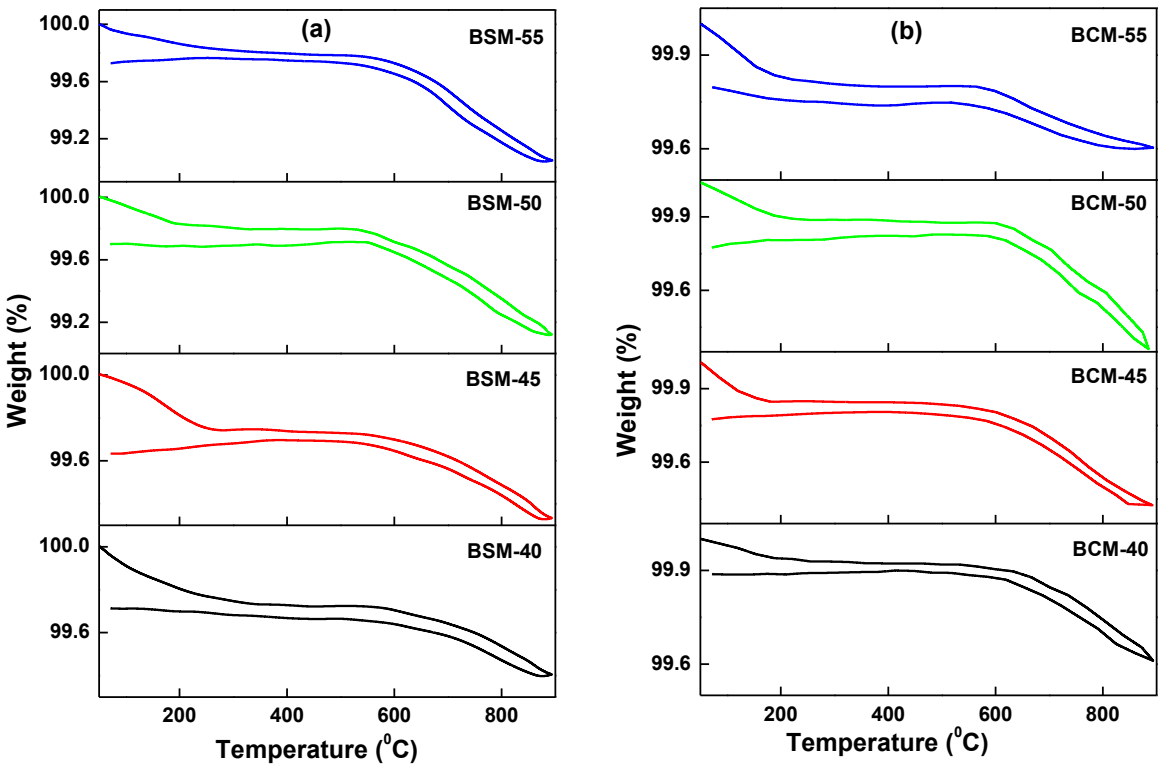

Figure 4.8: TGA curves of (a) $Bi_{1-x}Sr_xMnO_3$ (b) $Bi_{1-x}Ca_xMnO_3$; $0.40 \leq x \leq 0.55$.

materials release of oxygen occurs at elevated temperatures that lead to formation of distributed oxygen vacancies [25]. Thus, weight loss above 600 °C can be attributed to oxygen vacancies. During cooling cycle, the curve almost retrace the heating cycle which conforms that weight loss is due to the oxygen vacancies. However, it does not retrace below 250 °C which indicates that the weight loss up to this temperature is due to the moisture. In addition to this, BSM sample is more hygroscopic, particularly $Bi_{0.55}Sr_{0.45}MnO_3$ since the plateau at ~ 200 °C is suppressed as substitution concentration increases. It is well reported in literature that heavier alkaline earth metal (Sr) exhibits vigorous reaction with hydroxyl group than lighter one (Ca). So, BSM sample would be more hygroscopic than BCM. Moreover, the larger size of the Sr^{2+} as compared to Ca^{2+} leads to lower packing which create more free space in the unit cell and can attach more hydroxyl group.

Figure 4.9 (a) and (b) show the DTA curves of $Bi_{1-x}A_xMnO_3$ (A=Sr, Ca; $0.40 \leq x \leq 0.55$). This curve contains two peaks; one around 300 °C and second at 600 °C. The first peak (300 °C) can be attributed to the charge ordering temperature of these systems. The high charge ordering temperature (T_o) is attributed to $6s^2$ lone pairs in outermost shell of bismuth [26, 27]. This lone pair hybridizes with oxygen p-orbitals lowering the mobility of Mn electrons

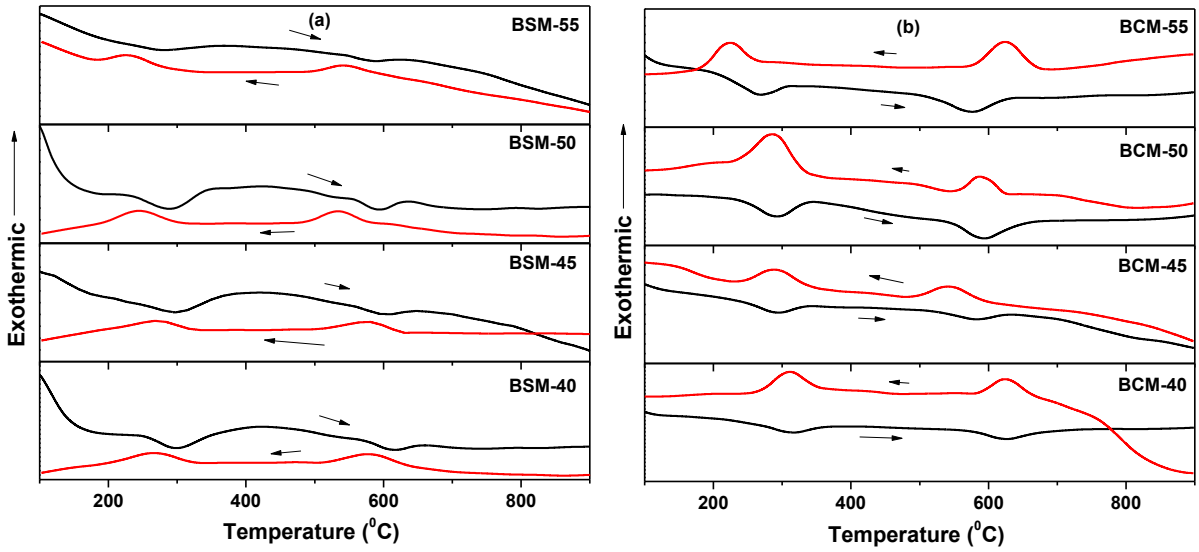

Figure 4.9: DTA curves of (a) $Bi_{1-x}Sr_xMnO_3$ (b) $Bi_{1-x}Ca_xMnO_3$; $0.40 \leq x \leq 0.55$.

and favors the charge ordering and charge localization. This peak shifts to lower temperature with increase in substituent concentration. With the increase in substituent concentration, bismuth content decreases causing a further decrease in the charge ordering and charge localization. Thus, T_o decreases with increasing content of substituents. The second peak (600 °C) can be devoted to the phase change from tetragonal/ orthorhombic to rhombohedral [28, 29]. With the substituent concentration this peak also shifts to lower temperature in all the samples. This transition is governed by the concentration of Mn^{4+}. With the substitution, the concentration of Mn^{4+} increases which lowers down the temperature of this transitions.

4.1.9 Thermal expansion coefficient (TEC)

In most of the perovskites, loss of lattice oxygen occurs at high temperatures which results in increase in thermal expansion of the oxides. Therefore, in addition to thermogravimetry measurements, the stability of materials with temperature can also be checked by dilatometry. The physical ($\Delta L/L_0$ versus temperature) and technical (d ($\Delta L/L_0$)/dT=α versus temperature) thermal expansion curves of all BSM samples are shown in figure 4.10. The calculated values of TEC for all the samples are given in table 4.5. It is clear from figure 4.10 that the relative change in length is not linear along the entire temperature range. Typically, there exists two temperature ranges for each sample where the relative change in length is linear but with different slopes. After 600 °C, TEC curve becomes steeper and there is a significant increase in TEC. This can be due to loss of lattice oxygen at higher temperatures and creation of oxygen vacancies. For every oxygen vacancy, two Mn^{4+} ions are converted into two Mn^{3+}

ions. The larger ionic radii of Mn^{3+} as compared to Mn^{4+} will increase the TEC values. The reduction of Mn^{4+} results in the transformation of crystal structure as explained in DTA section. Thermal expansion coefficient values increases from x=0.40 to 0.45, then decreases for x=0.50 and after that again shows an increasing trend for x=0.55. The reason for these anomalies is not yet known. It may arise due to symmetric distribution of grains in x=0.50 samples.

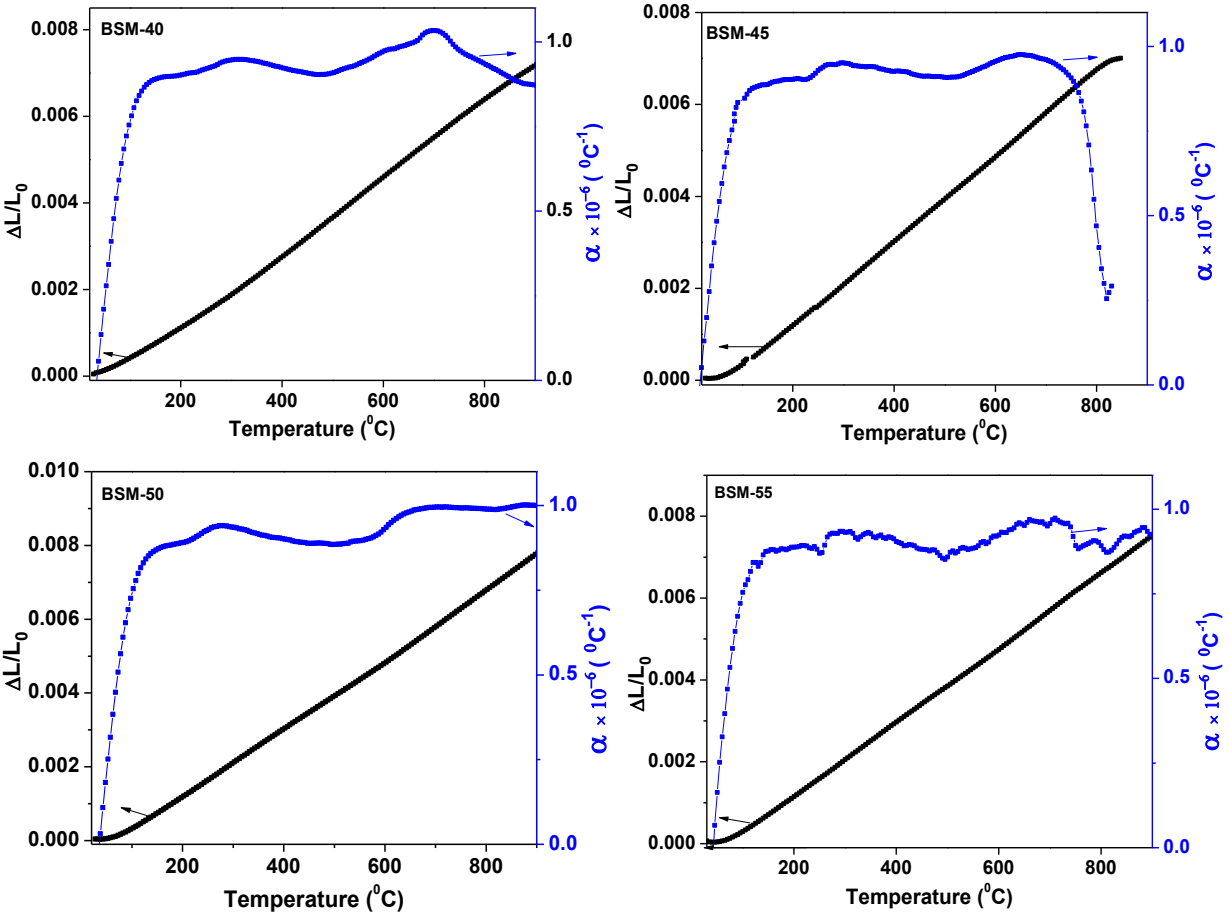

Figure 4.10: Thermal expansion curves of $Bi_{1-x}Sr_xMnO_3$ ($0.40 \leq x \leq 0.55$).

Table 4.5: Thermal expansion coefficient $Bi_{1-x}A_xMnO_3$ (A=Sr, Ca; $0.40 \leq x \leq 0.55$).

Sample Label	Thermal expansion coefficient ($\times 10^{-6}$ °C^{-1})	
	100 °C ≤ T ≤ 600 °C	600 °C ≤ T ≤ 800 °C
BSM-40	8.48	8.99
BSM-45	9.12	9.57
BSM-50	9.05	9.44
BSM-55	8.98	9.90
BCM-40	9.37	10.02
BCM-45	9.47	10.12
BCM-50	8.92	9.01
BCM-55	9.33	10.04

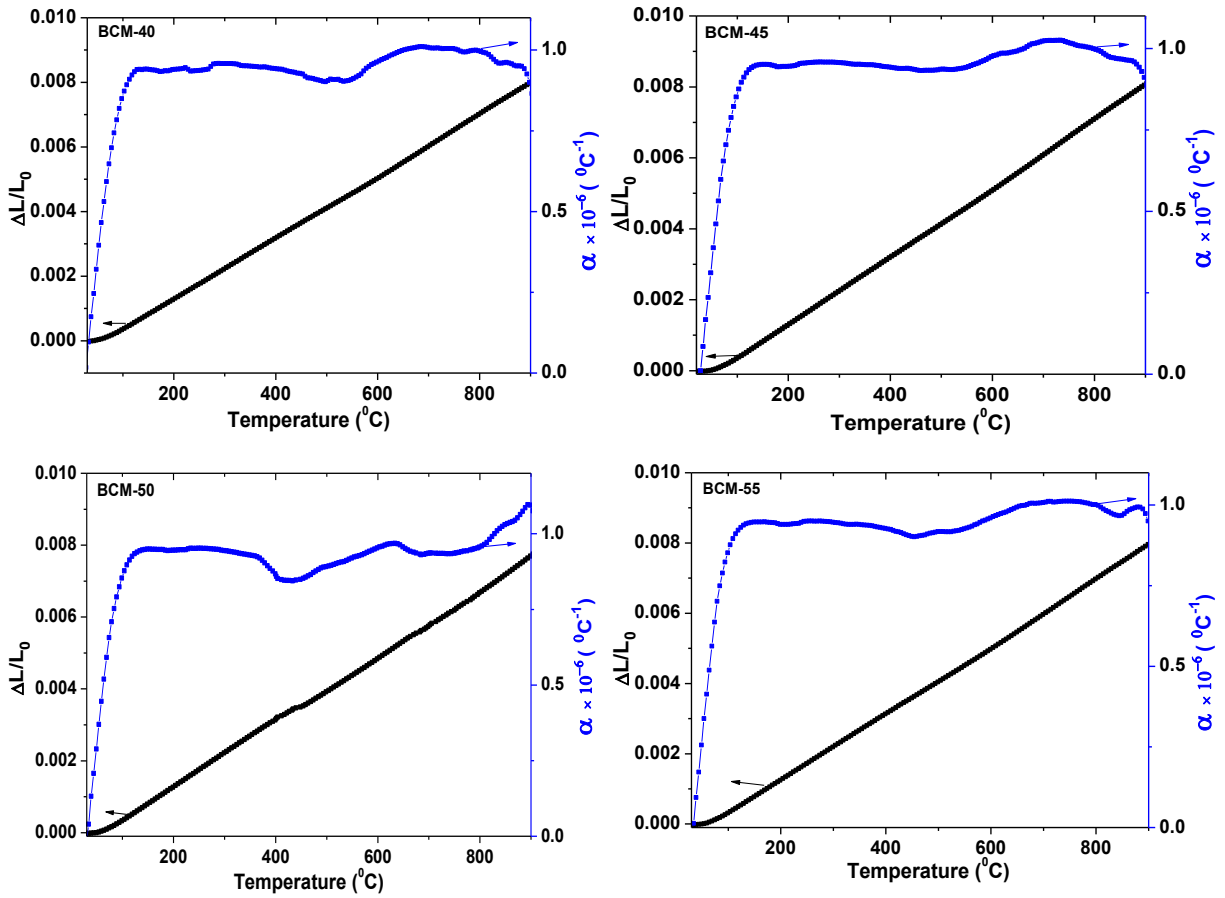

Figure 4.11: Thermal expansion curves of $Bi_{1-x}Ca_xMnO_3$ ($0.40 \leq x \leq 0.55$).

The thermal expansion curves for the BCM system are shown in figure 4.11. The curves of this system also exhibit two slopes as already discussed for Sr^{2+} substituted system. The values of thermal expansion coefficients are given in table 4.5. The TEC of this system also increases up to x=0.45 then decreases for x=0.50 and after that again increases for x=0.55. The TEC of Sr^{2+} doped $BiMnO_3$ is smaller as compared to Ca^{2+} doped $BiMnO_3$. This may be due to the larger specific free volume of BSM system as compared to BCM because higher free volume allows bonds to rotate and flex instead of stretch with increasing temperature and yield low TEC. The technical alpha curves of both the systems show two humps around 300 °C and 600 °C. The peak around 300 °C corresponds to charge ordering temperature (T_o) and other to crystal transformation and generation of oxygen vacancies as discussed in DTA curves.

4.1.10 Electrical conductivity

Figure 4.12 shows the Cole - Cole plot of the best conducting sample $Bi_{0.5}Sr_{0.5}MnO_3$ at 380 and 540 °C, respectively, as a representative curve. It exhibits a depressed semicircle which is

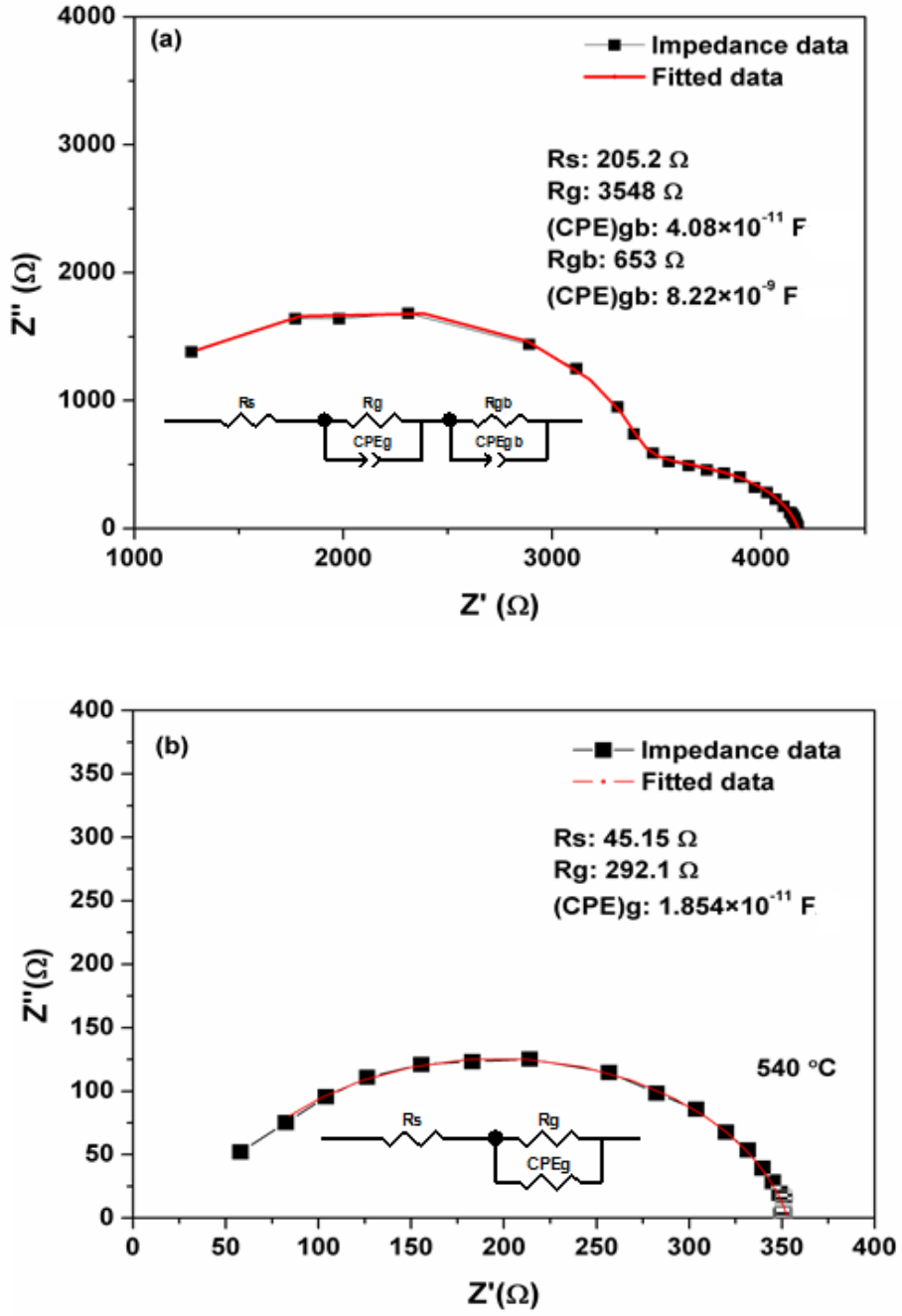

Figure 4.12: Cole - Cole plot of $Bi_{0.50}Sr_{0.50}MnO_3$ at (a) 380 ˚C and (b) 540 ˚C.

induced by the inhomogeneous and dispersion of electrodes, a constant phase element was introduced to replace the normal capacitor used in the fitting. At low temperatures two semicircles were observed which were fitted by using two parallel $R_s(R_gCPE_g)(R_{gb}CPE_{gb})$ circuits. R_s corresponds to the resistance in series, (R_gCPE_g) to the grain contribution and $(R_{gb}CPE_{gb})$ to the grain boundary contribution. However in the present case, at higher temperatures, only one semicircle was observed and fitted by using single $R_s(R_gCPE_g)$ circuit.

It is clear from the shape of the cole –cole plot that grain boundary and grain contribution both exists at low temperatures, but at high temperatures only grain contribution is observed. The total resistance of the sample was calculated by adding resistances from different contributions and the total conductivity was calculated by using the relation:

$$\sigma = l/RA \qquad [4.1]$$

where, *l* is thickness and *A* is cross-sectional area of gold sputtered pellet.

Arrhenius plots (*ln σT vs 1000/T*) for all the samples are given in figure 4.13 (a) and (b). These spectra are also fitted with the Arrhenius equation $\sigma T = \sigma_0 \exp\left(\frac{-E_a}{kT}\right)$ and activation energies calculated for all the samples are tabulated in table 4.6. The conductivity curves show a deviation at ~600 °C. This deviation is associated with phase transition as also observed in DTA (figure 4.9). At low temperatures, conductivity is mainly due to the polaron

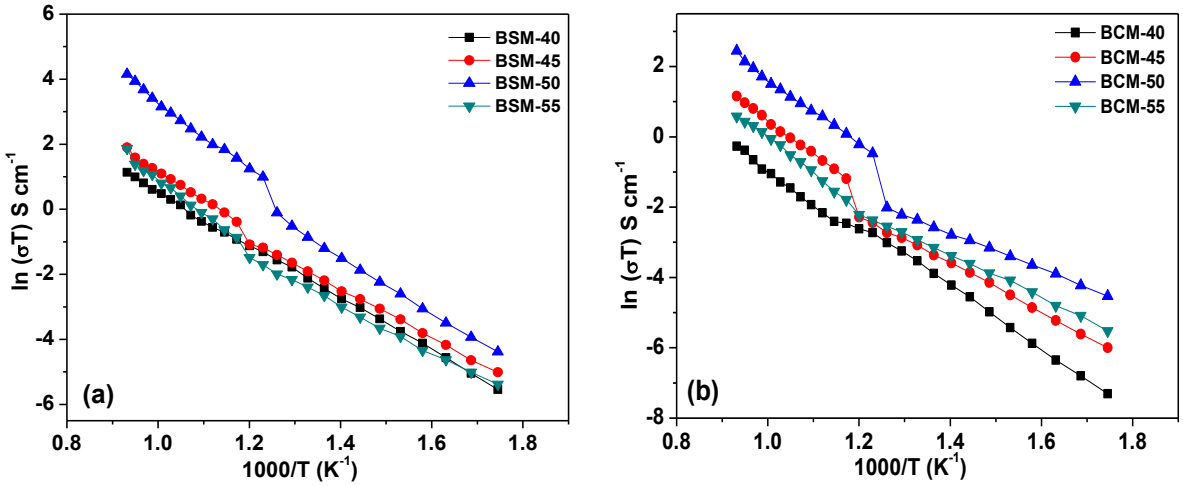

Figure 4.13: Arrhenius curves of (a) $Bi_{1-x}Sr_xMnO_3$ (b) $Bi_{1-x}Ca_xMnO_3$; 0.40≤x≤0.55.

conduction mechanism and at high temperatures the ionic conductivity contributes more due to the formation of more oxygen vacancies. So, change in slope can also be attributed to the change in charge carriers with temperature. The conduction phenomenon in these perovskites can be understood as follows:

In Sr^{2+}/Ca^{2+} doped $BiMnO_3$, Sr^{2+}/Ca^{2+} ions occupy Bi lattice sites, so, A'_{Bi} (A=Sr^{2+}/Ca^{2+}) are predominant defects in the system with effective negative charge. Then, electroneutrality in the system is maintained by the formation of tetravalent Mn ions (Mn_{Mn}) and doubly charged oxygen vacancies($V_{\ddot{O}}$). The non-stoichiometry of the $Bi_{1-x}A_xMnO_3$ (A=Sr, Ca; 0.40≤x≤0.55)

system increases with increasing temperatures. At higher temperatures, there is tendency for the formation of more oxygen vacancies and this happens by reduction of Mn^{4+} cations again into Mn^{3+} ions. The TGA also supports this phenomenon because higher weight loss is observed in TGA at high temperatures. This whole process can be explained by the equation [4.2]:

$$2Mn_{Mn}^{\cdot} + O_o^x \rightarrow 2Mn_{Mn}^x + V_o^{\cdot\cdot} + \frac{1}{2}O_2(g) \qquad [4.2]$$

With increase in substituent concentration (Ca/Sr), the conductivity also increases up to x=0.50 and after that decreases. As the substituent concentration is increased, there will be more chances of conversion of Mn^{3+} into Mn^{4+} and creation of oxygen vacancies occurs which increases the conductivity. Even there will be more Mn^{4+} which can be converted to Mn^{3+} at higher temperatures and will create more oxygen vacancies. As far as x=0.55 system is concerned, decrease in conductivity can be due to the oxygen ordering in this system. This type of phenomenon is well reported in doped ceramic samples [30].

As explained in the SEM analysis, the grain size decreases with increase in substituent concentration which further increases the number of grain boundaries per unit cross sectional area. At low temperatures, grain boundaries play vital role in conductivity but as temperature increases their role decreases substantially [31]. That is why in our system with increase in substituent concentration and decrease in grain size conductivity yet increases.

Conductivity of BSM system is higher than that of BCM system. This can be due to the more symmetric structure of BSM as compared to BCM as explained considering tolerance factor. Even it can also be explained on the basis of specific free volume of two systems. Lower specific free volume of BCM system hinders the movement of ions in crystal and results in low ionic conductivity of these samples. However, the total conductivity of the present system is quite low as compared to earlier reported values for $Bi_{0.50}Sr_{0.50}MnO_3$ [29]. It may be associated with the two different methods used to measure the conductivity [32]. Moreover, the thin glassy layer formed during the liquid phase sintering also acts as a blocking layer and reduces the conductivity [33]. Additionally, the microstructure of the ceramics also play important role to influence the conductivity [33, 34]. In the present studied system, highest conducting sample (x=0.50) exhibit relatively larger grain size (2.25 μm) as compared to reported one (1.80 μm) for similar system [29]. Moreover, in present studied system, lattice parameters are larger which implies the presence of higher concentration of

Mn^{3+} rather than Mn^{4+}. In order to make the system neutral, there will be more oxygen vacancies which should increase the ionic conduction. However, the ordered distribution of oxygen vacancies will decrease the conductivity in the present system [35].

Table 4.6: Activation energy for $Bi_{1-x}A_xMnO_3$ (A= Sr, Ca; $0.40 \leq x \leq 0.55$).

Sample Label	Activation Energy, E_a (eV)	
	300 °C ≤ T ≤ 600°C	**600 °C ≤ T ≤ 800 °C**
BSM-40	0.70	0.84
BSM-45	0.62	0.81
BSM-50	0.48	0.71
BSM-55	0.62	0.87
BCM-40	0.78	0.88
BCM-45	0.59	0.86
BCM-50	0.43	0.77
BCM-55	0.53	0.97

In Bismuth manganite series, it can be concluded that Substitution of Sr^{2+}/Ca^{2+} has resulted into more symmetric tetragonal and orthorhombic structure, respectively, as compared to monoclinic structure of undoped $BiMnO_3$. BSM system exhibits high conductivity as compared to BCM conductivity. Among all the studied samples, BSM-50 exhibit highest conductivity 0.099 S cm^{-1} at 800 °C with TEC in the range of 9.44×10^{-6} $°C^{-1}$.

4.2 $Bi_{1-x}A_xFeO_3$ (A=Sr, Ca; 0.40≤x≤0.55)

Undoped and doped $BiFeO_3$ has been studied for their multiferroic properties [36, 37]. These materials can also behave as p/n-type semiconductor and oxide ion conductor depending upon the partial pressure of oxygen and their synthesis conditions [38, 39]. Even $SrFeO_3$ has also been reported as mixed ionic- electronic conductor and have low thermal expansion coefficient values [40]. In the next series, $Bi_{1-x}A_xFeO_3$ (A=Sr, Ca; $0.40\leq x\leq0.55$) have been studied for structural, thermal and electrical properties.

4.2.1 Physical properties

The relative density, specific free volume and tolerance factor of all the studied samples are given in table 4.7. The density of all the samples are more than 95% of theoretical density and even the variation in density with increasing substituent concentration is also very small. Thus, structural and conductivity properties of all the samples will be least affected by the density variation. BSF system has high specific free volume and tolerance factor as compared to BCF system. This can be due to the larger unit cell volume of BSF as compared to BCF

and larger ionic radii of Sr^{2+} (1.26 Å) as compared to Ca^{2+} (1.12 Å). It also signifies that BSF system will be more symmetric as compared to BCF system.

Table 4.7: Composition along with Sample label, density, tolerance factor and specific free volume of $Bi_{1-x}A_xFeO_3$ (A=Sr, Ca; $0.40 \leq x \leq 0.55$).

Composition	Sample Label	Density			Tolerance factor	Specific free volume
		Theoretical density (d_{th}) (g cm^{-3})	Experimental density (d) (g cm^{-3})	(d/d_{th}) (%)		
$Bi_{0.60}Sr_{0.40}FeO_3$	BSF-40	7.20	6.87	95.4	0.835	0.325
$Bi_{0.55}Sr_{0.45}FeO_3$	BSF-45	6.90	6.63	96.1	0.836	0.320
$Bi_{0.50}Sr_{0.50}FeO_3$	BSF-50	6.80	6.52	95.8	0.837	0.319
$Bi_{0.45}Sr_{0.55}FeO_3$	BSF-55	6.70	6.50	96.7	0.837	0.307
$Bi_{0.60}Ca_{0.40}FeO_3$	BCF-40	6.78	6.58	97.1	0.821	0.319
$Bi_{0.55}Ca_{0.45}FeO_3$	BCF-45	6.58	6.35	96.0	0.825	0.310
$Bi_{0.50}Ca_{0.50}FeO_3$	BCF-50	6.36	6.15	96.7	0.828	0.306
$Bi_{0.45}Ca_{0.55}FeO_3$	BCF-55	6.12	5.82	95.1	0.829	0.296

4.2.2 X-Ray diffraction

The Rietveld refined X-ray diffraction (XRD) patterns of $Bi_{1-x}Sr_xFeO_3$ ($0.40 \leq x \leq 0.55$) are shown in figure 4.14. The calculated and observed patterns clearly indicate that XRD patterns are completely fitted. The lattice parameters and refinement parameters are given in table 4.8. Rietveld refinement results reveal that BSF samples have a tetragonal perovskite structure with *p4mm* space group up to x=0.50. However, for BSF-55, the XRD pattern shows some additional peaks which can be indexed to orthorhombic superstructure. The XRD pattern of SF-55 is completely refined with *pmma* symmetry. A detailed phase diagram study of SrO-Bi_2O_3-Fe_2O_3 system by Zaitsev et al. [41] shows that these peaks can be due to the tetragonal superstructure. On the other hand, additional peaks in $Sr_2LaFe_3O_8$ (double perovskite) has been indexed to orthorhombic crystal structure with *Pmma* space group [42]. However, in present studied samples, the XRD pattern of BSF-55 was fully refined with orthorhombic *Pmma* symmetry. The anomalies in fitted data of present sample and earlier reported data might have raised due to different site occupancies of Sr^{2+} or ordering of oxygen vacancies in some particular direction. With increasing Sr^{2+} concentration, lattice parameters should increase as ionic radii of Sr^{2+} is larger than Bi^{3+}. But in the present system with increasing concentration of Sr^{2+} the lattice parameters show decreasing trend. The opposite trend observed in present BSF system can be attributed to the creation of oxygen vacancies and transformation of Fe^{3+} to Fe^{4+} due to the charge imbalance created in the system after Sr^{2+}

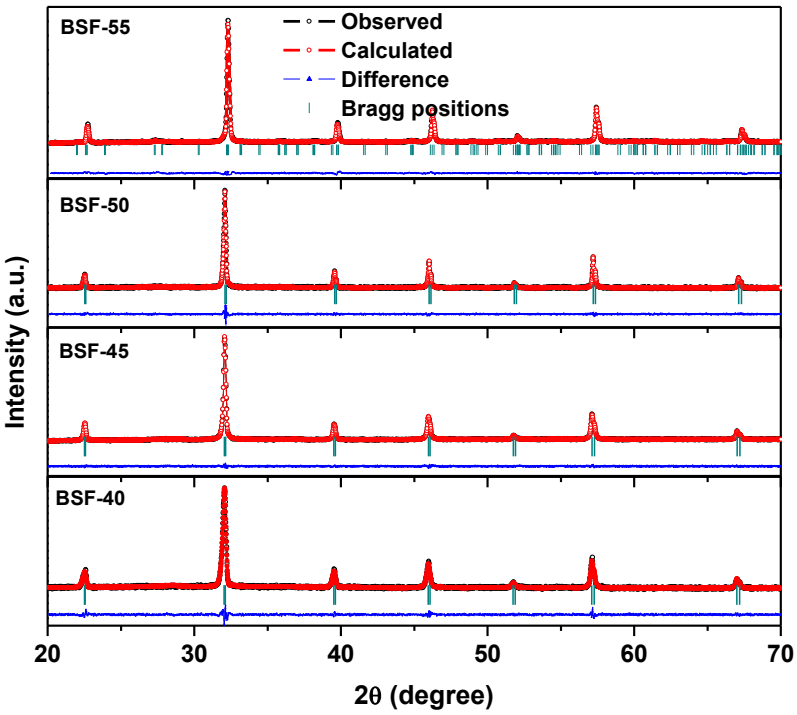

Figure 4.14: Rietveld refined X-ray diffraction pattern of $Bi_{1-x}Sr_xFeO_3$ ($0.40 \leq x \leq 0.55$).

substitution in place of Bi^{3+}. With the increase of oxygen vacancies in the system, the fraction of FeO_4 octahedra increases so coordination number of Fe^{3+} will change from 6 to 4 which will reduce the ionic radii and results in the decrement of lattice constants [43].

The Rietveld refined XRD patterns are shown in figure 4.15 for Ca^{2+} substituted system. The Ca^{2+} substituted system also show tetragonal structure up to BCF-50 with *p4mm* symmetry. The refined parameters along with the lattice parameters are given in table 4.8. After that, higher concentration of Ca^{2+} leads to the formation of secondary phase ($Ca_2Fe_2O_5$) in BCF-55. This phase is refined with *pnma* space group. The lattice parameters of this system also show decreasing trend with increasing Ca^{2+} concentration. This variation is quite obvious as ionic radii of Ca^{2+} is smaller than that of Bi^{3+} and moreover, the presence of oxygen vacancies will also reduce the lattice parameters.

Table 4.8: Lattice parameters and refined parameters of $Bi_{1-x}A_xFeO_3$ (A=Sr, Ca; $0.40 \leq x \leq 0.55$).

Sample Label	Lattice parameters (Å)	Wyckoff positions	Goodness of fit parameters		Grain size (μm)
			R_{wp} (%)	χ^2	
BSF-40	a = 3.9507(4) c = 3.9403(5)	Bi/Sr: (0,0,0) Fe: (0.5,0.5,0.412(4)) O1: (0.5,0.5,0.026(3)) O2: (0.5,0,0.452(2))	2.34	1.07	1.80
BSF-45	a = 3.9412(5) c = 3.9360(2)	Bi/Sr: (0,0,0) Fe: (0.5,0.5,0.474(4)) O1: (0.5,0.5,0.019(3)) O2: (0.5,0,0.552(2))	3.14	1.62	1.56
BSF-50	a = 3.9376(5) c = 3.9290(8)	Bi/Sr: (0,0,0) Fe: (0.5,0.5,0.562(4)) O1: (0.5,0.5,0.026(7)) O2: (0.5,0,0.552(2))	2.54	1.74	2.17
BSF-55	a = 5.5512(3) b = 11.8021(4) c = 5.4807(9)	Bi1/Sr: (0.25,0.5,0.744(3)) Bi1/Sr: (0.25,0.191(4), 0.730(7) Fe1: (0.25, 0.338(8),0.241(5)) Fe2: (0.207(8),0,0) O1: (0,0.302(5),0) O2: (0,0.340(6),0.5) O3: (0.25,0.5,0.200(1)) O4: (0.268(2),0.142(2),0.361(7)) O5: (0.134(2),0,0.875(2)) O6: (0.074(8),0,0.688(8))	2.10	1.28	2.01
BCF-40	a = 3.9208(3) c = 3.9174(7)	Bi/Sr: (0,0,0) Fe: (0.5,0.5,0.532(4)) O1: (0.5,0.5,0.046(3)) O2: (0.5,0,0.452(2))	3.02	1.74	2.98
BCF-45	a = 3.9197(8) c = 3.9078(4)	Bi/Sr: (0,0,0) Fe: (0.5,0.5,0.491(4)) O1: (0.5,0.5,0.146(3)) O2: (0.5,0,0.4811(2))	2.88	2.01	1.95
BCF-50	a = 3.9085(2) c = 3.8971(5)	Bi/Sr: (0,0,0) Fe: (0.5,0.5,0.501(4)) O1: (0.5,0.5,0.202(5)) O2: (0.5,0,0.482(2))	2.57	1.62	1.87
BCF-55	a = 3.9195(7) c = 3.9010(5)	Bi/Sr: (0,0,0) Fe: (0.5,0.5,0.512(4)) O1: (0.5,0.5,0.158(3)) O2: (0.5,0,0.432(2))	3.02	1.88	1.67

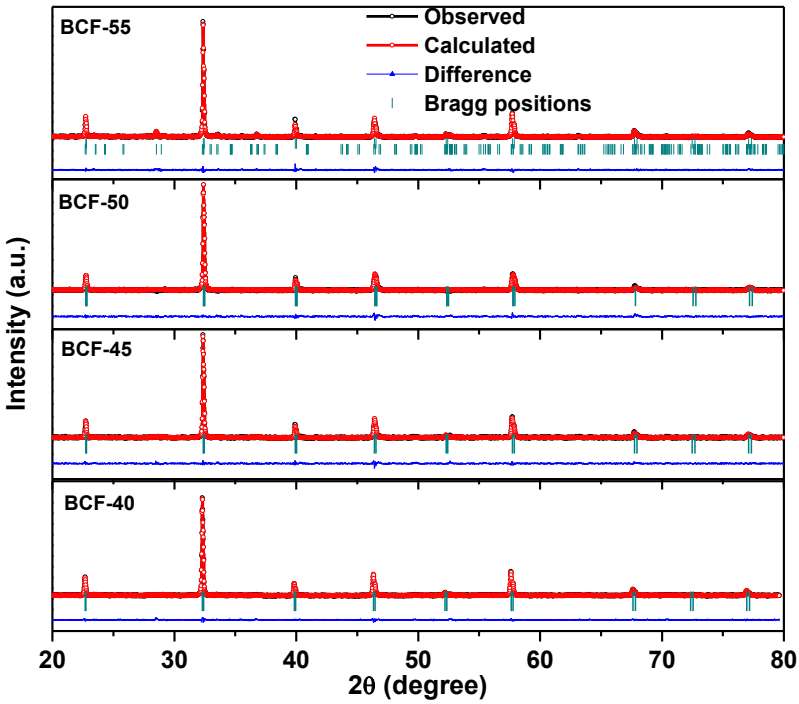

Figure 4.15: Rietveld refined X-ray diffraction pattern of $Bi_{1-x}Ca_xFeO_3$ ($0.40 \leq x \leq 0.55$).

Undoped $BiFeO_3$ shows the rhombohedral structure with R-3C space group [44]. The highly polarizable $6s^2$ electron pair displaces the Bi^{3+} ion from its centrosymetric position and are responsible for the rhombohedral structure of $BiFeO_3$. When aliovalent cations Sr^{2+}/Ca^{2+} are Substituted in place of Bi^{3+}, oxygen vacancies are created which suppresses this displacement and leads to the formation of a more symmetric environment around Bi^{3+} [45]. This type of changes in local environment leads to more symmetric tetragonal structure in the substituted samples. In BSF-55 sample, these oxygen vacancies got ordered and results in the orthorhombic superstructure [46].

4.2.3 X-ray photoelectron spectroscopy

The X-ray photoelectron spectrum of BSF-50 sample is shown in figure 4.16. The analysis of Fe $2p_{3/2}$ spectrum is quite complicated due to the huge background effect. The peaks around 710.7, 711.2 and 711.79 correspond to Fe $2p_{3/2}$. The peak located at 720.7 and 719.2 eV corresponds to $2p_{1/2}$ and satellite peak positions, respectively [47, 48]. Interestingly, the peaks corresponding to Fe^{2+} or Fe^{4+} are absent in this spectrum. It might be possible due to the huge background noise and small concentration of Fe^{4+} in the present system. The satellite peak in BSF spectra give significant information about the different chemical oxidation state of Fe. As Fe^{2+} and Fe^{3+} have different electrons in d^6 and d^5 shells. The satellite peak appeared at different positions during relaxation of metal ion and is characteristic of oxidation state of Fe.

It is well reported in literature that if the difference between $2p_{3/2}$ and satellite peak energy is around 6 eV then Fe may be present in Fe^{2+} state and if it is around 8 eV then in Fe^{3+} state [49]. In present studied sample the difference is more than 8 eV, so, shifting of peak can be attributed to the presence of Fe^{4+} state in $BiFeO_3$ system.

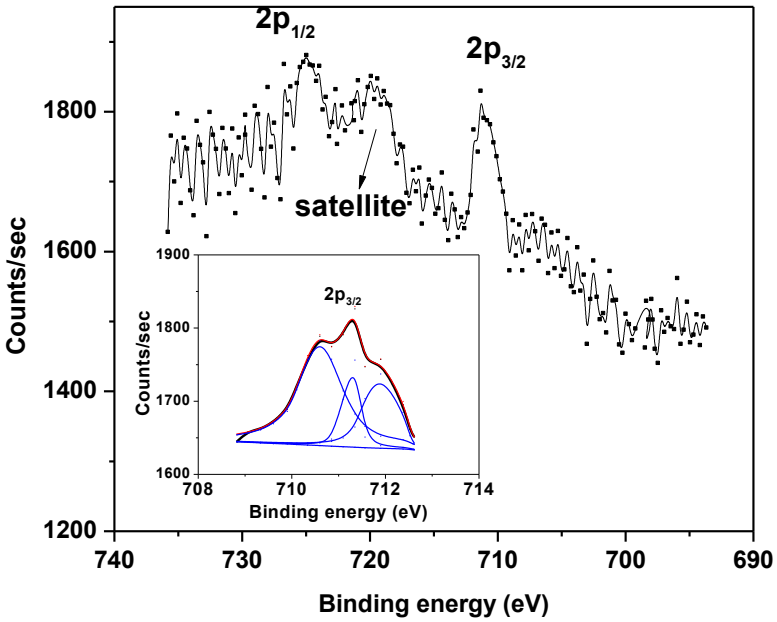

Figure 4.16: X-ray photoelectron spectra of BSF-50.

4.2.4 Iodometric titration analysis

From X-ray photoelectron spectra, it was not possible to confirm the presence of Fe^{4+}. So, in order to estimate the Fe^{3+}/ Fe^{4+} and oxygen content in the present studied samples, the iodometric titration was performed. The as obtained values are listed in table 4.9. It is clear from the results that Fe is present in Fe^{3+}/Fe^{4+} states and oxygen vacancies are also created to maintain the charge neutrality of the system. These results also indicate that charge imbalance in these systems is mainly compensated by the generation of oxygen vacancies and the concentration of Fe^{4+}. However, it is very low. As the concentration of substituent cation (Sr^{2+}/Ca^{2+}) increases, the non-stoichiometry in oxygen content and Fe^{4+} also increases.

The striking feature observed in Ca^{2+}/ Sr^{2+} substituted systems is that the conversion of Fe^{3+} into Fe^{4+} is more and oxygen vacancies concentration is low in Ca^{2+} as compared to Sr^{2+} substituted system. This can be correlated to the polarizing strength of both the cations because there is a strong correlation between the substituent polarizability and the oxygen vacancy ordering/disordering [50]. The polarizability of Ca^{2+} and Bi^{3+} is almost same, so,

there will be fewer tendencies to form the oxygen vacancies for maintaining the charge neutrality. So, in the present case more Fe^{3+} will get converted to Fe^{4+}. Whereas in case of Sr^{2+} substituted system, the polarizability difference between Sr^{2+} and Bi^{3+} is high which will create more disordering and higher number of oxygen vacancies. This is also supported by XRD and Raman spectroscopy.

Table 4.9: Oxygen and Fe^{4+} content as calculated from iodometric titration.

Composition	x=0.40		x = 0.45		x=0.50		x=0.55	
	Oxygen content (3- δ)	**Fe^{4+} content [(1-α) %]**	**Oxygen content (3- δ)**	**Fe^{4+} content [(1-α) %]**	**Oxygen content (3- δ)**	**Fe^{4+} content [(1-α) %]**	**Oxygen content (3- δ)**	**Fe^{4+} content [(1-α) %]**
$Bi_{1-x}Sr_xFeO_3$	2.81	2.1	2.79	3.2	2.77	3.9	2.75	4.5
$Bi_{1-x}Ca_xFeO_3$	2.82	4.1	2.80	5.0	2.78	6.8	2.77	7.9

4.2.5 Analysis of Raman spectra

The Raman spectra for $Bi_{1-x}A_xFeO_3$ (A=Sr, Ca; x=0.40, 0.50) samples are shown in figure 4.17. The spectra were deconvoluted into individual Lorentzian components and the peak position of each component i.e. natural frequency of each Raman mode was calculated. In the Sr^{2+}/ Ca^{2+} substituted samples, seven Raman active phonon modes A_1-2, A_1-4, E-3, E-4, E-7, E-8, E-9 at 189, 439, 256, 297, 502, 539 and 663 are obtained. According to selection rules 13, 8, 27 Raman active modes are assigned to rhombohedral, tetragonal and monoclinic symmetries, respectively for undioped $BiFeO_3$ [51]. These bands are consistent with earlier reported values for Sr^{2+}/Ca^{2+} subtituted BFO systems. The presence of these bands indicates towards the tetragonal structure of the present systems [52, 53]. All the Raman active modes of undoped $BiFeO_3$ (from literature data) are also tabulated in table 4.10 for comparison [53, 54]. The peak positions of Raman active modes have shifted to higher wavenumber side with Sr^{2+}/ Ca^{2+} substitution except A_1-4 mode in Sr^{2+} substituted system and E-3, E-4 modes in Ca^{2+} substituted system which are shifted to lower wavenumbers. The intensity of different peaks also changed noticeably with the substitution. The band at 650 cm^{-1} has also become much stronger than in the undoped sample. The changes in Raman spectra can be explained on the basis of; firstly the substitution of Sr^{2+}/Ca^{2+} disturbs the stereo-chemical activity of bismuth electron pair and thereby changes the Bi-O covalent bonds abruptly and lead to a phase transition, secondly, the atomic mass also plays an important role in the vibrating

system. The mode frequency is proportional to $(k/M)^{1/2}$. The atomic weights of Sr^{2+}/Ca^{2+} (87.62 g and 40.08 g, respectively) are less than that of bismuth (208.98 g). So, the shifting of Raman modes, disappearance of some modes and the change in crystal structure are also likely due to the A-site substitution by low atomic eight elements (lighter), thirdly, since Sr^{2+}/Ca^{2+} also create charge imbalance in the system due to the different valence states of Sr^{2+}/Ca^{2+} than Bi^{3+}. To compensate this charge imbalance, generation of Fe^{4+} and oxygen vacancies has taken place which also causes broadening /shifting/ disappearance of bands in

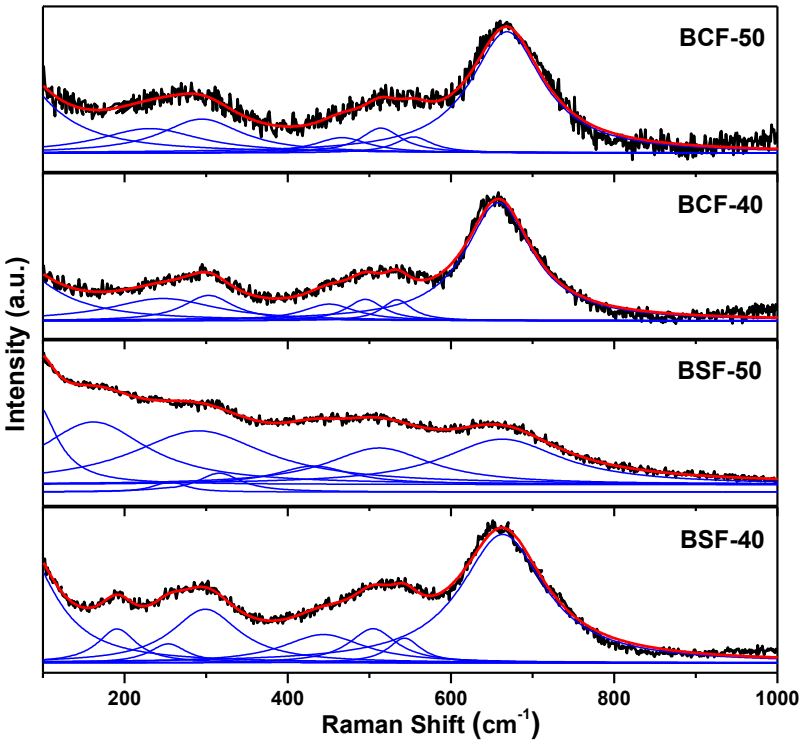

Figure 4.17: Raman spectra of $Bi_{1-x}A_xFeO_3$ (A=Sr, Ca; x=0.40, 0.50).

Raman spectra [55, 56]. Moreover, band broadening is prominent in Sr^{2+} doped system as compared to Ca^{2+} doped system. Both Sr^{2+} and Ca^{2+} are alkaline earth metals but they behave in a different way in both the systems. The Ca^{2+} doped samples show a small change in their peak positions as compared to Sr^{2+} doped systems. Even in $B_{0.50}Sr_{0.50}FeO_3$ system, Raman spectra shows drastic changes as compared to $Bi_{0.60}Sr_{0.40}FeO_3$ whereas, Raman spectra of $B_{0.50}Ca_{0.50}FeO_3$ show a very small change as compared to that of $Bi_{0.60}Ca_{0.40}FeO_3$. The main cause of this anomaly is the difference in ionic radii and atomic weights of Sr^{2+} and Ca^{2+} solutes. Incorporation of Sr^{2+} into $BiFeO_3$ will create more disorder in the system by creating more oxygen vacancies as also confirmed by iodometric analysis. The reduced phonon modes and shifting/ broadening of Raman modes confirms the transformation of crystal structure

into much more symmetric tetragonal structure as compared to rhombohedral structure of undoped $BiFeO_3$ which is also well supported by XRD data. .

Table 4.10: Comparison of Raman peak positions for the studied samples $Bi_{1-x}A_xFeO_3$ (A=Sr, Ca; x=0.40, 0.50) and reported data.

Raman modes (cm^{-1})	**Kothari *et al.* [53]**	**Varshney *et al.* [54]**	**BSF-40**	**BSF-50**	**BCF-40**	**BCF-50**
A_1-1	135.15	143.97	-	-	-	-
A_1-2	167.08	175.92	189	169	-	-
A_1-3	218.11	233.37	-	-	-	-
A_1-4	430.95	-	439	432	450	463
E-1	71.39	-	-	-	-	-
E-2	98.36	104.92	-	-	-	-
E-3	255.38	-	256	260	243	230
E-4	283.0	281.09	297	300	303	293
E-5	321.47	372.15	-	-	-	-
E-6	351.55	-	-	-	-	-
E-7	467.60	477.22	504	510	495	510
E-8	526.22	528.95	539	-	534	554
E-9	598.84	626.81	660	663	657	662

4.2.6 Fourier transform infrared analysis

Figures 4.18 (a) and (b) show the FT-IR spectra BSF and BCF, respectively, in wavenumber range of 400-1200 cm^{-1}. The two major absorption bands around 420-430 cm^{-1} and 590-600 cm^{-1} are observed for all the samples. The band around 420-430, 590-600 cm^{-1} can be attributed to the stretching vibration of Fe-O bond in the FeO_6 octahedral unit and also due to the BiO_6 octahedral structural unit [57, 58]. The presence of metal oxygen bond also confirms the formation of perovskite compounds. The two small shoulders can also be seen around 670 and 720 cm^{-1} in all the substituted samples. The band around 670, 720 cm^{-1} can be assigned to the bending modes of vibrations of Fe-O stretching vibrations with overlapped band of Bi-O at 670 cm^{-1} [59-60]. In all the FT-IR spectra, three peaks between 500 and 720 cm^{-1} are present which clearly indicates the presence of most of Fe in Fe^{3+} state in the present studied systems. With increasing substituent concentration, a shift in FT-IR bands towards higher wave number side can also be observed from the spectra. This effect is same for both Sr^{2+} and Ca^{2+} substituted systems. This shift can be due to the smaller atomic number of Sr^{2+} and Ca^{2+} as compared to Bi^{3+}. It is well reported in literature that substitution of lower atomic number element shifts the spectra to higher wavenumber side [20]. Sr^{2+} substituted samples show higher shift in their wavenumbers as compared to Ca^{2+} substituted samples. It could be related to the larger ionic radii of Sr^{2+} as compared to Ca^{2+}. Additionally, it is also associated

with the presence of higher content of oxygen vacancies as discussed in iodometric titration section. These results also supports the XRD and Raman data which clearly indicates that Sr^{2+} substitution has affected the crystal structure more strongly as compared to Ca^{2+} substituted samples.

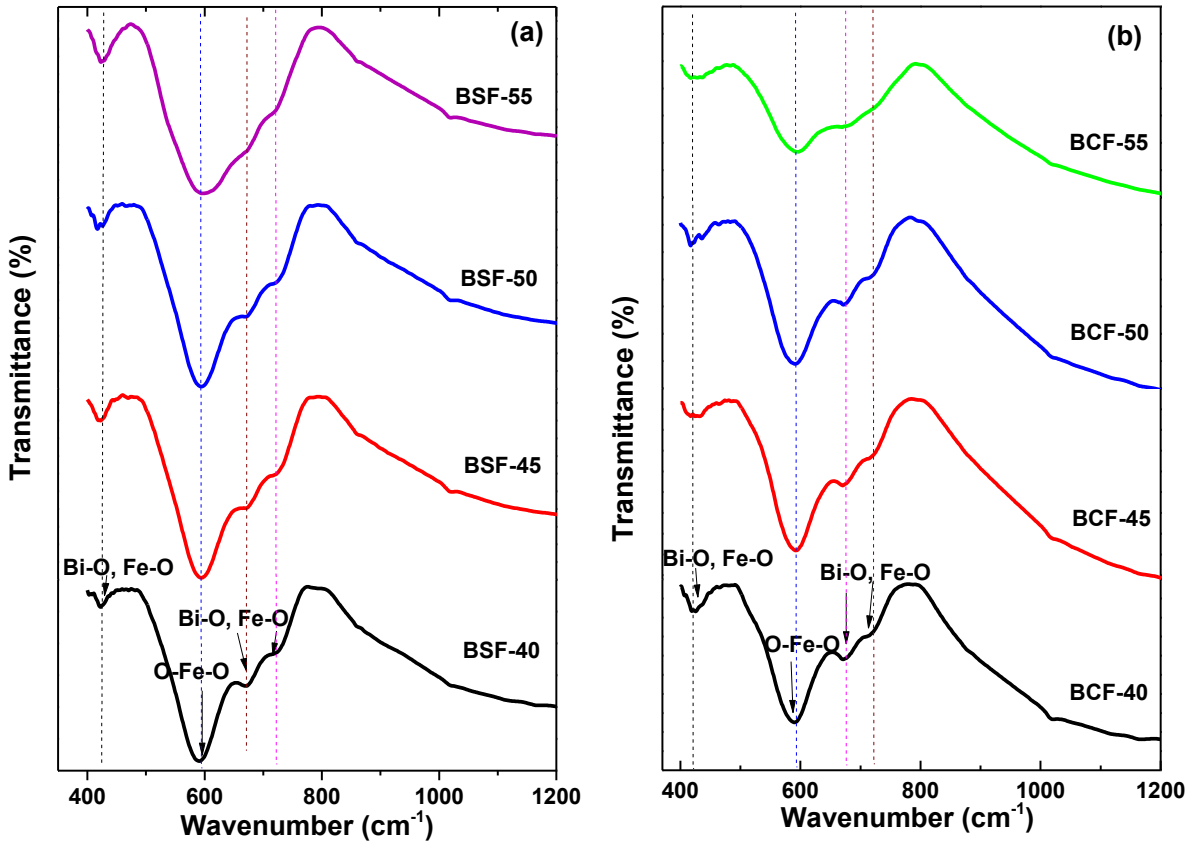

Figure 4.18: FT-IR spectra of (a) $Bi_{1-x}Sr_xFeO_3$ (b) $Bi_{1-x}Ca_xFeO_3$; $0.40 \leq x \leq 0.55$.

4.2.7 Microstructural study

The scanning electron micrographs obtained from the fractured surface of the sintered pellets of $Bi_{1-x}Sr_xFeO_3$ ($0.40 \leq x \leq 0.55$) are shown in figure 4.19 (a). The grains are equiaxed faceted type with variation in size for all the samples. The black area which looks like pores is due to detachment of grains. The dispersion in grain size values with the variation in Sr^{2+} concentration is shown in figure 4.19 (b) and their average values are tabulated in table 4.8. It is clear from the micrographs that all the samples have undergone liquid phase sintering and exhibit higher density [64]. Grain size decreases with increase in substitution up to x=0.45 and BSF-45 as compared to BSF-40 can be explained on the fact that substitution of

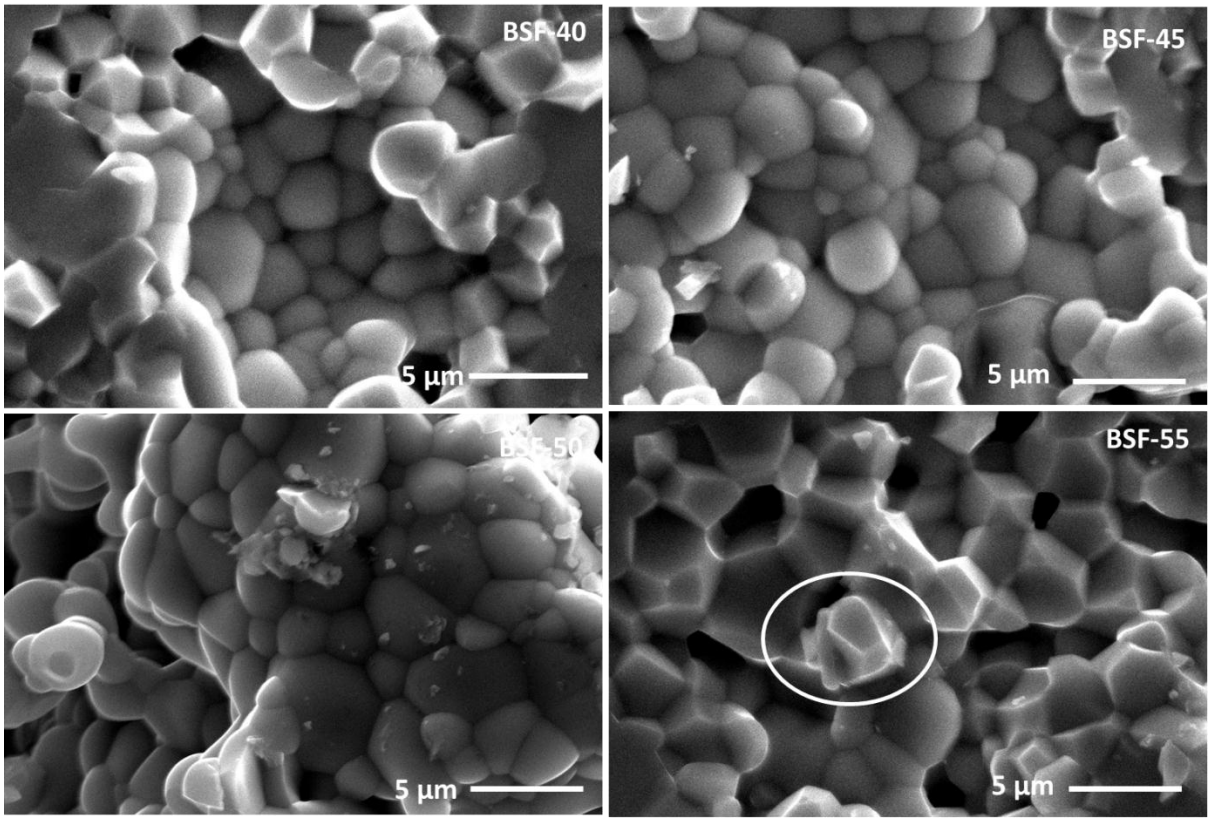

Figure 4.19 (a): SEM micrographs of $Bi_{1-x}Sr_xFeO_3$ ($0.40 \leq x \leq 0.55$).

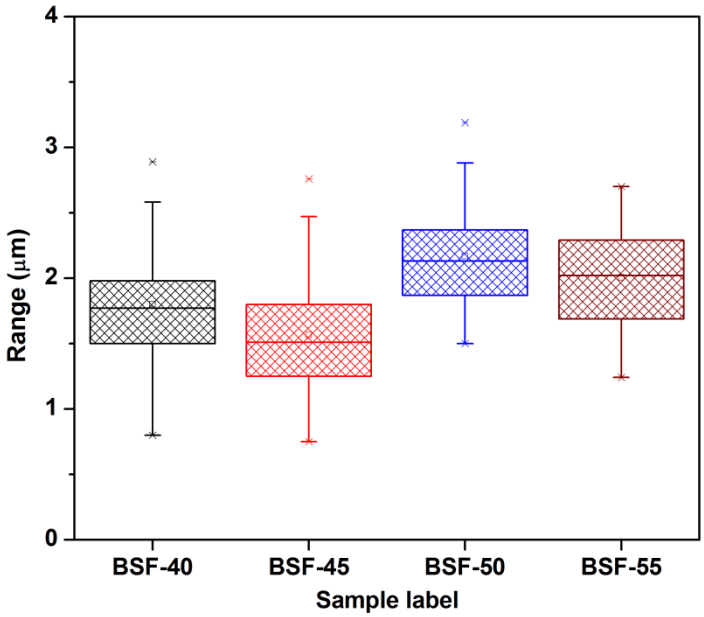

Figure 4.19 (b): Grain size distribution of $Bi_{1-x}Sr_xFeO_3$ ($0.40 \leq x \leq 0.55$). The central lines in the boxes represent the mean value.

Sr^{2+} further restricts the grain growth as it provides large number of nucleating sites for grains thus facilitating more number of grains. It is well known fact that substituting cation such as alkaline earth metallic cation suppresses necking of grains due to reduced grain boundary mobility which then hindered the densification [24]. However, after BSF-45, the substitution of Sr^{2+} does not restrict the grain growth due to its maximum solubility at this point and after that grain size again starts increasing due to liquid phase sintering. It is observed that all the samples exhibit similar morphology except BSF-55. The faceted structure is more pronounced for BSF-55 sample, where, sharp polygonal grains appear. However, the interesting feature observed in BSF-55 sample is the existence of different cleavage planes for the grains as shown in circle in BSF-55. In ceramic samples, defect formation is strongly affected by condition of charge neutrality because creation of imbalanced charges acquires higher energy state and provides cleavage planes within a grain [65]. Formation of ordered oxygen vacancies may be the reason for such a cleavage.

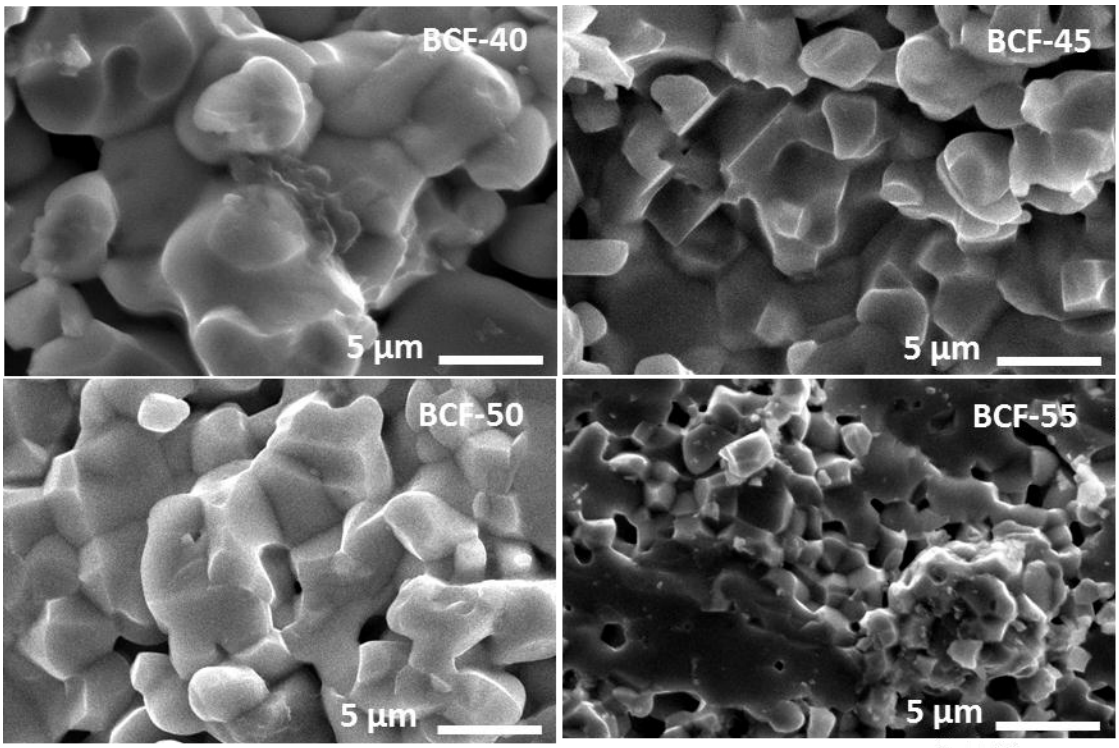

Figure 4.20 (a): SEM micrographs of $Bi_{1-x}Ca_xFeO_3$ ($0.40 \leq x \leq 0.55$).

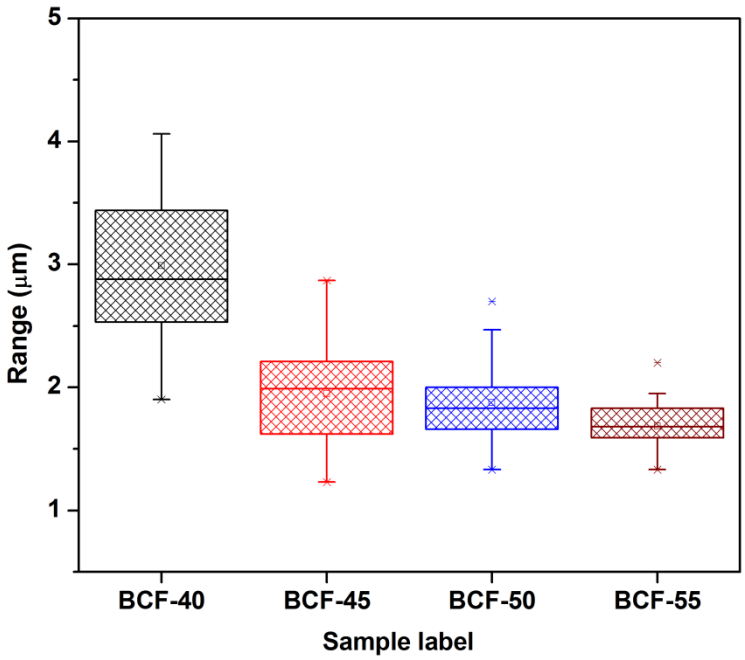

Figure 4.20 (b): Grain size distribution of $Bi_{1-x}Ca_xFeO_3$ ($0.40 \leq x \leq 0.55$). The central lines in the boxes graph represent the mean value.

The micrographs of BCF samples are shown in figure 4.20 (a). The distribution of grain sizes for all the samples are shown in figure 4.20 (b) and average value of the respective grain size of each sample is given in table 4.8. It is clear from the data that with increasing Ca^{2+} substitution grain size decreases. This can be due to the necking effect of Ca^{2+} up to BCF-50 composition. However, for BCF-55 sample, it may be possible the segregation of secondary ($Ca_2Fe_2O_5$) phase at the grain boundaries restrict the grain growth. As compared to BSF-40 sample, BCF-40 has the higher grain size which can be associated with more liquid phase sintering in this particular sample. But other than BCF-40, all the samples have smaller grain size as compared to BSF samples.

4.2.8 Thermal properties

Fig. 4.21 (a) and (b) shows the DTA curves of $Bi_{1x}A_xFeO_3$ (A=Sr, Ca; $0.40 \leq x \leq 0.55$) in the temperature range of 100 - 900 °C in both heating and cooling cycles. All the samples show two peaks around 360 °C and 750 °C. During cooling, these transitions shift towards lower temperature as compared to heating curves. These transitions are reversible as shown in fig. 4.21. First endothermic peak (360 °C) corresponds to Neel's temperature (T_N) and arises due to the magnetic phase transition i.e. antiferromagnetic to paramagnetic transition [66].

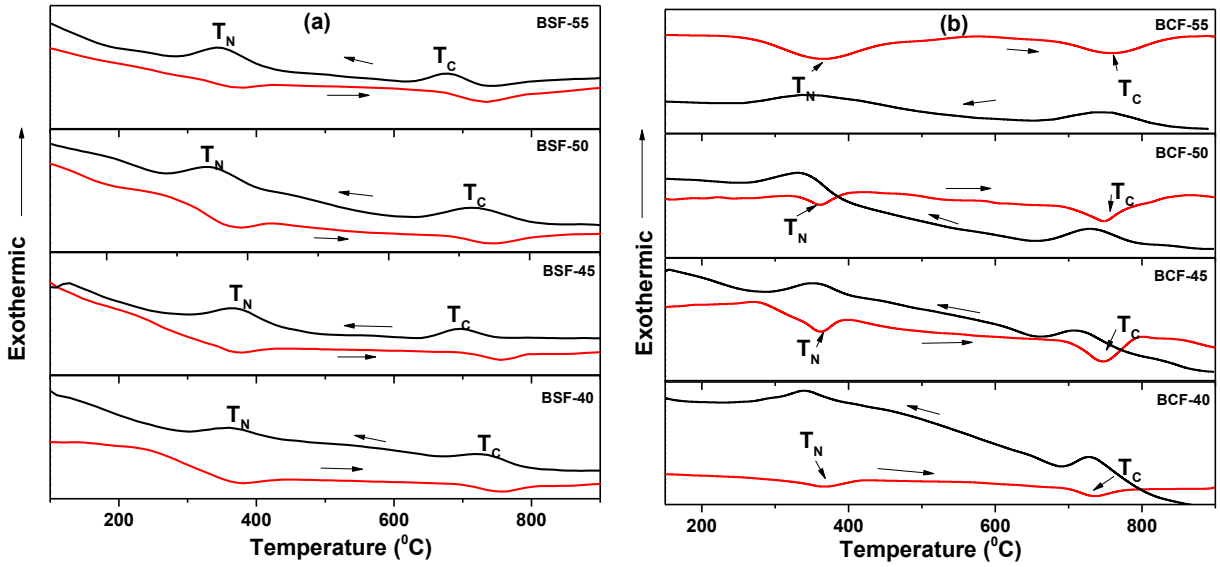

Figure 4.21: DTA curves of (a) $Bi_{1-x}Sr_xFeO_3$ (b) $Bi_{1-x}Ca_xFeO_3$; $0.40 \leq x \leq 0.55$.

Second endothermic peak (750 °C) belongs to ferroelectric to paraelectric phase transition i.e. Curie temperature (T_c). Similar transitions have also been reported by other researchers [67]. With the increase in A-site substituent (Ca^{2+}), second peak (T_c) shifts marginally towards lower temperature and also become diffused, whereas, no significant change is observed in case of first peak i.e. magnetic phase transition temperature (T_N). It is reported in literature that A and B sites (ABO_3) substitutions are responsible for ferroelectric (Curie temperature) and magnetic phase transitions (Neel's temperature), respectively [68]. Thus, Neel's temperature (T_N) does not show any change and ferroelectric temperature (Curie temperature) changes with the substituent concentration because substitution has taken place only at A-site in present system. The broadening of these peaks can be attributed to the oxygen disordering in the system which arises due to the substitution of Sr^{2+}/Ca^{2+} in place of Bi^{3+}. This disordering will affect the long range ferroelectric order and will reduce the Curie temperature [69].

The thermogravimetric (TG) measurements are performed in air for all the samples and are shown in figure 4.22. TG measurements in air show that all the samples undergo weight change up to 300 °C due to the loss of moisture content as well as trapped water in the pores. After that, there is weight gain in all the samples which also increases with the increase in temperature. The weight gain above 300 ˚C is very marginal ~0.15-0.5% in all the samples. The present studied systems have inherent oxygen deficiency due to the charge imbalance created by the Sr^{2+}/Ca^{2+} substitution. So, the weight gain in air atmosphere can be ascribed

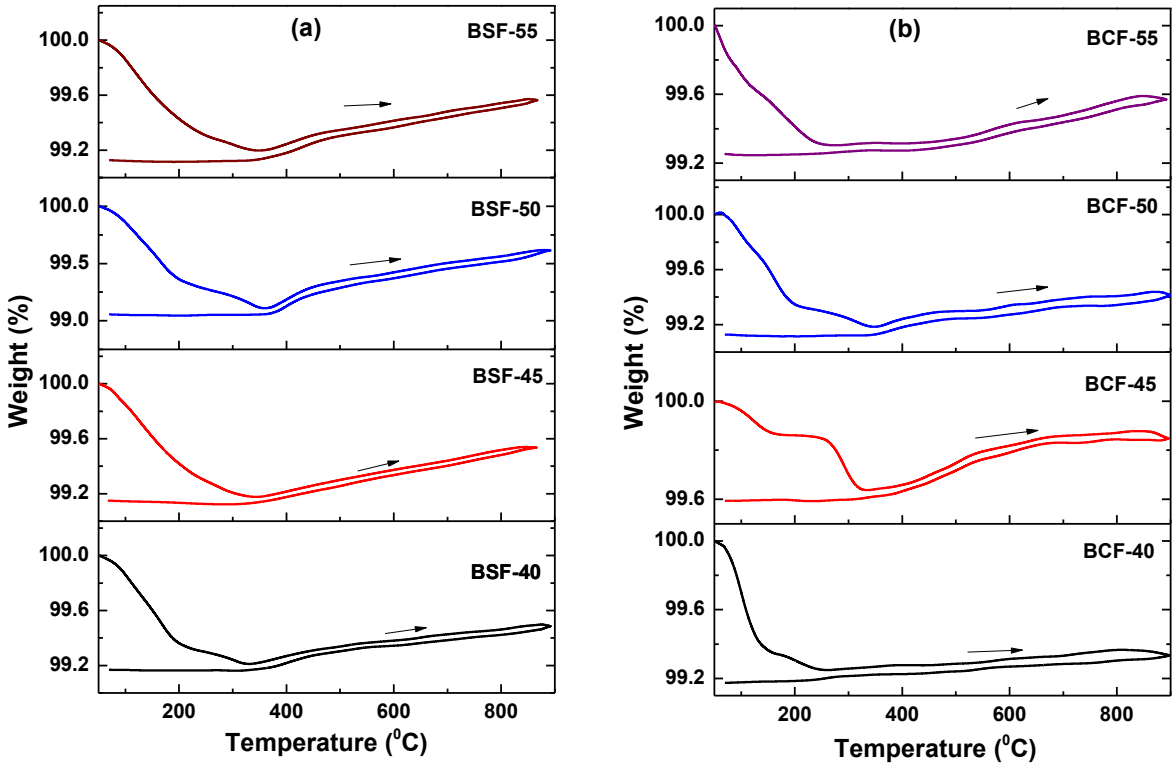

Figure 4.22: TGA curves of (a) $Bi_{1-x}Sr_xFeO_3$ (b) $Bi_{1-x}Ca_xFeO_3$; $0.40 \leq x \leq 0.55$.

due to oxidation of Fe^{2+}/Fe^{3+} to Fe^{4+} which leads to annihilation of oxide vacancies and formation of oxide lattice ions [70]. The XRD refinement results discussed in previous section shows a slight decrease in lattice parameter with increase in Sr^{2+}/Ca^{2+} content up to x=0.50. This decrease in lattice parameter indicates a decrease in average metal – oxygen (Bi-O or Fe-O) and metal-metal (Fe-Bi) bonds. The decrease in bond distance increases the electron density around B-site cations which results in an increase of oxidation state of transition metal cations and leads to weight gain at higher temperatures [71].

4.2.9 Thermal expansion coefficient

The variation of thermal expansion ($\Delta L/L_0$ versus temperature) with temperature for all the BSF samples is shown in figure 4.23. In order to examine the effect of phase transition and formation of oxygen vacancies, the technical thermal expansion curve ($\alpha = d(\Delta L/L_0)/dT$ versus temperature) is also given in figure 4.23. The measured values of thermal expansion coefficients in different temperature range are listed in table 4.11. Up to 600 °C, with an increase in substituent concentration in BSF-40 and BSF-50 samples, there is only a slight increase in thermal expansion coefficient. For higher concentration, BSF-55, the reverse trend

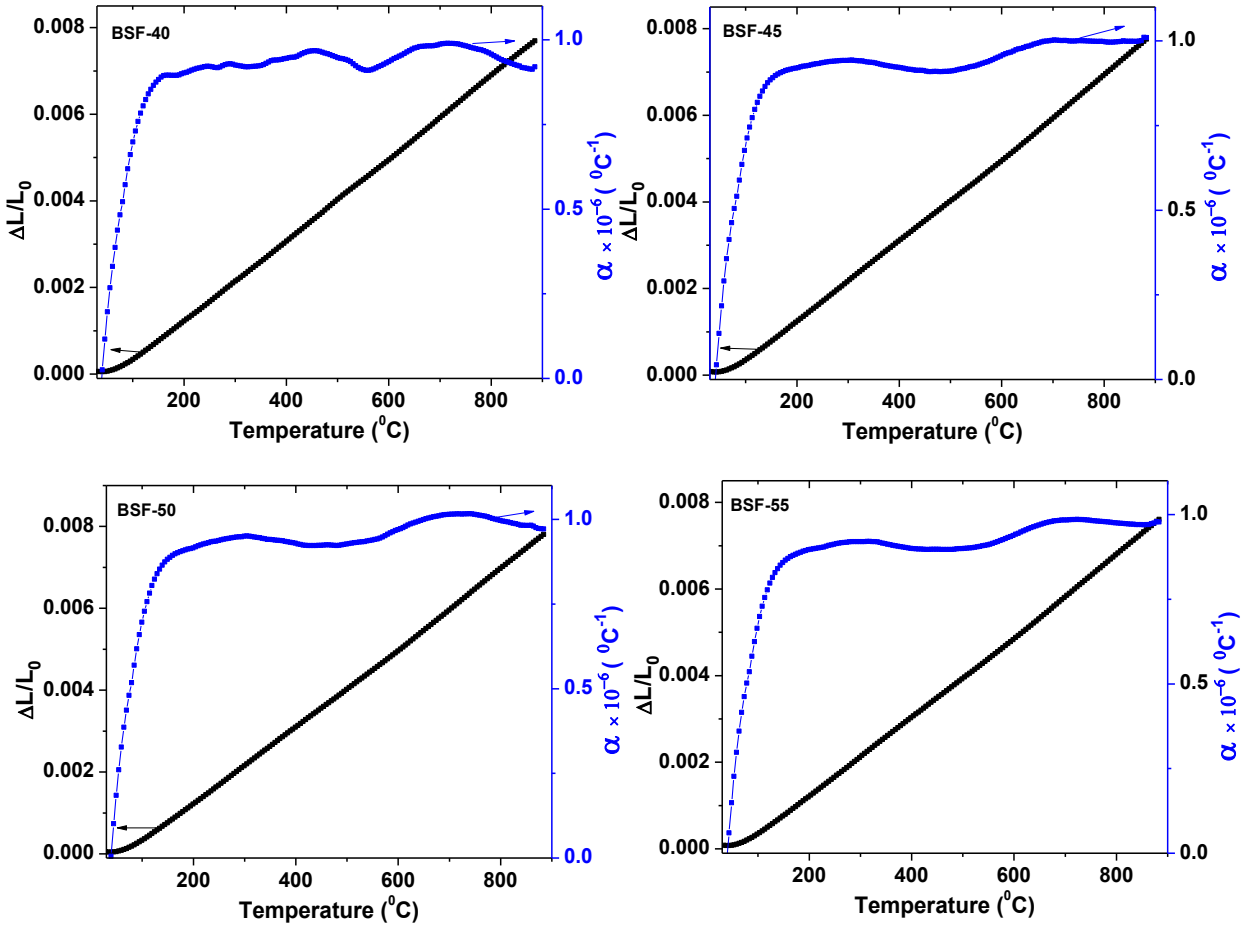

Figure 4.23: Thermal expansion curves of $Bi_{1-x}Sr_xFeO_3$ ($0.40 \leq x \leq 0.55$).

is observed. The decrease in TEC for BSF-55 may be due to the presence of superstructure and ordering of oxygen vacancies. The ordering of oxygen vacancies makes potential energy well more symmetric and reduces the TEC. The curve becomes steeper at higher temperatures and there is a significant increase in thermal expansion coefficient above 600 °C. This may be attributed to loss of lattice oxygen at higher temperatures and the formation of oxygen vacancies [72-73]. As the Sr^{2+} content increases there are more chances for the formation of oxygen vacancies with the higher disordering in the system. The TEC curves for BCF system is shown in figure 4.24 and the calculated values of TEC values in different ranges are given in table 4.11, respectively. Up to 600 ˚C, the change in TEC values with increasing Ca^{2+} concentration is very negligible. After 600 ˚C, the TEC increases with increasing Ca^{2+} concentration. This change can be attributed to the generation of more oxygen vacancies at elevated temperatures as described in BSF system.

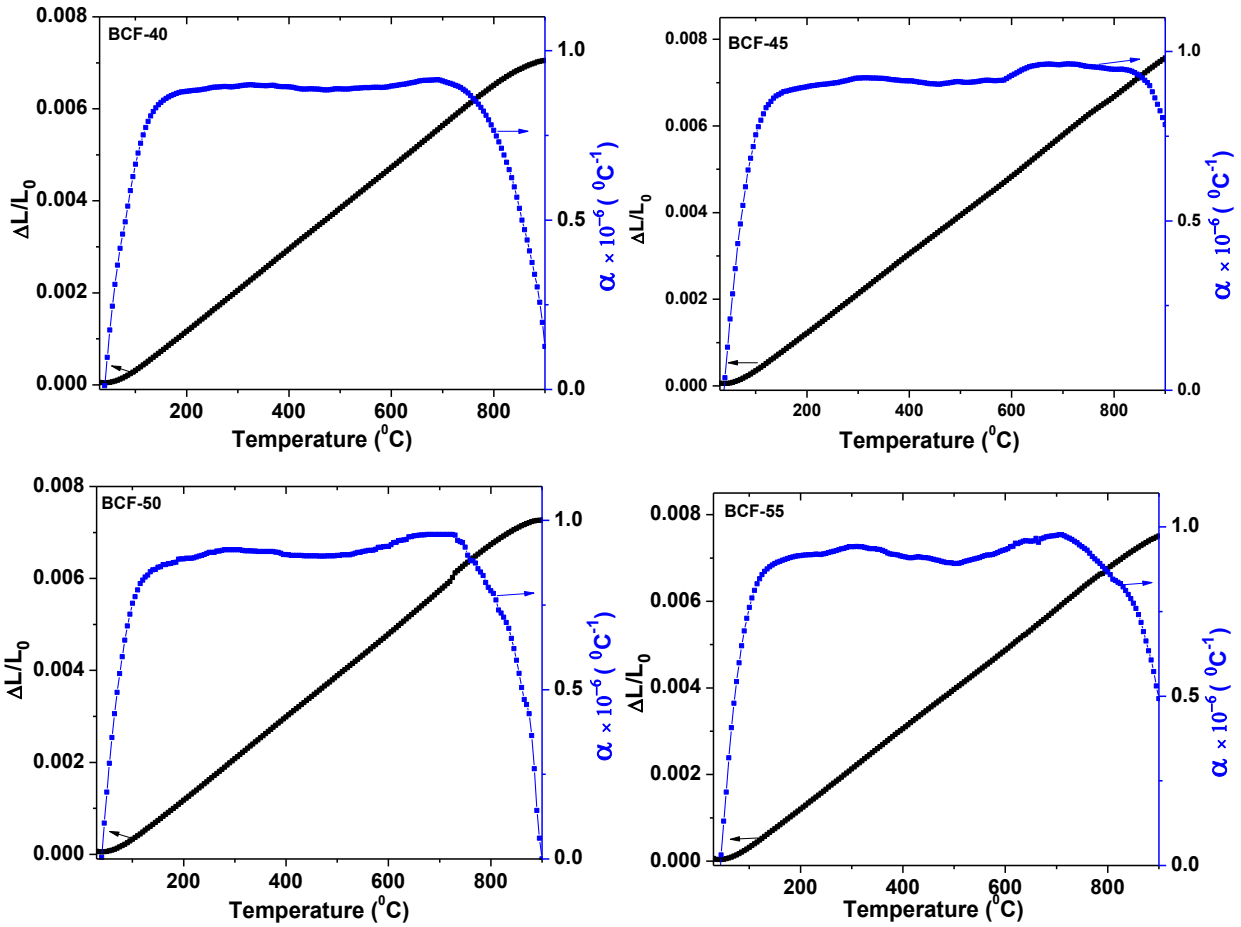

Figure 4.24: Thermal expansion curves of $Bi_{1-x}Ca_xFeO_3$ ($0.40 \leq x \leq 0.55$).

The technical alpha curves both the systems show two broad humps ~ 320 and 650 ˚C for all the samples. These humps can be associated with phase transition as has also been observed in DTA curves. From the results of thermal expansion measurements, it is apparent that with the increase of substituents concentration, the onset temperature decreases at which oxygen loss become significant due to that TEC increases. This may be due to enhanced rate of formation of defect complexes with increasing Sr content [73]. This is also supported by the TGA curve which clearly shows a weight change above 600 °C. The TEC values of BSF system are more as compared to BCF system. Different ionic radii of substituents can be the reason for this variation.

Table 4.11: Thermal expansion coefficient of $Bi_{1-x}A_xFeO_3$ (A=Sr, Ca; $0.40 \leq x \leq 0.55$).

Sample Label	Thermal expansion coefficient ($\times 10^{-6}$ °C^{-1})	
	100 °C ≤ T ≤ 600 °C	**600 °C ≤ T ≤ 800 °C**
BSF-40	9.1	9.7
BSF-45	9.2	9.9
BSF-50	9.2	10.1
BSF-55	8.9	9.8
BCF-40	8.8	8.9
BCF-45	9.0	9.2
BCF-50	9.0	9.34
BCF-55	9.1	9.42

4.2.10 Electrical conductivity

Impedance spectroscopy was used to analyze the conductivity behavior of the samples. The different cole-cole plots were fitted by using different combinations of circuit $R_s(R_iCPE_i)$ for grains, grain boundary and electrode contribution. Figure 4.25 and 4.26 shows the cole-cole plot of the BSF and BCF, at two different temperatures, as representative curves. The cole-cole plot at different temperatures can be fitted by using a combination of $R_s(R_gCPE_g)(R_{gb}CPE_{gb})(R_eCPE)$ circuits, where, (R_gCPE_g) corresponds to grain, $(R_{gb}CPE_{gb})$ to grain boundary and (R_eCPE) to electrode contribution. The differentiation between the three semicircles was made on the basis of their capacitance values. The capacitance of high frequency semicircle is 10^{-11} F which is in the range of grain or bulk contribution. The capacitance of second semicircle is 10^{-9} F, two orders higher than that of bulk contribution. So, it can be assigned to the grain boundary. For low frequency semicircle, the capacitance value is in the range of 10^{-3}-10^{-5} F which is the typical response of electrode effect.

The Arrhenius plots ($ln\ \sigma T$ *vs* $1000/T$) for all samples are given in figure 4.27. For BSF system, the conductivity increases with increase in substituent concentration up to BSF-50 and after that decreases for BSF-55. The decrease for BSF-55 can be due to the ordering of oxygen vacancies in this particular system as discussed in XRD section. For BCF system, the trend in conductivity is same as that of BSF where it firstly increases up to BCF-50 and after that decreases. However, the decrease in conductivity is due to the presence of secondary phase in this system. The increase of conductivity with substituent concentration (Sr^{2+}/Ca^{2+}) is mainly associated with the generation of more oxygen vacancies and Fe^{4+}.

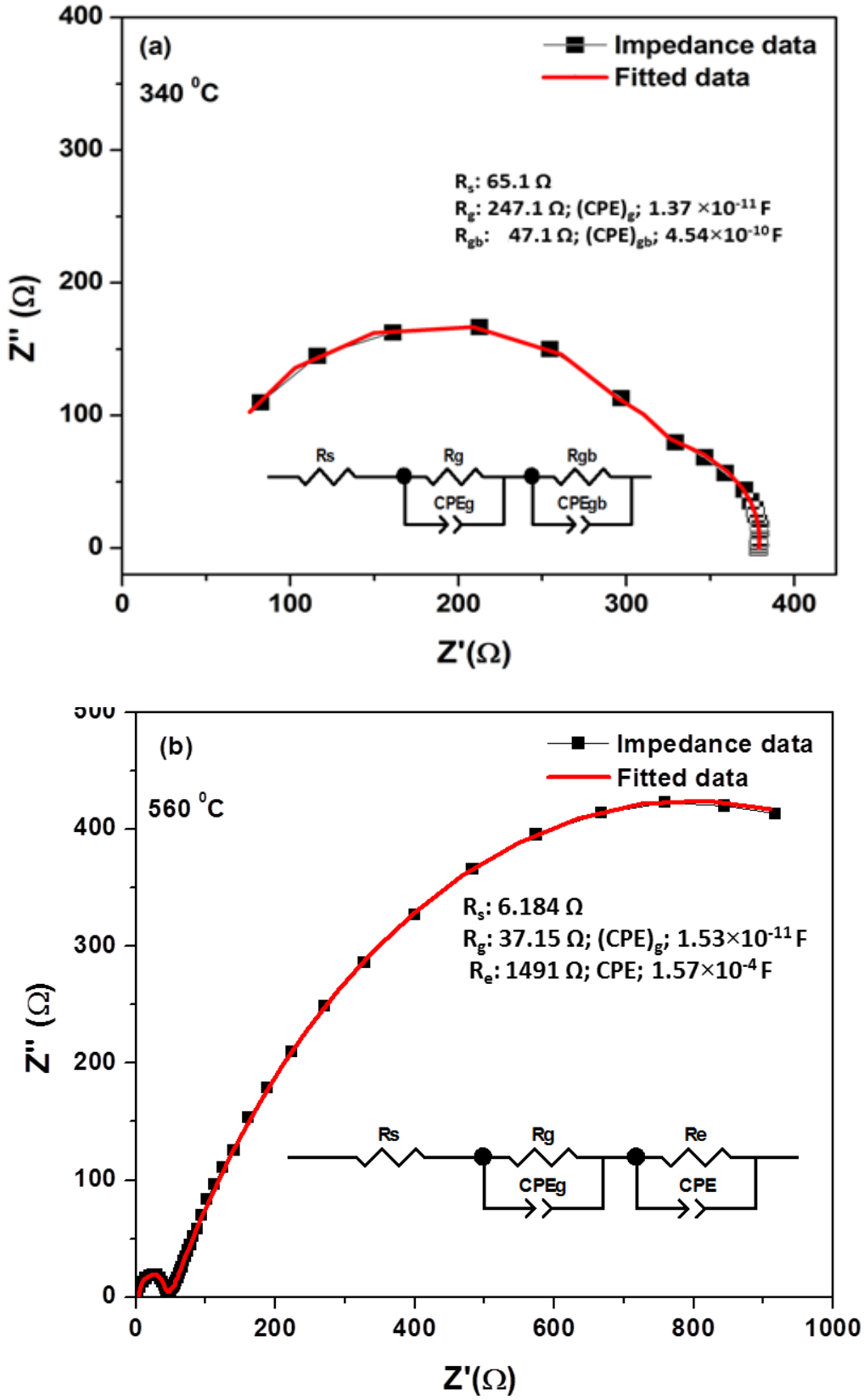

Figure 4.25: Cole – Cole plot of $Bi_{0.50}Sr_{0.50}FeO_3$ at (a) 340 °C (b) 560 °C.

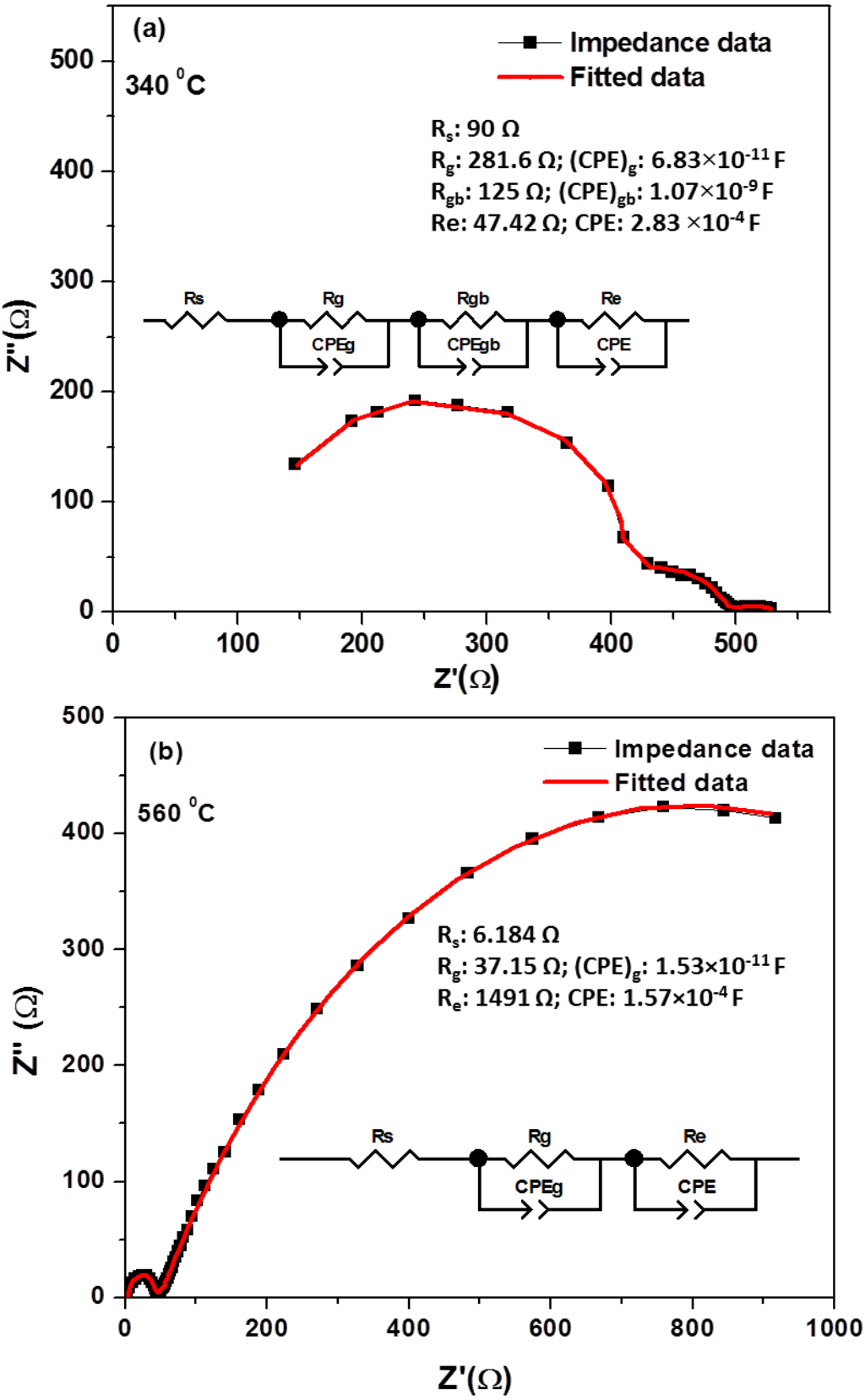

Figure 4.26: Cole – Cole plot of $Bi_{0.50}Ca_{0.50}FeO_3$ at (a) 340 °C (b) 560 °C.

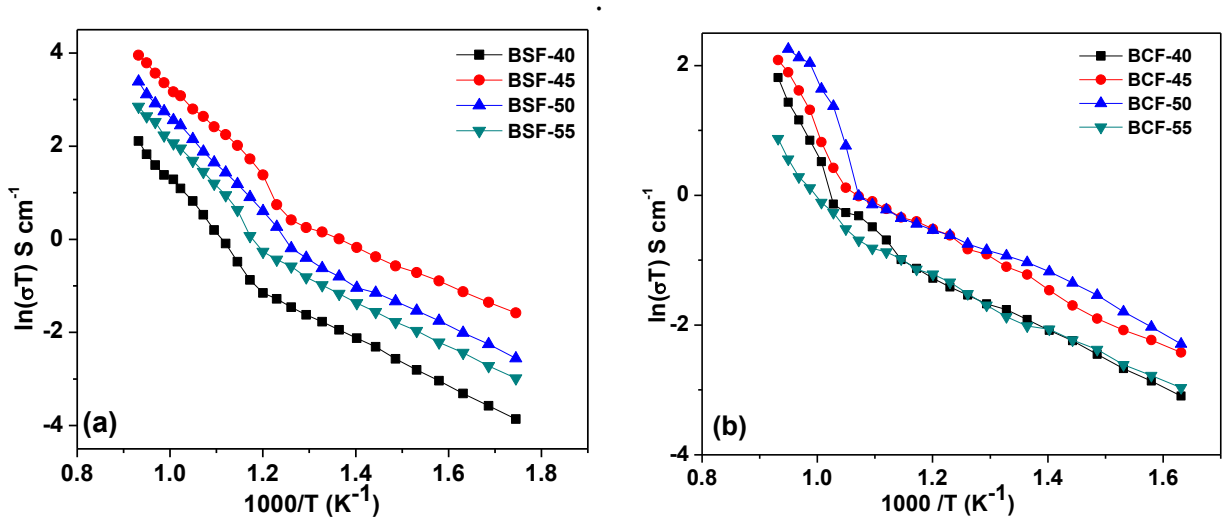

Figure 4.27: Arrhenius curves of (a) $Bi_{1-x}Sr_xFeO_3$ (b) $Bi_{1-x}Ca_xFeO_3$; $0.40 \leq x \leq 0.55$.

Table 4.12: Activation energy for $Bi_{1-x}A_xFeO_3$ (A= Sr, Ca; $0.40 \leq x \leq 0.55$).

Sample Label	Activation Energy, E_a (eV)	
	300 °C ≤ T ≤ 600 °C	600 °C ≤ T ≤ 800 °C
BSF-40	0.43	0.86
BSF-45	0.39	0.82
BSF-50	0.32	0.76
BSF-55	0.45	0.92
BCF-40	0.40	1.64
BCF-45	0.37	1.47
BCF-50	0.34	1.37
BCF-55	0.36	1.42

The Arrhenius plots of all the samples can be divided into two main linear regions which can be easily distinguished on the basis of different activation energies. The discontinuity in these curves can be attributed to the small change in oxygen stoichiometry with rise in temperature as discussed in TGA/ DTA. These spectra are also fitted with the Arrhenius equation and activation energies are calculated for all the samples. The results are given in table 4.12. The low activation energy in the temperature range of 300- 600 °C clearly indicates that conductivity in this region is mainly due to the hopping of small p-type polarons which are associated with the generation of Fe^{4+} in the system. [75, 76]. Maso *et al.* [77] have reported that 3% Fe^{4+} content is sufficient to increase the electronic conductivity in the doped $BiFeO_3$ system. The increase in conductivity at higher temperature around 600 °C is due to the creation of more oxygen vacancies. In TGA results it has also been observed that these oxygen vacancies get annihilated in the presence of air. However, the weight gain is very small. Moreover, the conductivity experiment is performed in the normal atmospheric

pressure, so, it is quite possible that the annihilation of oxygen vacancies will be very low. The effect of conductivity thus can be neglected due to the annihilation of oxygen vacancies. The BSF system exhibits high conductivity as compared to BCF system. This can be attributed to the higher symmetry and larger specific free volume of the BSF system. Even it is also reported in literature that trapping of holes by Ca'_{Bi} in BCF system also decreases the conductivity and increase the activation energy [77]. It is also well supported by the activation energy values of BCF system which are higher than BSF system.

It can be concluded in the present series that substitution of Sr^{2+}/Ca^{2+} has transformed the crystal structure into tetragonal structure as compared to rhombohedral structure of undoped $BiFeO_3$. The maximum conductivity is observed for BSF sample i.e. 3.42×10^{-2} S cm^{-1}.

4.3 $Bi_{1-x}A_xYO_3$ (A=Sr, Ca; $0.0 \leq x \leq 0.20$)

Y_2O_3 being extensively used element in SOFC as solid electrolyte (YSZ) and anode (Ni-YSZ) has been explored as cathode material in this series. In literature, it is reported that undoped and doped $LaYO_3$ compounds are oxygen ion conductor and also p-type semiconductors depending upon the variation of partial pressure of oxygen [78, 79]. So, the effect of different substituents Sr^{2+}/ Ca^{2+} in $BiYO_3$ have been studied for their different properties. The samples of $Bi_{1-x}A_xYO_3$ were first synthesized with x=0.40 and 0.50. However, substitution leads to the formation of secondary phase so, it was decided to work with lower concentrations of Sr^{2+}/ Ca^{2+} substitution.

4.3.1 Physical properties

The density of all the $Bi_{1-x}A_xYO_3$ (A=Sr, Ca; $0.0 \leq x \leq 0.20$) samples was measured by Archimedes principle. As secondary phases are present in these samples (discussed in next section), the additive mixture rule was used to calculate the theoretical density. All the calculated values are given in table 4.13. The specific free volume and tolerance factor was calculated only for x=0.0 and 0.05 compositions as they form single phase with perovskite structure. For the calculations of doped samples, it was presumed that only oxygen vacancies are the prominent defects Y does not exhibit different oxidation state. The oxygen non-stoichiometry is calculated according to the normal charge compensation equation which is also listed in table 4.13. The tolerance factor and specific free volume of the Sr^{2+} doped system are higher than that of Ca^{2+} doped systems as described earlier.

Table 4.13: Composition along with sample label, density, tolerance factor and specific free volume of $Bi_{1-x}A_xYO_3$ (A=Sr, Ca; 0.0≤x≤0.20).

Composition	Sample Label	Density			Tolerance factor	Specific free volume
		Theoretical (d_{th}) (g cm^{-3})	Calculated (d) (g cm^{-3})	(d/d_{th})%		
$BiYO_3$	BYO	7.51	7.06	94.2	0.801	0.400
$Bi_{0.95}Sr_{0.05}YO_3$	BSY-05	7.05	6.69	95.1	0.790	0.391
$Bi_{0.90}Sr_{0.10}YO_3$	BSY-10	6.66	6.02	90.5	-	-
$Bi_{0.85}Sr_{0.15}YO_3$	BSY-15	6.51	5.84	89.7	-	-
$Bi_{0.80}Sr_{0.20}YO_3$	BSY-20	6.45	5.92	91.7	-	-
$Bi_{0.95}Ca_{0.05}YO_3$	BCY-05	7.00	6.57	93.9	0.782	0.383
$Bi_{0.90}Ca_{0.10}YO_3$	BCY-10	7.24	6.64	91.6	-	-
$Bi_{0.85}Ca_{0.15}YO_3$	BCY-15	7.21	6.48	89.9	-	-
$Bi_{0.80}Ca_{0.20}YO_3$	BCY-20	7.17	6.39	89.02	-	-

4.3.2 X-ray diffraction

The X-ray diffraction patterns of $Bi_{1-x}Sr_xYO_3$ ($0.0 \leq x \leq 0.20$) are shown in figure 4.28. The XRD pattern clearly indicates that only sample with x=0.0 and 0.05 are single phase. These samples have cubic structure. So, it can be said that solubility of Sr^{2+} is only up to 5 mol% in

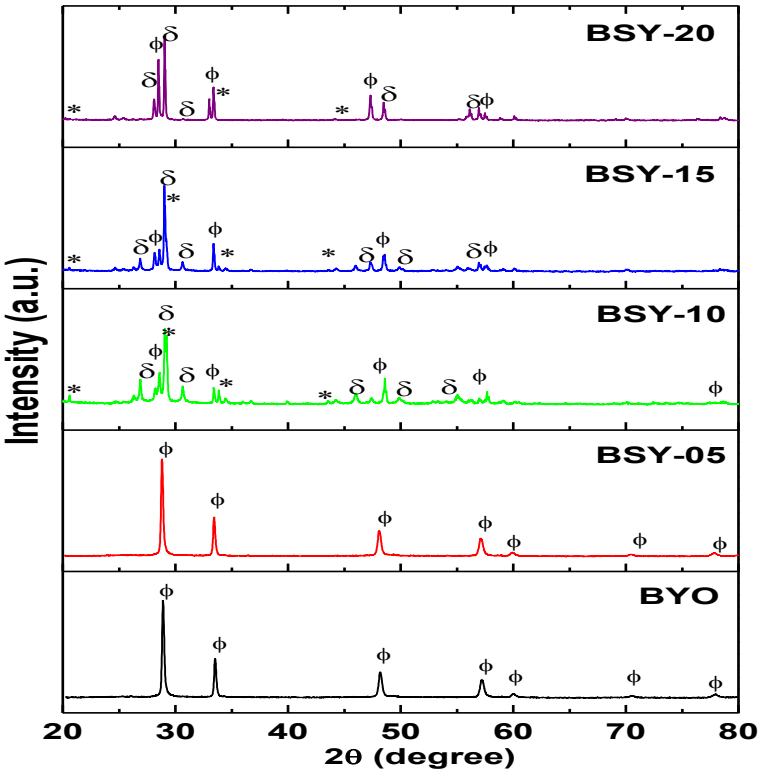

Figure 4.28: X-ray diffractions pattern of $Bi_{1-x}Sr_xYO_3$ (0.0≤x≤0.20); ϕ -$BiYO_3$, δ -$Sr_2Bi_2O_6$, *-Y_2O_3.

$BiYO_3$ lattice. For higher concentration x>0.05, the secondary phase starts appearing. The crystalline phases are indexed as $BiYO_3$ (ICDD-00-027-1047), $Sr_2Bi_2O_5$ (ICDD-01-089-1552) and Y_2O_3 (ICDD-01-073-1334). The volume fraction of Y_2O_3 and $Sr_2Bi_2O_5$ phases increases with the increase in substituent (Sr^{2+}) concentration which is also given in table 4.14. As solubility of Sr in $BiYO_3$ is quite low so, for higher SrO concentration, a small portion of Sr gets dissolved in the matrix of $BiYO_3$ and rest of it combines with some bismuth and forms the secondary phase $Sr_2Bi_2O_5$. The probability of formation of $Sr_2Bi_2O_5$ is quite high as compared to $(BiSr)YO_3$ for high concentration of Sr due to the low solubility of Sr in $BiYO_3$. The lattice parameters of only undoped and doped $Bi_{0.95}Sr_{0.05}YO_3$ were calculated and are tabulated in table 4.14. With the substitution of Sr^{2+} in $BiYO_3$, there is an increase in the lattice parameters. This can be attributed to the larger ionic radii of Sr^{2+} as compared to Bi^{3+}. The oxygen vacancies will also be generated in this system to maintain the charge imbalance created after substitution of Sr^{2+} in place of Bi^{3+}. The number of oxygen vacancies created in this system is quite low as small amount of Bi^{3+} is replaced by the Sr^{2+}.

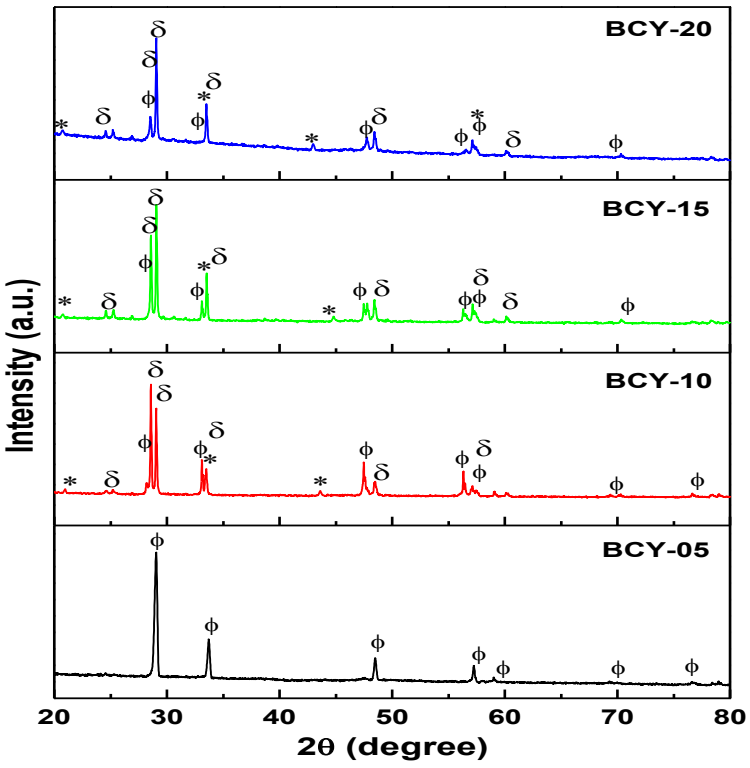

Figure 4.29: X-ray diffraction patterns of $Bi_{1-x}Ca_xYO_3$ ($0.0 \leq x \leq 0.20$); ϕ-$BiYO_3$, δ-$Ca_5Bi_{14}O_{26}$, *-Y_2O_3.

The XRD patterns of $Bi_{1-x}Ca_xYO_3$ ($0.0 \leq x \leq 0.20$) are shown in figure 4.29. The BCY-5 is single phase with cubic structure and rest of all compositions has secondary phases. These

secondary phases can be indexed as $BiYO_3$ (ICDD-00-027-1047), $Ca_5Bi_{14}O_{26}$ (ICDD-00-042-1460) and Y_2O_3 (ICDD-01-073-1334). The volume fraction of these phases is given in table 4.14. With increasing CaO content, secondary phases start increasing at the cost of $BiYO_3$ phase. As discussed in Sr^{2+} substituted system, the probability of formation of other phases is high for higher Ca^{2+} concentration in the system due to the low solubility of Ca^{2+} in $BiYO_3$. The lattice parameters of BCY-5 are smaller than that of undoped BYO sample due to the smaller ionic radii of Ca^{2+} as compared to Bi^{3+}. Smaller ionic radii of Ca^{2+} will generate compressive strain in the lattice and decrease the unit cell volume.

Table 4.14: Volume fraction of different phases present in $Bi_{1-x}A_xYO_3$ (A=Sr, Ca; $0.0 \leq x \leq 0.20$).

Sample Label	**Volume fraction of different phases (%)**				
	$BiYO_3$	**$Bi_2Sr_2O_5$**	**$Bi_{14}Ca_5O_{26}$**	**Y_2O_3**	**Lattice parameters**
BYO	100	-	-	-	5.4280 Å
BSY-05	100	-	-	-	5.4394 Å
BSY-10	25	62	-	13	-
BSY-15	15	68	-	17	-
BSY-20	10	72	-	18	-
BCY-05	100	-	-	-	5.3983 Å
BCY-10	20	-	63	17	-
BCY-15	12	-	69	19	-
BCY-20	7	-	72	21	-

4.3.3 Analysis of Raman spectra

The Raman spectra of selected samples were recorded to confirm the structure of the doped $BiYO_3$. The spectra of samples BSY-5, BSY-10 and BCY-10 are shown in figure 4.30. The Raman spectrum of BSY-5 does not exhibit any peak because of its cubic structure as the optical bands for cubic structure are classified as $\Gamma = 3F_{1u}(IR) + F_{2u}$. Where the three F_{1u} species are allowed only in infrared region and other F_{2u} is forbidden for both infrared and Raman scattering [80]. This is the reason that cubic perovskite systems do not exhibit any band in Raman spectra. BSY-10 sample shows three bands around 83, 100 and 633 cm^{-1}, respectively. Whereas, in BCY-10 sample, the bands are observed around 363, 306 and 631 cm^{-1}, respectively. All these active bands can be indexed to the Bi-O stretching and O-Bi-O bending modes [81]. The presence of these bands also indicates towards the formation of bismuth rich phase in the present studied samples. No band was observed for Y_2O_3 in all the Raman spectra as it also has the cubic structure.

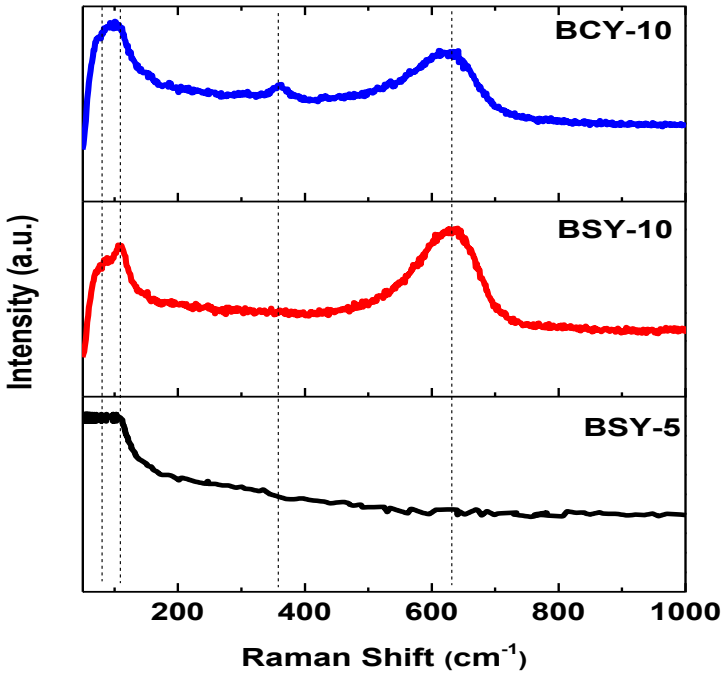

Figure 4.30: Raman spectra of BSY-05, BSY-10 and BCY-10.

4.3.4 Fourier transform infrared analysis

Figure 4.31 (a) represents the FT-IR spectra $Bi_{1-x}Sr_xYO_3$ ($0.0 \leq x \leq 0.20$) system. The bands around 500 and 600 cm^{-1} are observed in BYO and BSY-05. Additional bands around 560, 460, 440 and 860 cm^{-1} start appearing for samples having higher concentration of Sr^{2+} ($x>0.05$). Most of the bands can be indexed to stretching and bending vibrations of Bi-O bond. The band predominantly observed at 620 cm^{-1} in all the samples is due to Bi–O–Bi vibrations of [BiO_6] octahedral units. The bands around 460, 500 and 560, 860 cm^{-1} are also assigned to the stretching vibrations of Bi–O bonds in distorted BiO_6 octahedral units over which the longitudinal bands of Y-O are superimposed [82, 83].

The FT-IR spectra of $Bi_{1-x}Ca_xYO_3$ ($0.05 \leq x \leq 0.20$) samples are shown in figure 4.31 (b). These samples also exhibit the FT-IR bands around 440, 560 and 610 cm^{-1}, respectively. All the bands can be attributed to the different vibrations of Bi-O bands as discussed in Sr^{2+} substituted samples. The bands around 460, 500 and 560 cm^{-1} shift to lower number side whereas one around 610 cm^{-1} shifts to higher wavenumber side with increase in substituent concentration in both the BSY and BCY systems. This shift can be due to the different sizes and masses of the Bi^{3+}, Sr^{2+} and Ca^{2+} cations. The major difference between the BCY and BSY spectra is the number of bands present in both the samples. The BSY samples show

some additional peaks after 0.05 concentration of Sr^{2+}. Whereas, these bands are same throughout for every composition in Ca^{2+} substituted samples. This variation is because of the fact that difference between the ionic radii of Bi^{3+} (1.17 Å) and Sr^{2+} (1.26 Å) is more as compared to Bi^{3+} and Ca^{2+} (1.12 Å) due to which Sr^{2+} containing systems are more disordered as compared to Ca^{2+} substituted systems. This disordering may be responsible for generation of more number of bands in these samples.

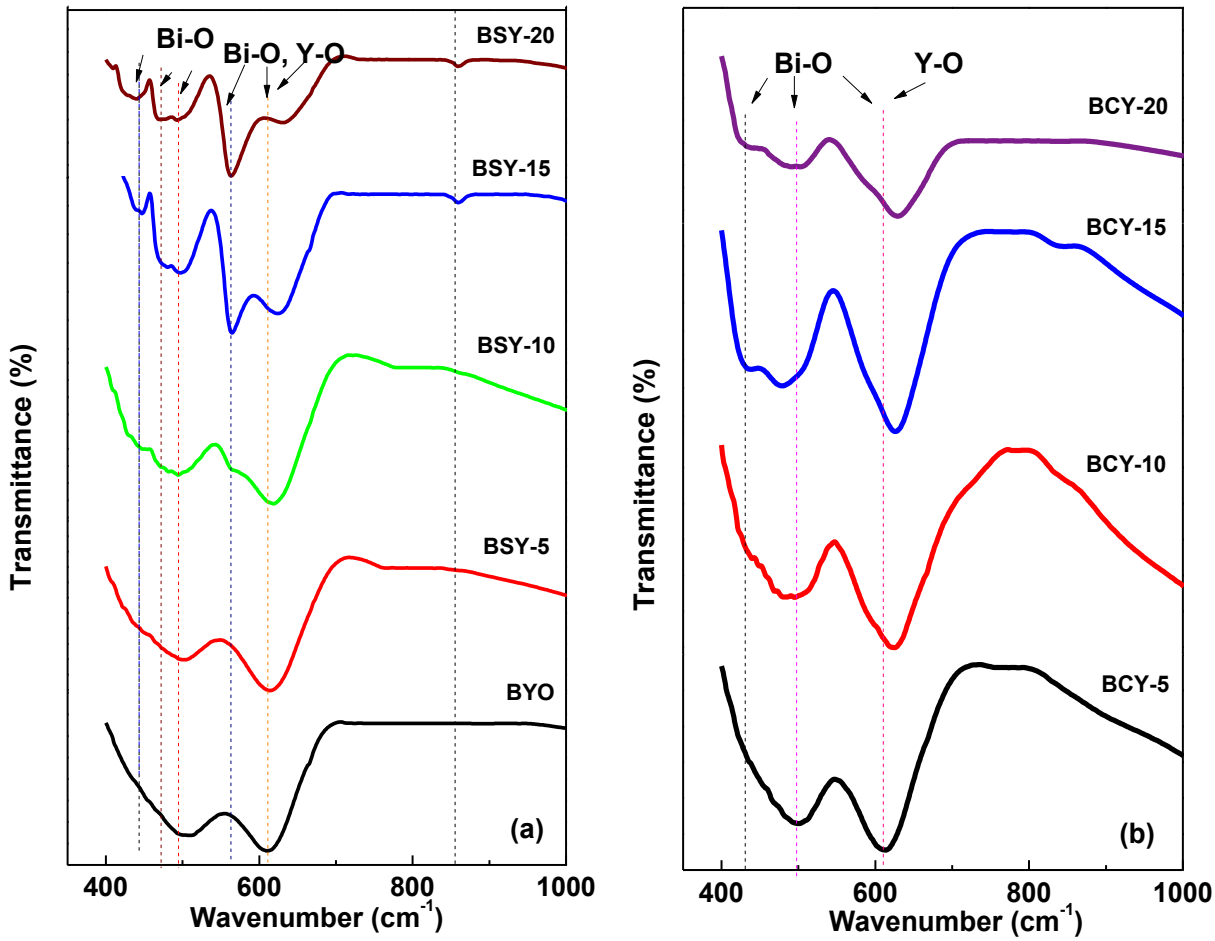

Figure 4.31: FT-IR spectra of (a) $Bi_{1-x}Sr_xYO_3$ (b) $Bi_{1-x}Ca_xYO_3$; $0.0 \leq x \leq 0.20$.

4.3.5 Microstructural study

The scanning electron micrographs of the undoped BYO, BSY-05 and BSY-10 are shown in figure 4.32 (a). In BYO, grains are equiaxed and uniform in size. Micrograph of BSY-05 clearly indicates that Sr^{2+} substitution has led to decrease in grain size as addition of alkaline earth metals suppresses the grain growth. The grains are of nearly uniform size. The elongated porosity is observed because of the solidification shrinkage. For BSY-10, the grains are non-uniform with considerable porosity. The non-uniformity is due to the presence

of secondary phases in this particular sample. The grains are not much pronounced but have considerable variation in grain size. Moreover some of the grains are very small as compared to BYO and BSY-05 samples. As different phases are present in this sample, so, it is quite possible that one phase inhibits the growth of other phase or it can be said that one phase grows at the expense of other. This has caused variation in grain size. Because of such transitions in the samples, the porosity has increased. This can be due to the different melting temperature of different phases. The dispersion in grain sizes for all the samples are shown in figure 4.32 (b). Figure 4.33 (a) represents the micrographs of BCY-05 and BCY-10 sample. The grain size variation for all the samples has also been shown in figure 4.33 (b). In BCY-05 micrograph, it is clear that this sample has endured through liquid phase sintering. Due to the liquid phase sintering, the grain size has increased considerably. Apart from substitution, there are other thermodynamic factors which influence the grain size. The grain size decreases with the Ca^{2+} substitution as discussed earlier also. Grain size variation decreases as the substituent concentration increases which is minimum for BCY-20 sample as shown in figure 4.33 (b).

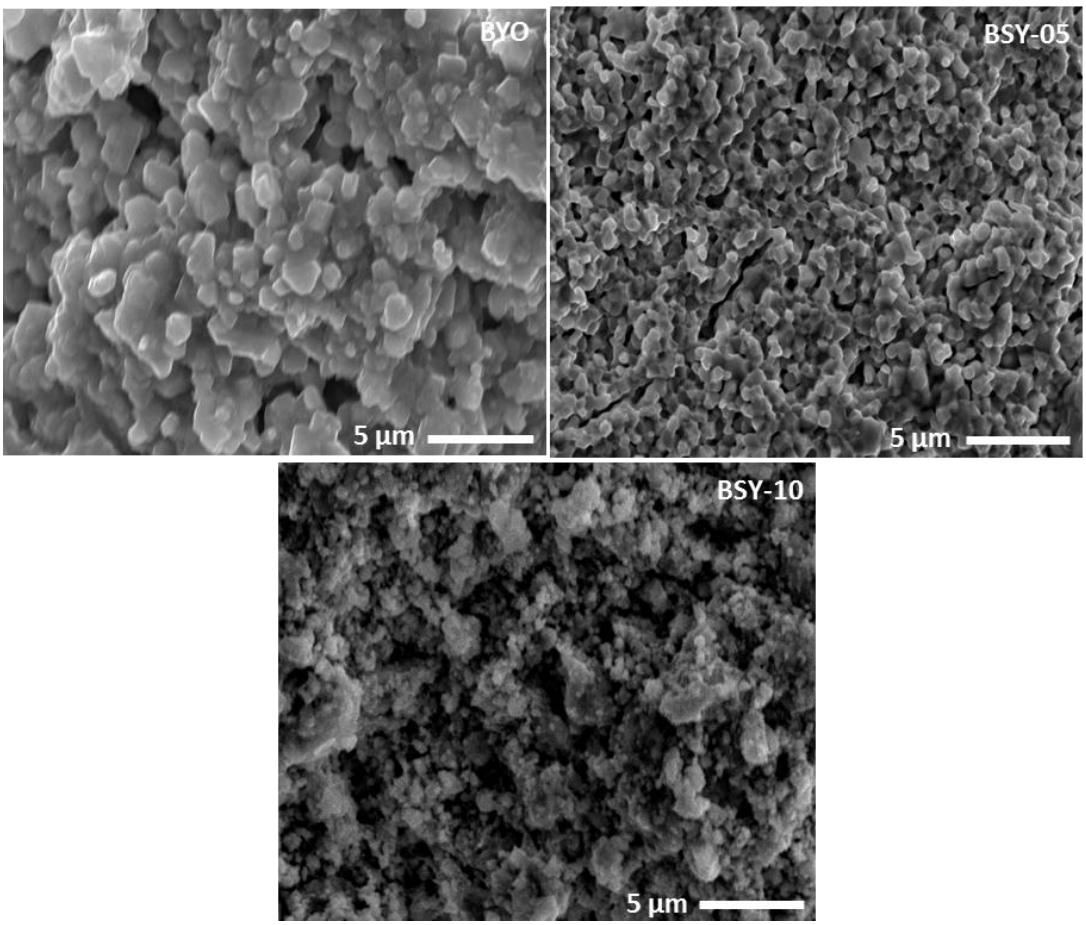

Figure 4.32 (a): SEM micrographs of BYO, BSY-05 and BSY-10.

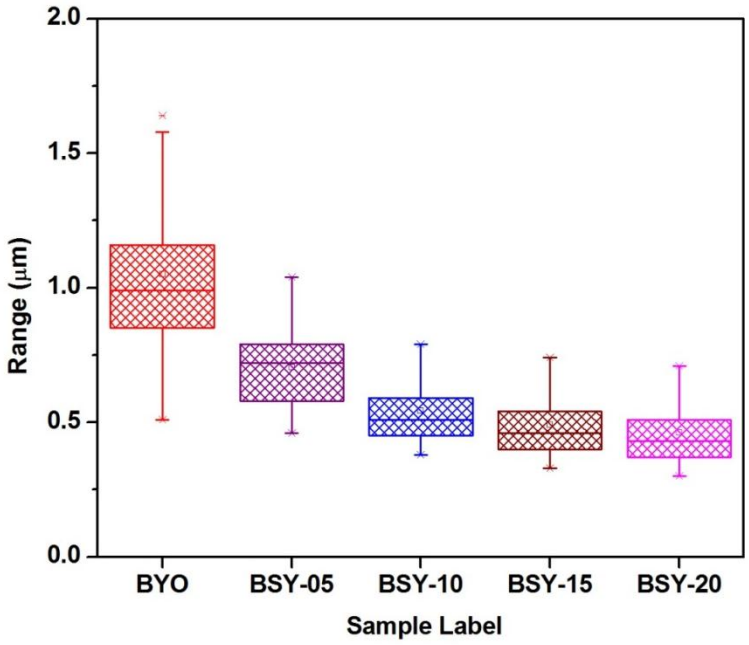

Figure 4.32 (b): Grain size distribution of $Bi_{1-x}Sr_xYO_3$ ($0.0 \leq x \leq 0.20$). The central lines in the boxes represent the mean value.

Such a narrow variation is because of the formation of secondary phases during sintering. Since, the formation of these phases occurs through diffusion which is temperature driven phenomenon so, it generates porosity which leads to lower density and smaller grain size as compared to undoped sample.

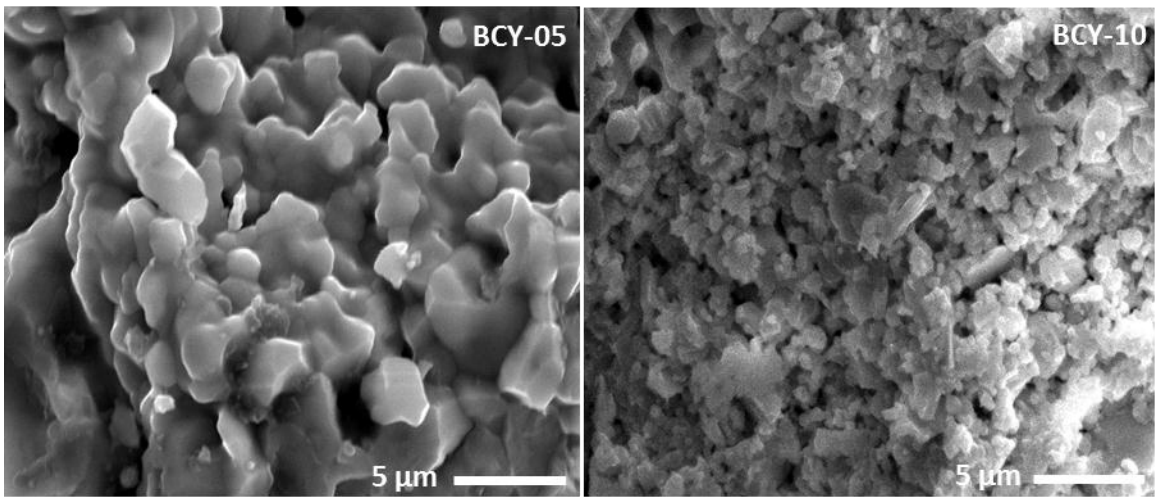

Figure 4.33 (a): SEM micrographs of BCY-05 and BCY-10.

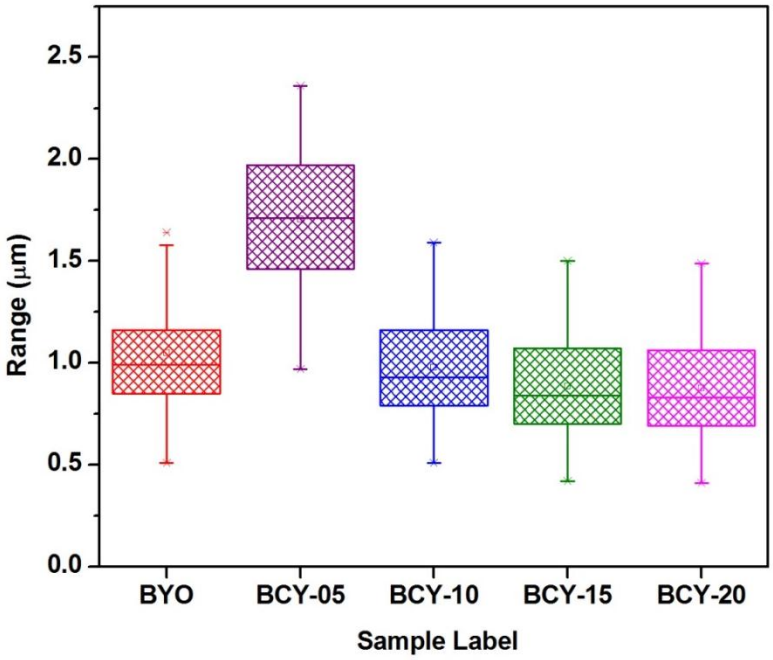

Figure 4.33 (b): Grain size distribution of $Bi_{1-x}Ca_xYO_3$ ($0.0 \leq x \leq 0.20$). The central lines in the boxes represent the mean value.

4.3.6 Thermal properties

The TGA curves of $Bi_{1-x}A_xYO_3$ (A=Sr, Ca; $0.0 \leq x \leq 0.20$) are shown in figure 4.34 and 4.35, respectively. The DTA curves of undoped BYO, BSY and BCY systems are given in inset of their respective TGA curves. No peak has been observed in the DTA curves of any sample which indicates that all the samples do not undergo any phase transition in the studied temperature range. All the undoped, Sr^{2+} and Ca^{2+} substituted samples exhibit weight loss in two steps. First weight loss is up to 200 ˚C which can be attributed to the loss of moisture and water content from the sample. After that there is no weight loss up to 500 ˚C and the curve becomes almost flat. The weight loss above this temperature can be explained on the basis of multiple processes: (1) generation of oxygen vacancies in $BiYO_3$ and Y_2O_3 at high temperatures. (2) Sublimation of bismuth [84, 85]. All the samples almost retrace their behavior in cooling cycles. So, it can be concluded that majority of weight loss is due to the generation of oxygen vacancies at high temperatures [86]. These vacancies again get filled during cooling cycle as the TGA is performed in air.

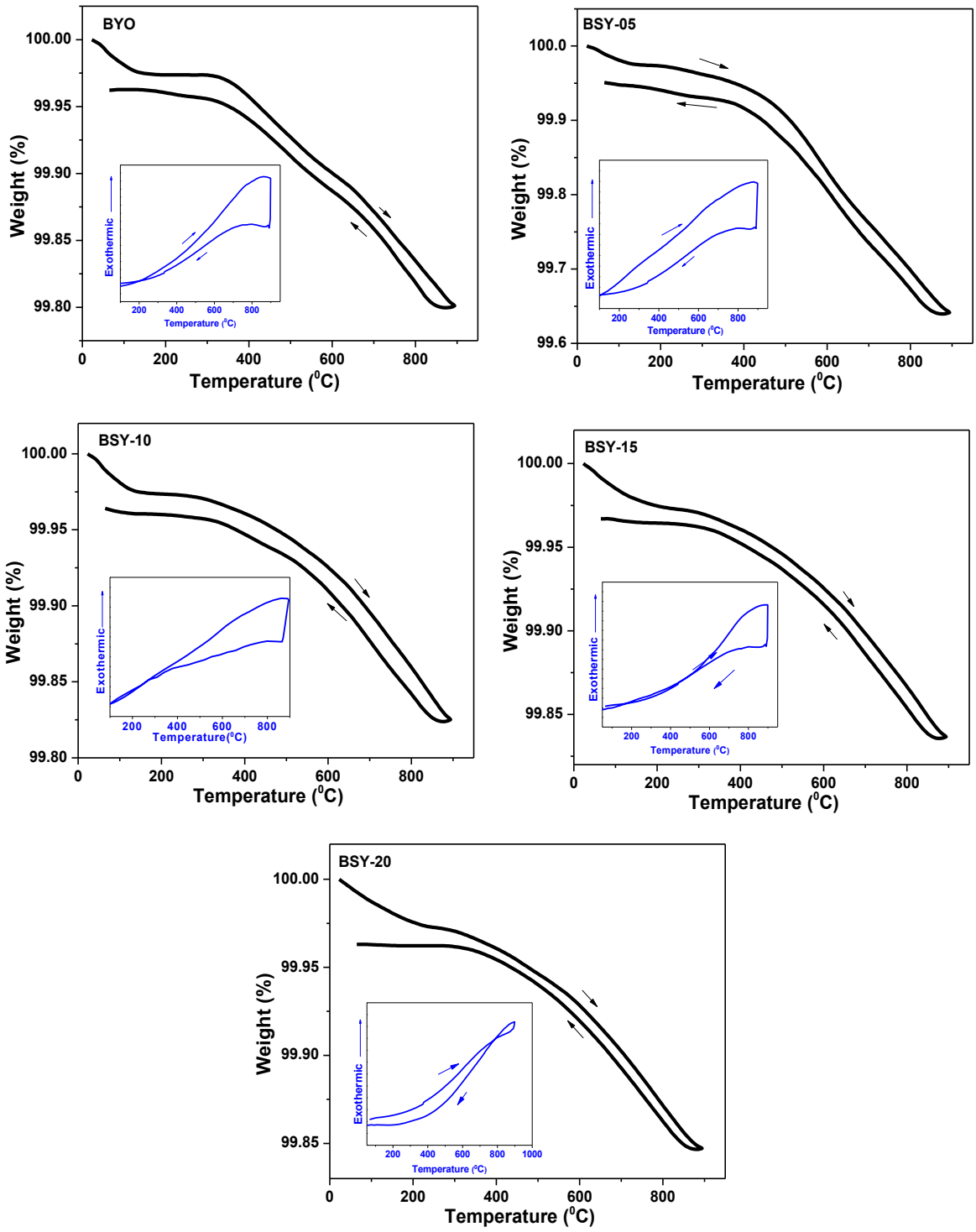

Figure 4.34: DTA/TGA curves of $Bi_{1-x}Sr_xYO_3$ ($0.0 \leq x \leq 0.20$).

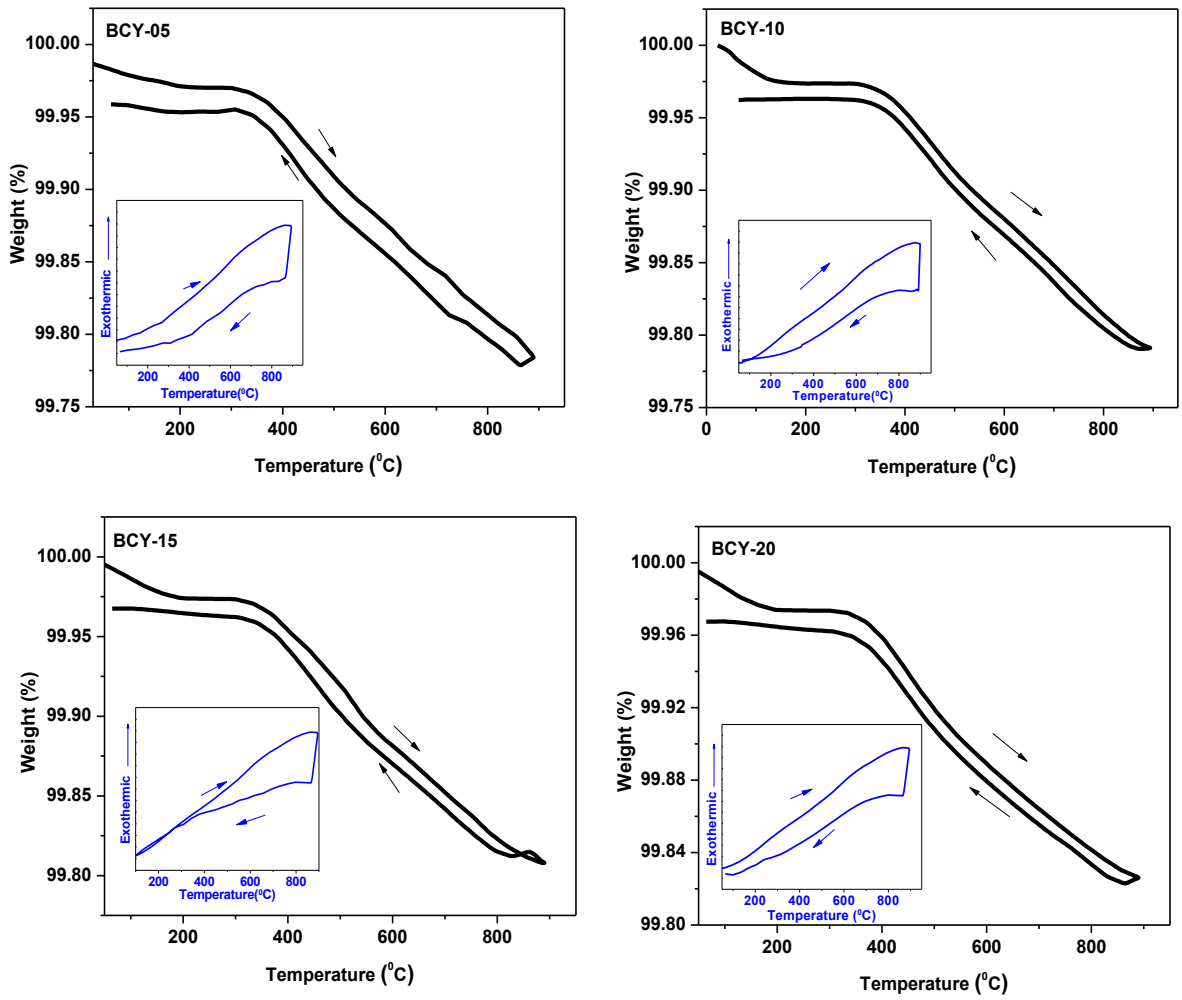

Figure 4.35: DTA/TGA curves of $Bi_{1-x}Ca_xYO_3$ ($0.05 \leq x \leq 0.20$).

The weight loss increases with the increase in substituent concentration up to x=0.05 in both the Sr^{2+} and Ca^{2+} containing systems. After that for higher concentration of Sr^{2+}/Ca^{2+}, the weight loss for all the samples becomes almost same. The higher weight loss observed for substituted samples than undoped samples can be due to the more oxygen vacancies at high temperatures in BSY-05 and BCY-05. The decrease in weight loss after that composition may be due to the presence of more stable secondary phases in the samples.

4.3.7 Thermal expansion coefficient

The physical and technical thermal expansion curves of $Bi_{1-x}A_xYO_3$ (A=Sr, Ca; $0.0 \leq x \leq 0.20$) are shown in figure 4.36 and 4.37, respectively. The calculated values of thermal expansion coefficients for both BSY and BCY systems are given in table 4.15. The thermal expansion coefficient firstly increases with the increase in concentration of the substituent Sr^{2+}/Ca^{2+} up to x=0.05 as compared to undoped samples. This increase can be due to more in

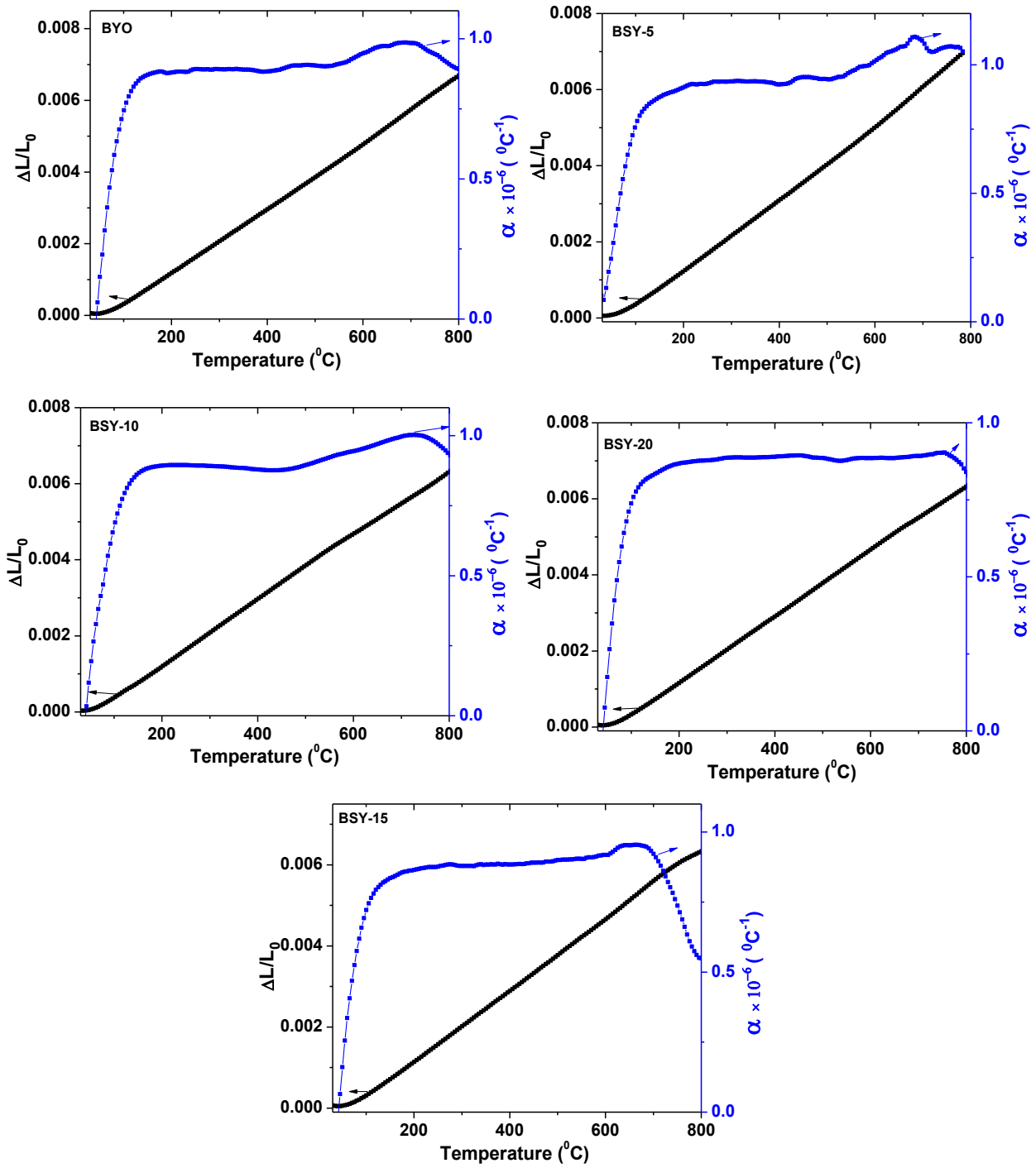

Figure 4.36: TEC curves of $Bi_{1-x}Sr_xYO_3$ ($0.0 \leq x \leq 0.20$).

the substituted samples as compared to undoped BYO. The BSY-05 sample shows drastic increase in TEC as compared to BYO, whereas, this change is very small in BCY-05 sample. As ionic radii difference between Sr^{2+} and Bi^{3+} is larger, this will make potential well more asymmetric and results in high TEC in this sample. Whereas, the substitution of Ca^{2+} will not disturb the potential well so effectively as the ionic radii of both cations Bi^{3+} and Ca^{2+} are

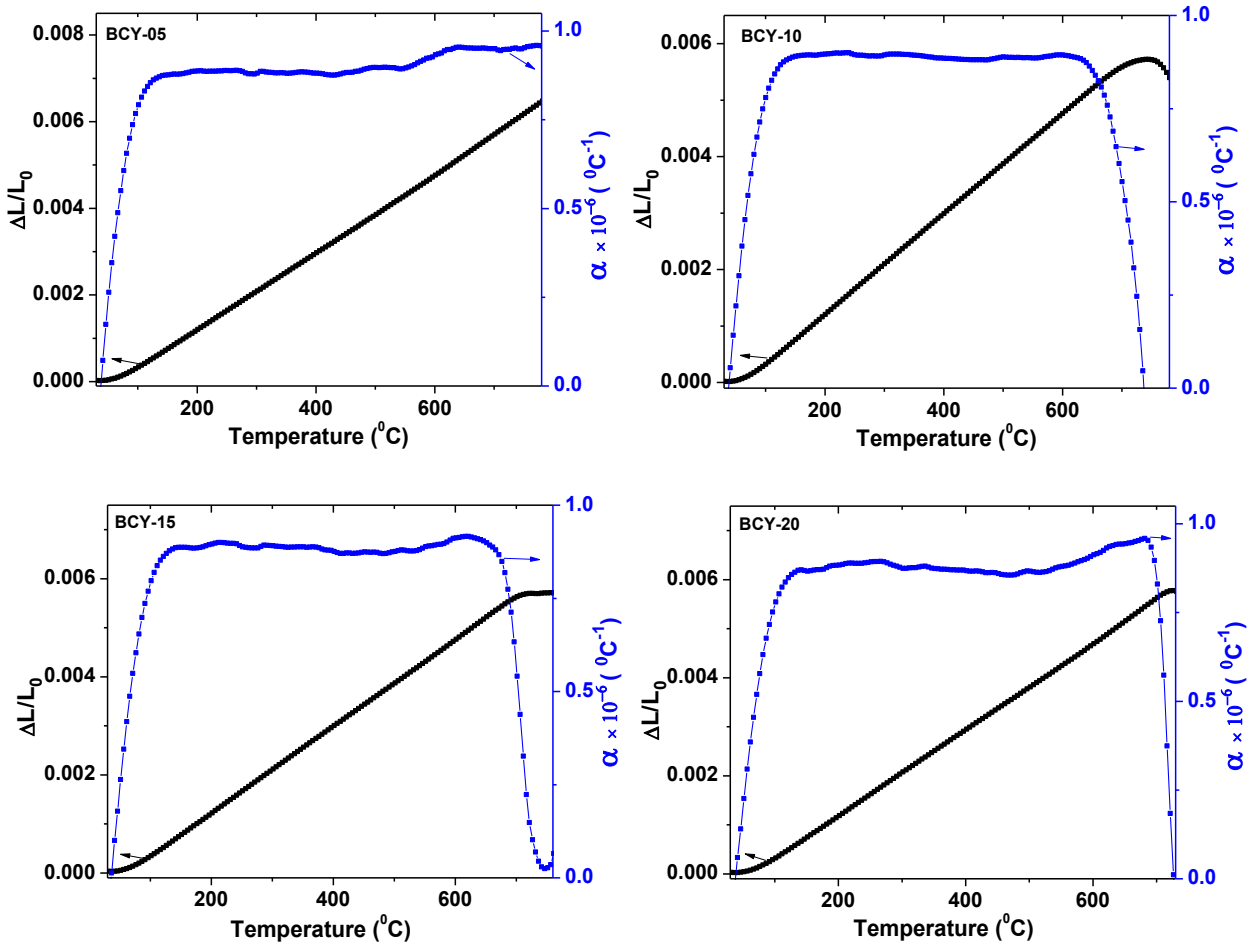

Figure 4.37: TEC curves of $Bi_{1-x}Ca_xYO_3$ ($0.05 \leq x \leq 0.20$).

Table 4.15: Thermal expansion coefficient of $Bi_{1-x}A_xYO_3$ (A=Sr, Ca; $0.0 \leq x \leq 0.20$).

Sample Label	Thermal expansion coefficient ($\times 10^{-6}$ °C^{-1})	
	100 °C ≤ T ≤ 450 °C	**450 °C ≤ T ≤ 750 °C**
BYO	9.14	9.46
BSY-05	9.76	10.06
BSY-10	9.11	9.48
BSY-15	8.99	9.18
BSY-20	8.86	8.85
BCY-05	9.20	9.55
BCY-10	8.93	8.80
BCY-15	8.83	8.32
BCY-20	8.84	8.30

almost same. Thus, the TEC of both the BYO and BCY are almost same. Technical alpha curves of BSY and BCY are also shown with their respective physical thermal expansion curves. The technical alpha curves show increase in TEC after 500 ˚C. This increase can be due to the generation of oxygen vacancies at elevated temperatures as already discussed in

TGA section. Above x=0.05, the increase in technical alpha curves above 450 °C is also small as compared to BSY-05 sample.

4.3.8 Electrical conductivity

The cole -cole plot of BSY-05 and BCY-05 at different temperatures are shown in figure 4.38 and 4.39, respectively. These plots are fitted by using different equivalent circuits depending upon the grain, grain boundary and electrode contribution. The respective equivalent circuits are also shown in their respective figures. The conductivity of each sample was calculated from resistance obtained from the fitting data. The Arrhenius curves of $Bi_{1-x}A_xYO_3$ ($0.0 \leq x \leq 0.20$; A=Sr, Ca) are shown in figure 4.40 (a) and (b), respectively. The activation energies calculated from these plots are given in table 4.16.

In the present studied systems, two different slopes in Arrhenius curve are observed. Since the oxygen vacancies are the most probable defects in these systems, so, the conduction in these systems will be mainly through the hopping of oxygen vacancies. In most of the perovskites, the oxide ions are supposed to hope into adjacent oxygen vacancies along the edge of B-site cations through a triangular face saddle point with two large cations and one small cation at its corners [87]. But practically, grain boundaries and defects play very important role in the conductivity of a particular system. In the present studied systems, it is clear from the cole-cole plot that grain boundary contribution (shown in cole cole plot of 370 ˚C) is prominent at low temperatures. Whereas with increase in temperature, their role diminishes (shown in cole cole plot of 370 ˚C), only bulk contribution is there. This change in contribution from the grain and grain boundary at low and high temperatures also results in decrement in resistance and change in slope in Arrhenius curve. It is also reported that substituent cations Sr^{2+}/Ca^{2+} act as trap centres for the isolated oxygen vacancies. Moreover, they also act as the nucleating sites for the formation of ordered oxygen vacancies clusters and make them unavailable for conduction [88, 89]. At low temperatures, extra energy is dissociate these clusters and to make ions mobile. Thus, activation energy is the sum of dissociation energy and migration energy. Whereas at high temperatures energy is required only for the mobility of these ions so, activation energy only constitutes the migration energy which will be obviously less than the low temperature activation energy [90, 91]. Thus, change in slope in the Arrhenius curves can be due to the combined effect of the intergrain-intragrain and the dissociation- migration energy model.

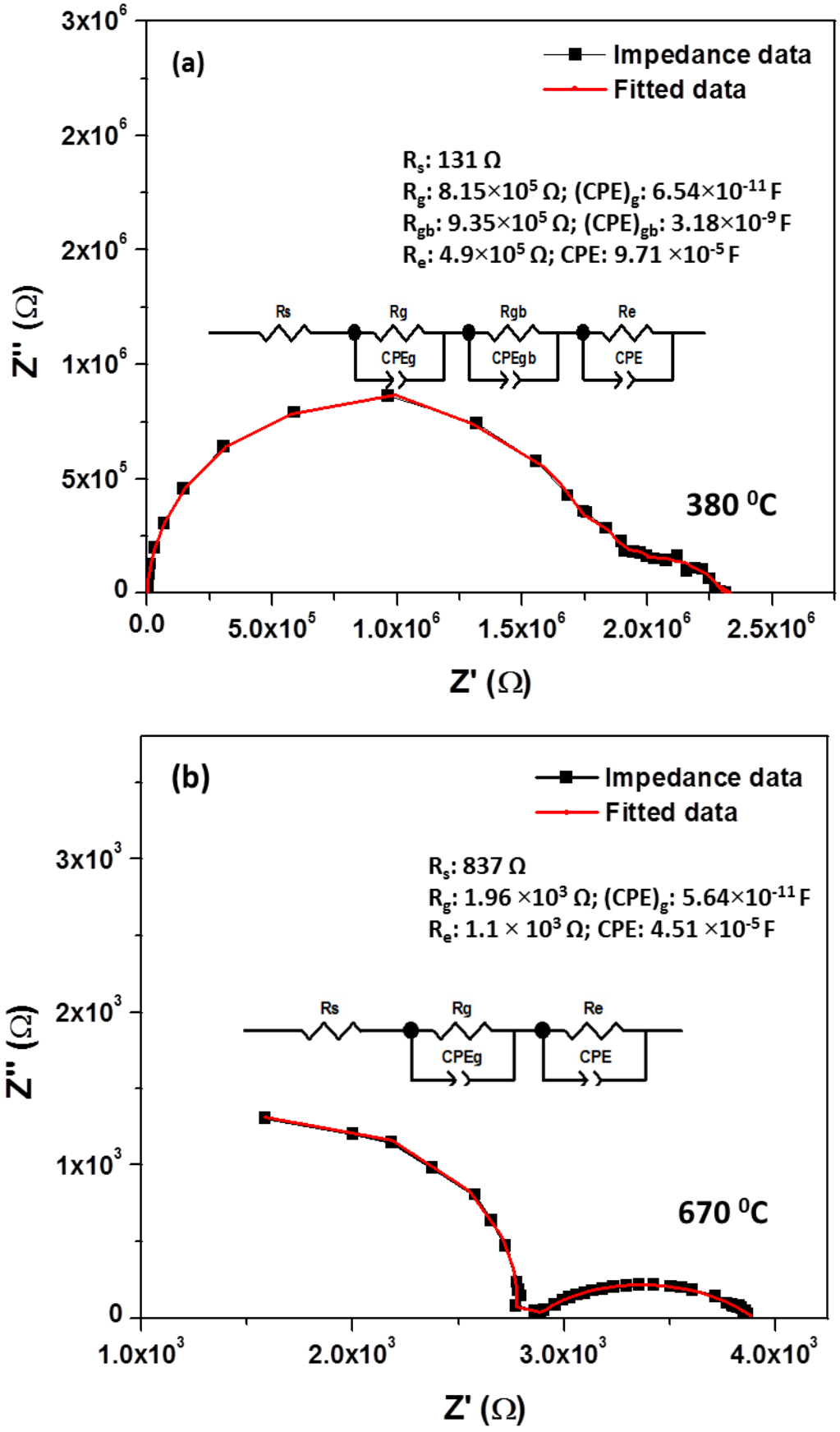

Figure 4.38: Cole - Cole plot of BSY-5 (a) 380 °C (b) 670 °C.

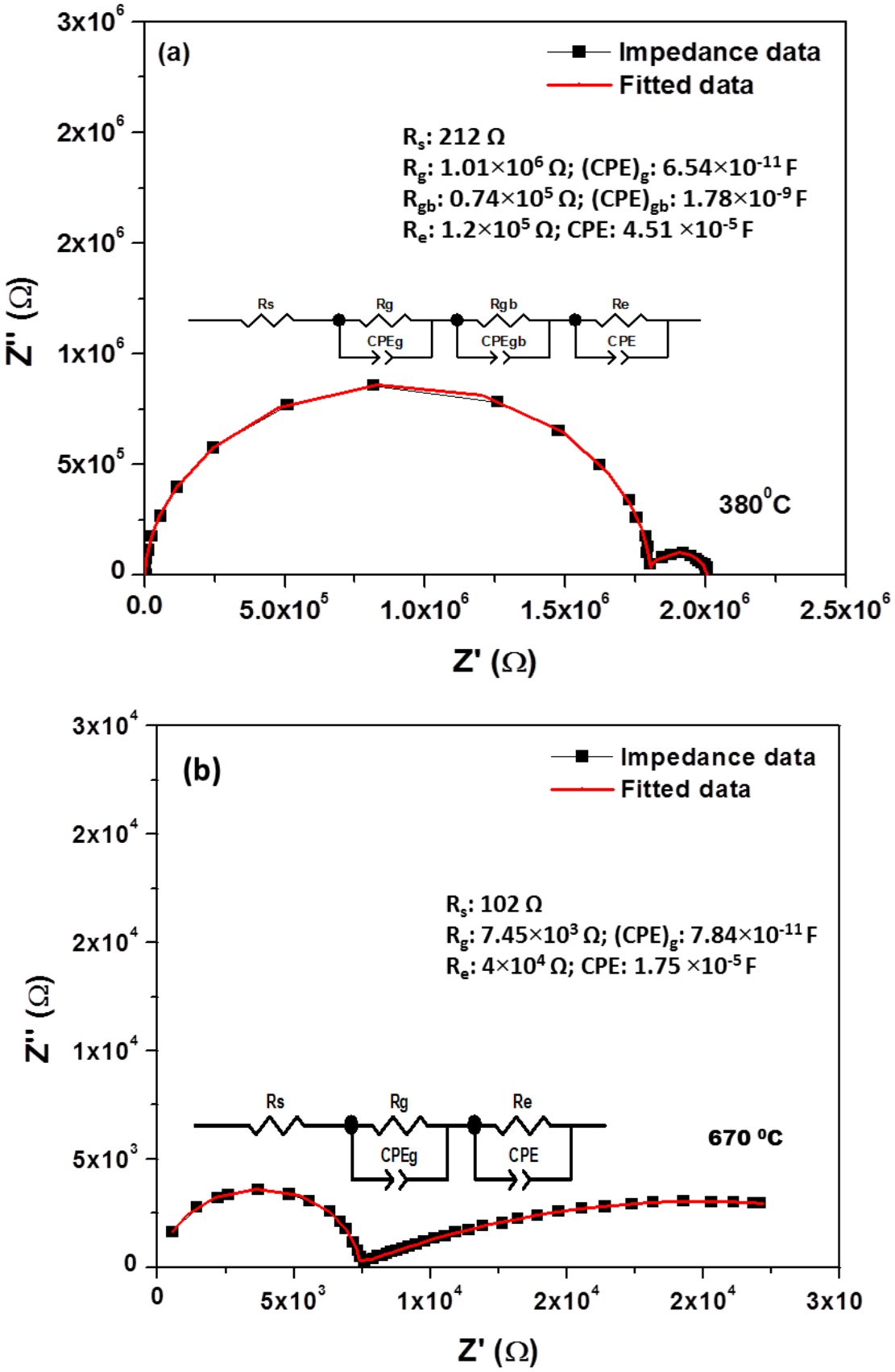

Figure 4.39: Cole - Cole plot of BCY-5 (a) 380 °C (b) 670 °C.

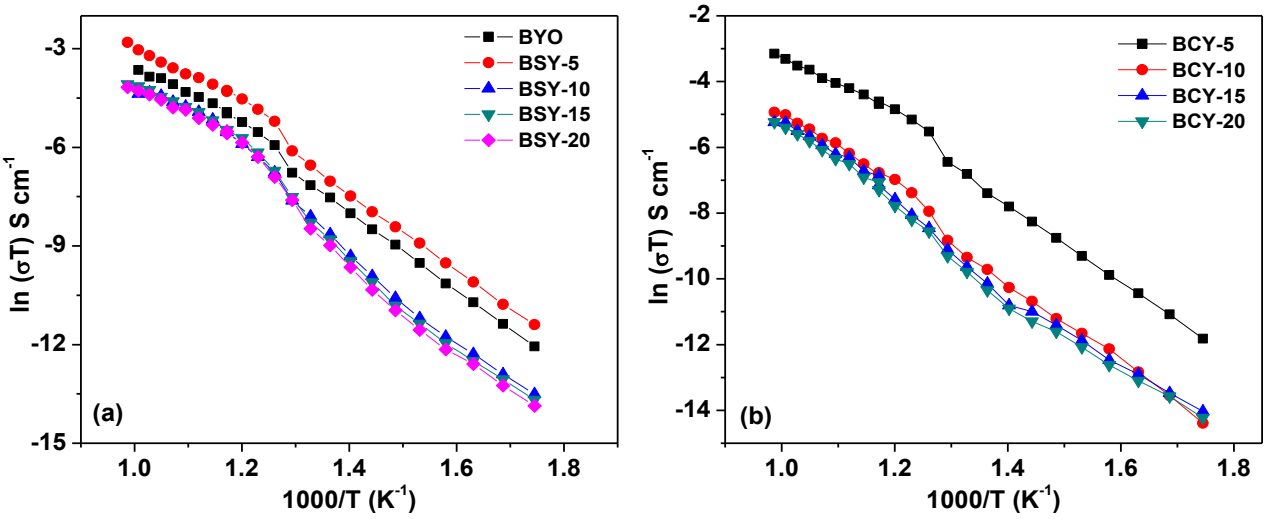

Figure 4.40: Arrhenius curves of (a) $Bi_{1-x}Sr_xYO_3$ (b) $Bi_{1-x}Ca_xYO_3$; $0.05 \leq x \leq 0.20$.

The conductivity increases up to x=0.05 and after that again decreases and becomes almost same for the samples having higher concentrations of substituents in both BSY and BCY system. This is because of the presence of secondary phases for higher concentration in both the systems. As all the secondary phases have low conductivity also act as the scattering centers, so, they will affect the total conductivity of the samples and results in reduction of the conductivity.

Table 4.16: Activation energy for $Bi_{1-x}A_xYO_3$ (A= Sr, Ca; $0.0 \leq x \leq 0.20$).

Sample Label	Activation Energy, E_a (eV)	
	300 °C ≤ T ≤ < 500°C	500 °C ≤ T ≤ 750 °C
BYO	1.06	0.75
BSY-05	0.99	0.70
BSY-10	1.16	0.82
BSY-15	1.16	0.79
BSY-20	1.15	0.78
BCY-05	1.01	0.73
BCY-10	1.02	0.92
BCY-15	1.03	0.93
BCY-20	1.02	0.92

From the above discussion it can be concluded that the solid solubility limit of Sr^{2+} and Ca^{2+} in $Bi_{1-x}A_xYO_3$ ($0.0 \leq x \leq 0.20$) is very limited i.e. x=0.05 in both the cases. The volume fraction of secondary phases increases with the increasing concentration of substituents. The formation of secondary phase also acts as grain inhibiter. The TEC of the samples lies in the range of 8.30-10.06 $\times 10^{-6}$ $°C^{-1}$.

4.4 $Bi_{1-x}A_xCrO_3$ (A=Sr, Ca; 0.40≤x≤0.55)

Cr being prior to Mn in the periodic table and having almost same ionic radii as that of Mn (ionic radii of Mn= 0.78 Å and Cr=0.75 Å). It is the fourth substituents which was planned to study as the B-site cation in the present work. But the synthesis of Sr^{2+}/ Ca^{2+} substituted $BiCrO_3$ is not possible by solid state reaction method. The $Bi_2(CrO_4)_2Cr_2O_7$ and $SrBi_2O_4$/$CaBi_2O_4$ phases are observed in all the synthesized samples (shown in figure 4.51 as representative XRD patterns). Moreover, the density of all the samples was less than 40 % of the theoretical density. So, these samples cannot be used for the conductivity measurements. For any characterization the samples should be dense with very low porosity. The samples with low Sr^{2+}/Ca^{2+} substituent concentration were also tried, but they also show the formation of secondary phase with very low density. Due to these reasons, these samples were not considered for further investigated by other techniques as their utility factor is very low.

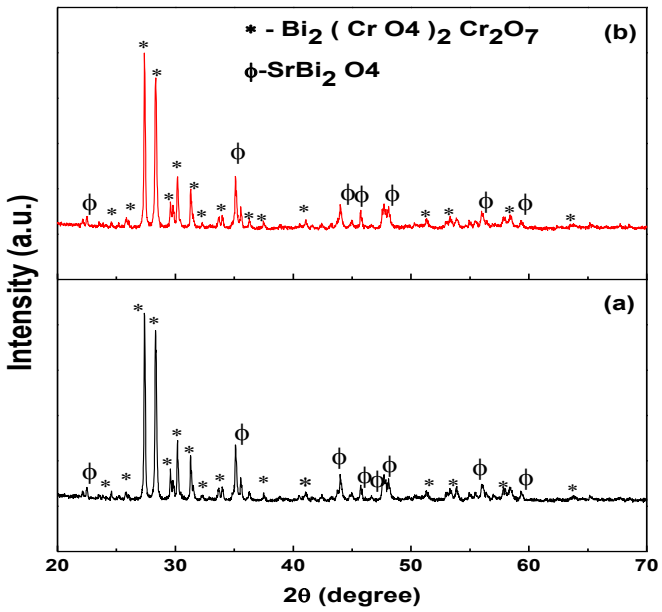

Figure 4.41: XRD pattern of (a) $Bi_{0.50}Sr_{0.50}CrO_3$ (b) $Bi_{0.50}Ca_{0.50}CrO_3$.

References

[1] J. Hejtmanek, K. Knizek, Z. Jirak, M. Hervieu, C. Martin, M. Nevriva, P. Beran, J. Appl. Phys. 93 (2003) 7370.

[2] S. Yamada, T. Matsunaga, E. Sugano, Phys. Rev. B 75 (2007) 214431.

[3] R. D. Shannon, Acta Cryst. A32 (1976) 751.

[4] G. L. Yuan, S. W. Or, H. Lai, W. Chan, J. Phys D: Appl. Phys. 40 (2007) 1196.

[5] N. Dasgupta, R. Krishnamoorthy, J. Thomas, Mater. Sci. Engg. B 90 (2002) 278.

[6] A. Belik, K. Kodama, N. Igawa, S. Shamoto, K. Kosuda, E. Takayama-Muromachi, J. Am. Chem. Soc. 132 (2010) 8137.

[7] R. L. Withers, L. Bourgeois, K. Balamurugan, N. K. Harish, P. N. Santhosh, P. M. Woodward, J. Solid State Chem. 182 (2009) 2176.

[8] D. W. Boukhvalov, I. V. Solovyev, Phys. Rev. B 82 (2010) 245101.

[9] M. C. Biesingera, B. P. Payne, A. P. Grosvenord, L. W. M. Laua, A. R. Gerson, S. C. Roger, Appl. Surf. Sci. 257 (2011) 2717.

[10] H. W. Nesbitt, D. Banerjee, Am. Mineral. 83 (1998) 305.

[11] M. S. Kim, J. B. Yang, J. Medvedeva, W. B. Yelon, P. E. Parris, W. J. James, J. Phys.: Condens. Matter 20 (2008) 255228.

[12] V. Goian, S. Kamba, M. Savinov, D. Nuzhnyy, F. Borodavka, P. Vanek, A. A. Belik. J. Appl. Phys. 112 (2012) 074112.

[13] P. Toulemonde, C. Darie, C. Goujon, M. Legendre, T. Mendonca, M. Alvarez-Murga, V. Simonet, P. Bordet, P. Bouvier, J. Kreisel, M. Mezouar, High Pressure Research 29 (2009) 600.

[14] M. Hervieu, A. Maignan, C. Martin, N. Nguyen, B. Raveau, Chem. Mater. 13 (2001) 1356.

[15] M. N. Iliev, M. V. Abrashev, H. G. Lee, V. N. Popov, Y. Y. Sun, C. Thomsen, R. L. Meng, C. W. Chu, Phys. Rev. B 57 (1998) 2872.

[16] S. Q. Liu, N. J. Wu, A. Ignatiev, Appl. Phys. Lett. 76 (2000) 2749.

[17] T. Kawasaki, Y. Ogimoto, N. Ogawa, K. Miyano, H. Tamaru, M. Izumi, J. Appl. Phys. 101 (2007) 123714.

[18] G. L. Yuan, S. W. Or, H. L. W. Chan, J. Phys. D: Appl. Phys. 40 (2007) 1196.

[19] D. Wu, Y. Deng, C. L. Mak, K. H. Wong, A. D. Li, M. S. Zhang, N. B. Ming, Appl. Phys. A 80 (2005) 607.

[20] X. Li, X. Wang, Y. Li, W. Mao, P. Li, T. Yang, J. Yang, Mater. Lett. 90 (2013) 152.

[21] S. S. Rojas, J. E. D. Souza, M. R. B. Andreeta, A. C. Hernandes, J. Non-Cryst. Solids 356 (2010) 2942.

[22] Y. Chang, H. Xiao, W. Guo, Thermochim. Acta 444 (2006) 173.

[23] G. Singh, A. Sil , S. Ghosh, Physica B 404 (2009) 3807.

[24] K. J. Park, C. H. Kim, Y. J. Yoon, S. M. Song, Y. T. Kim, K. H. Hur, J. Eur. Ceram. Soc. 29 (2009) 1735

[25] J. Richter, P. Holtappels, T. Graule, L. J. Gauckler, Solid State Ionics 179 (2008) 2284.

[26] J. L. Garcia-Munoz, C. Frontera, M.A.G. Aranda, A. Llobet, C. Ritter, Phy. Rev. B 63 (2001) 064415.

[27] B.H. Kim, J.S. Kim, M.S. Kim, C.J. Zhang, K.H. Kim, B.G. Kim, H.C. Kim, Y.W. Park, Phys. Lett. A 351 (2006) 368.

[28] S.P. Jiang, J. Mater. Sci. 43 (2008) 6799.

[29] B. Liu, Z. Jianga, B. Dinga, F. Chen, C. Xia, J. Power Sources 196 (2011) 999.

[30] G. Singla, P. K. Jha, O.P. Pandey, K. Singh, Ceram. Int. 38 (2012) 2065.

[31] R. Kant, K. Singh, O. P. Pandey, Int. J. Hydrogen Energy 33 (2008) 455.

[32] Q. Li, V. Thangadurai, J. Mater. Chem. 20 (2010) 7970.

[33] V. V. Kharton, F. M. B. Marques, Curr. Opn. Solid State Mater. Sci. 6 (2002) 261.

[34] M. C. Steil, J. Fouletier, M. Kleitz, P. Labrune, J. Eur. Ceram. Soc. 19 (1999) 815.

[35] I. Abraham, F. Krok, J. Mater. Chem. 12 (2002) 3351.

[36] B. Bhushan, A. Basumallick, S. K. Bandopadhyay, N. Y. Vasanthacharya, D. Das, J. Phys. D: Appl. Phys. 42 (2009) 065004.

[37] A. K. Pradhan, K. Zhang, D. Hunter, J. B. Dadson, G. B. Loutts, J. Appl. Phys. 97 (2005) 093903.

[38] K. Brinkman, T. Iijima, H. Takamura, Jpn. J. Appl. Phys. Part 2 46 (2007) L93.

[39] K. Brinkman, T. Iijima, H. Takamura, Solid State Ionics 181 (2010) 53.

[40] J. Mizusaki, M. Okayasu, S. Yamauchi, K. Fueki, J. Solid State Chem. 99 (1992) 166.

[41] D. D. Zaitsev, P. E. Kazin, Y. D. Tretyakov, M. Jansen, Inorg. Mater. 39 (2003) 1319.

[42] P. D. Battle, T.C. Gibb, P. Lightfoot, J. Solid State Chem. 84 (1990) 237.

[43] J. Li, Y. Duan, H. He, D. Song, J. Alloys Comp. 315 (2001) 259.

[44] B. H. Kim, J. S. Kim, M. S. Kim, C. J. Zhang, K. H. Kim, B. G. Kim, H. C. Kim, Y. W. Parka, Phy. Lett. A 351 (2006) 368.

[45] D. C. Jia, J. H. Xu, H. Ke, W. Wang, Y. Zhou, J. Eur. Cer. Soc. 29 (2009) 3099.

[46] P. D. Battle, T.C. Gibb and P. Lightfoot, J. Solid State Chem. 84 (1990) 237.

[47] K. Rida, A. Benabbas, F. Bouremmad, M. A. Pena, E. Sastre, A. Martinez-Arias, Appl. Catal. A 327 (2007) 173.

[48] S. K. Mandal, T. Rakshit, S. K. Ray, S. K. Mishra, P. S. R. Krishna, A. Chandra, J. Phys.: Condens. Matter 25 (2013) 055303.

[49] R. Das, T. Sarkar, K. Mandal, J. Phys. D: Appl. Phys. 45 (2012) 455002.

[50] E. D. Wachsman, S. Boyapati, N. Jiang, Ionics 7 (2001) 1.

[51] Y. Wang, C.W. Nan, J. Appl. Phys. 103 (2008) 114104.

[52] Z. Wen, X. Shen, D. Wu, Q. Xu, J. Wang, A. Li, Solid State Comm. 150 (2010) 2081.

[53] D. Varshney, A. Kumar, J. Mol. Struct. 1038 (2013) 241.

[54] D. Kothari, V.R. Reddy, V.G. Sathe, A. Gupta, A. Banerjee, A. M. Awasthi, J. Magn. Magn. Mater. 320 (2008) 548.

[55] P. Naik, J.J. Mazarko, C.S. Flattery, U.D. Venkateswaran, V.M. Naik, M. S. Mohammed, G.W. Auner, J.V. Mantese, N.W. Schubring, A.L. Micheli, A.B. Catalan, Phys. Rev. B 61 (2000) 11367.

[56] S.K. Pradhan, J. Mater Sci. Mater. Electron. 24 (2013) 3581.

[57] S. K. Srivastav, N. S. Gajbhiye, A. Banerjee, J. Appl. Phys. 113 (2013) 203917.

[58] P. C. Sati, M. Arora, S. Chauhan, S. Chhoker, M. Kumar, J. Appl. Phys. 112 (2012) 094102.

[59] R. K. Mishra, D. K. Pradhan, R. N. P. Choudhary, A. Banerjee, J. Phys.: Condens. Matter 20 (2008) 045218.

[60] S. Farhadi, M. Zaidi, J. Mol. Catalysis A: Chemical 299 (2009) 18.

[61] R. Punia, R.S. Kundu, J. Hooda, S. Dhankhar, S. Dahiya, N. Kishore, J. Appl. Phys. 110 (2011) 0335271.

[62] F. H. ElBatal, M. A. Marzouk, A. M. Abdelghany, J. Mater. Sci. 46 (2011) 5140.

[63] N. Du, Y. Xu, H. Zhang, C. Zhai, D. Yang, Nanoscale Res. Lett. 5 (2010) 1295.

[64] S.N. Kumar, P. Kumar, D.K. Agrawal, Ceram. Int. 38 (2012) 5243

[65] M. D. Antonik, R. J. Lad, J. Vac. Sci. Technol. A 10 (1992) 669.

[66] H. Liu, T. Liu, X. Wang, Solid State Comm. (2009) 1958.

[67] A. Khomchenko, D.A. Kiselev, J.M. Vieira, Li Jian, A.L. Kholkin, A.M.L. Lopes, Y.G. Pogordov, J.P. Arayo, M. Maglione, J. Appl. Phys. 103 (2008) 024105.

[68] D. I. Khomskii, J. Magn. Magn. Mater. 306 (2006) 1.

[69] D. Varshney, A. Kumar, K. Verma, J. Alloys Comp. 509 (2011) 509 8421.

[70] F. Chen, O. T. Sorensen, G. Meng, D. Peng, J. Mater. Chem. 7 (1997) 481.

[71] A. Petric, P. Huang, F.Tietz, Solid State Ionics 135 (2002) 719.

[72] J. Richter, P. Holtappels, T. Graule, L. J. Gauckler, Solid State Ionics 179 (2008) 2284.

[73] D. Bahadur, W. Fischer, M.V. Rane, Mater. Sci. Engg. A252 (1998) 109.

[74] C. Kostogloudis, N. Vasilakos, C. Ftikos, Solid State Ionics 106 (1998) 207.

[75] S. Banerjee, A. Kumar, J. Appld. Phys 109 (2011)114313.

[76] M. Prabu, S. Selvasekarapandian, A.R. Kulkarni, S. Karthikeyan, G. Hirankumar, C. Sanjeeviraja, Solid State Sciences 13 (2011) 1714.

[77] N. Maso, A. R. West, Chem. Mater. 24 (2012) 2127.

[78] H. Yamamura, K. Yamazaki, K. Kakinuma, K. Nomura, Solid State Ionics 150 (2002) 255.

[79] V. B. Balakireva, A. Y. Stroeva, V. P. Gorelov, Russian J. Electrochem. 41 (2005) 535.

[80] N. V. Minh, J. Phy D: Conference Series 187 (2009) 012011.

[81] G.A. Nazri, C. Julien, Solid State Ionics 53 (1992) 376.

[82] P. Dumrongrojthanath, T. Thongtem, A. Phuruangrat, S. Thongtem, J. Superlattices Microstruct. 54 (2013) 71.

[83] T. K. Vishnuvardhan, V. R. Kulkarni, C. Basavaraja, S. C. Raghavendra, Bull. Mater. Sci. 29 (2006) 77.

[84] T. Norby, P. Kofstad, J. Am. Ceram. Soc. 67 (1984) 786.

[85] E. Ruiz-Trejoa, M.S. Islamc, J.A. Kilnera, Solid State Ionics 123 (1999) 121.

[86] R. Metz, H. Delalu, J.R. Vignalou, N. Achard, M. Elkhatib, Mater. Chem. Phys. 63 (2000) 157.

[87] J. B. Goodenough, Crystalline Solid State Electrolytes II: Material Design in Solid State Electrochemistry (1995) Cambridge University Press Cambridge U.K.

[88] I. Kosacki, H.U. Anderson, Y. Mizutani, K. Ukai, Solid State Ionics 152–153 (2002) 431.

[89] K. Huang, R. S. Tichy, J. B. Goodenough, J. Am. Ceram. Soc. 81 (1998) 2565.

[90] J. H. Gong, Y. Li, Z. L. Tang, Y.S. Xie, Z.T. Zhang, Mater. Chem. Phys. 76 (2002) 212.

[91] M. Kurumada, H. Hara, F. Munakata, E. Iguchi, Solid State Ionics 176 (2005) 245.

Chapter 5

RESULTS AND DISCUSSION-II

Overview

On the basis of highest conductivity and optimum thermal expansion coefficient values, the BSM-50, BCM-50, BSF-50 and BCF-50 samples have been selected to investigate their chemical compatibility with the YSZ electrolyte. Diffusion couples are heat treated for 1, 50 and 100 h durations. The samples obtained after heat treatments are investigated by XRD to check the phases formed after the interaction between cathode and electrolyte. The interfacial growth and morohology with respect to time between the cathodes and YSZ electrolyte is investigated by the SEM. The elemental analysis of interface and vicinity is done by X-ray dot mapping. The formation of different phases and the diffusion of cations have been discussed on the basis of tolerance factor and the stability of B-site cations.

5.1 Interaction Study

During the fabrication and operation of SOFCs, an interface is formed between the cathode and electrolyte due to the inter-diffusion of different cations and anions from both the sides. This inter-diffusion results in the formation of crystalline phases which can result in the degradation of properties of these materials. So, some selected samples of the present study have also been investigated for their chemical compatibility with YSZ electrolyte in this chapter. The selection of YSZ is based on its best properties as an electrolyte.

In the last chapter, the structural, thermal and electrical properties of $Bi_{1-x}A_xMO_3$ (A=Sr, Ca; 0.40 ≤x ≤0.55; M=Fe, Mn, Cr) and $Bi_{1-x}A_xYO_3$ (0.0≤x≤0.20) have been discussed. It has been observed that all the systems containing Fe and Mn at B-site exhibit maximum conductivity at x=0.50 concentration of Sr^{2+}/Ca^{2+} with moderate coefficient of thermal expansion. In the present section BSM-50, BCM-50, BSF-50 and BCF-50 samples have been investigated for their chemical compatibility with YSZ electrolyte. The BCY and BSY systems have not considered for interaction study due to the absence of phase purity, low solubility of dopants and low conductivity of these systems.

5.2 BSM-50/ YSZ system

The interaction study for different durations has led to the formation of different phases. The XRD patterns of BSM-50/YSZ system after 1, 50 and 100 h heat treatments at 800 °C in shown in figure 5.1. $SrZrO_3$ (ICDD card No. 076-0167) and m-ZrO_2 (ICDD card No. 033-0937) are the major phases observed in this interaction study which are undesirable. Since, the formed strontium zirconate ($SrZrO_3$) and zirconium oxide (ZrO_2) phases have high melting point, low thermal conductivity and high thermal expansion coefficient, so, they are undesirable for SOFC applications. Their ionic conductivity is also very low, so, their presence can have negative impact on the properties of the cathode and electrolyte [1, 2]. These phases in the present system start appearing even after 1h of heat treatment. Kindermann *et al.* [3] have already reported that higher Sr content will enhance the formation of secondary phases. In present system the Sr content is up to 50 mol% so, there is ample chance of nucleation of these phases even for short duration of interaction. With the increase in duration of the heat treatments, the volume fraction percentage of these phases also increases. The volume fraction of the different phases formed in these systems has been calculated and given in table 5.1. To calculate the volume fraction of different phases, the

major peaks in XRD pattern for BSM-50, YSZ, ZrO_2 and $SrZrO_3$ were considered and the ratio of the area of these peaks was used for the calculation i.e. also called direct comparison method [4]. The XRD patterns obtained after heat treatments also exhibit a shift to lower diffraction angle side as compared to pristine samples of BSM-50 and YSZ. This shift in XRD peaks can be attributed to the diffusion of different ions from both the sides; BSM and YSZ side [5].

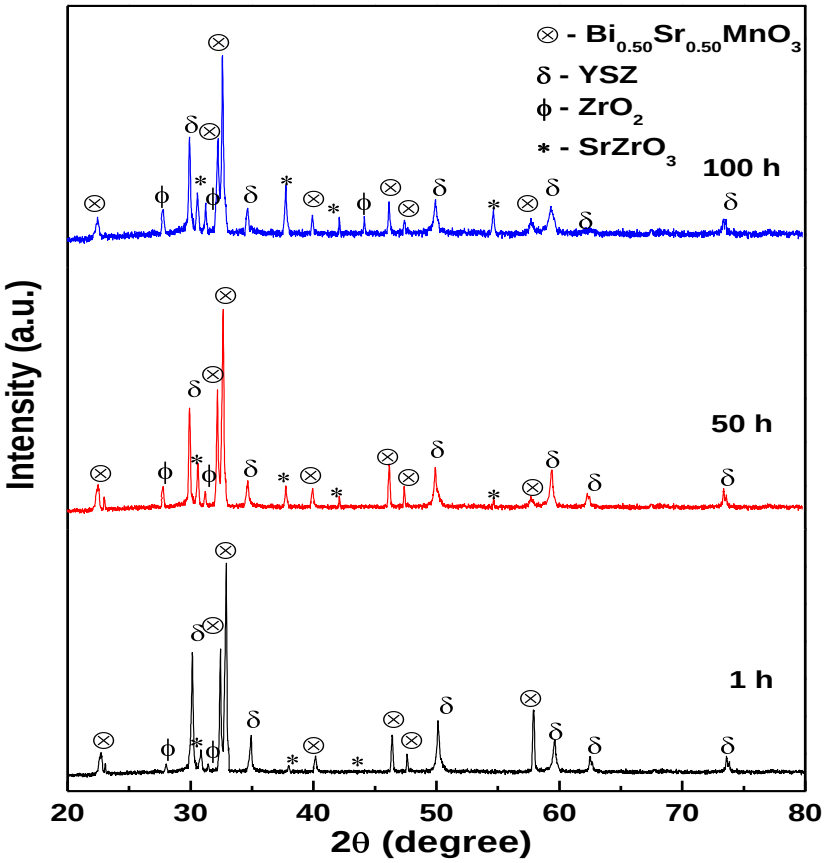

Figure 5.1: XRD patterns of BSM-50/YSZ after 1h, 50 h and 100 h heat treatment.

The interface of the samples obtained after 100 h heat treatment is shown in figure 5.2. The interface between the BSM and YSZ does not show any adherence. This can be due to the different thermal expansion coefficient of BSM (9.44×10^{-6} °C^{-1}) and YSZ (11.01×10^{-6} °C^{-1}). The difference in TEC results in the thermal stresses at the interface which leads to crack, nucleation, formation of pores and ultimately poor adherence. The X-ray dot mapping clearly indicates that all the elements have diffused into each other side. The maximum diffusion is observed for Zr followed by Sr and Bi. However, the diffusion of other elements is less. The diffusion of Zr and Y from electrolyte to cathode side has also been reported for LSM and LSF cathodes [5, 6]. The elements from the BSM side have also diffused into the YSZ side

but their diffusion is relatively small. The diffusion of Sr and Bi is comparatively large from BSM side as compared to Mn. The low diffusion of Mn can be due to the stronger MnO_6 octahedra as compared to BiO_6 octahedra in the unit cell [7].

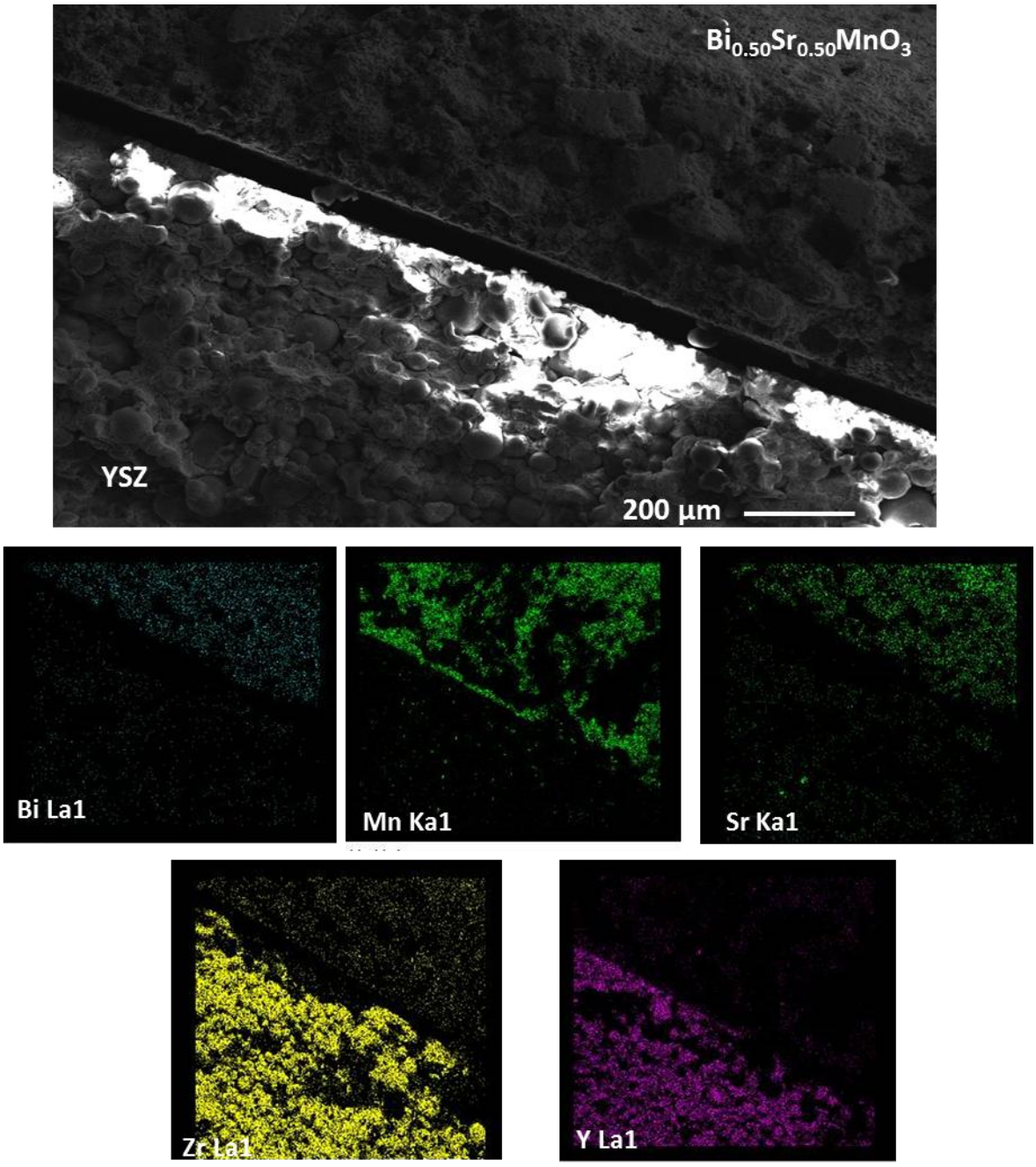

Figure 5.2: SEM and X-ray dot mapping of BSM-50/YSZ after 100 h heat treatment.

5.3 BCM-50/YSZ system

Interaction study of BCM-50/YSZ systems was done for different durations at 800 °C. The XRD patterns as shown in figure 5.3 which shows the presence of $Ca_{0.2}Zr_{0.8}O_{1.8}$ (ICDD card No. 01-075-0359) and ZrO_2 after heat treatments. The ZrO_2 phase was absent in the 1 h heat

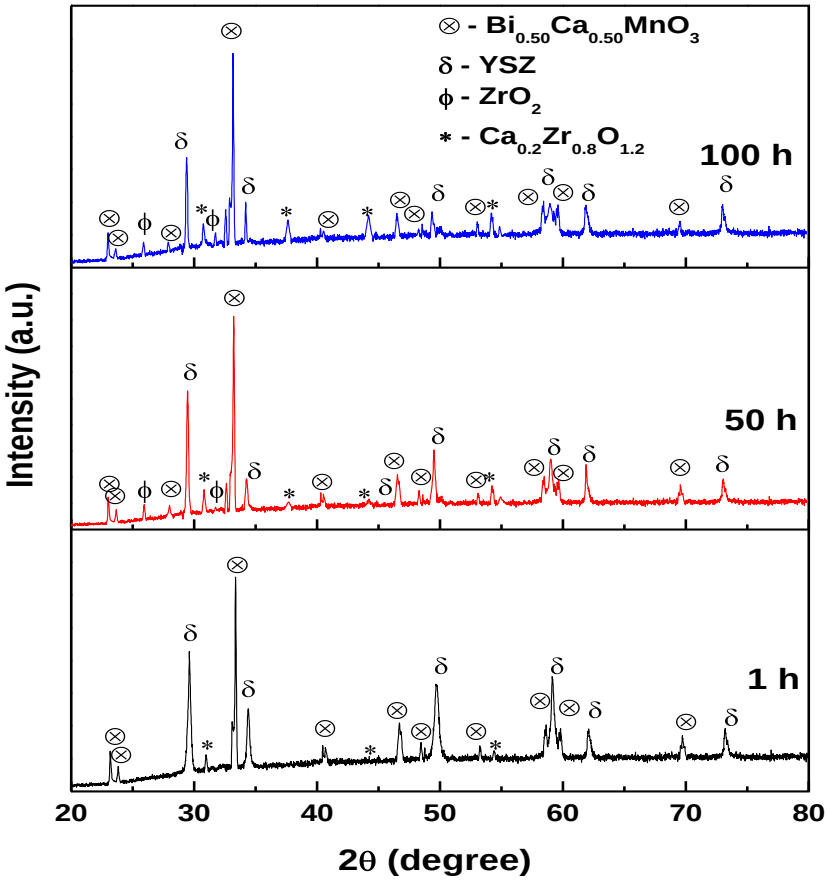

Figure 5.3: XRD patterns of BCM-50/YSZ after 1h, 50h and 100 h heat treatment.

treated diffusion couple. However, after 50 h of heat treatment, some crystalline phases nucleates and grows. The volume fraction of different phases is calculated and given in table 5.1. However, as compared to BSM-50, in BCM-50 the volume of undesirable phases is low. This can be explained on the basis of tolerance factor. Kindermann *et al.* [3] in their study have reported that tolerance factor plays an important role in determining the formation of different phases in the perovskite systems. The formation of different phases is basically controlled by the oxygen ion diffusion energies. For the oxides having high tolerance factor, this oxygen ion diffusion energy is low, which further enhances the formation of m-ZrO_2 and $SrZrO_3$. Sr^{2+}containing systems have higher effective ionic radii as compared to Ca^{2+} substituted system, so, BSM will have high tolerance factor as compared to BCM system. As

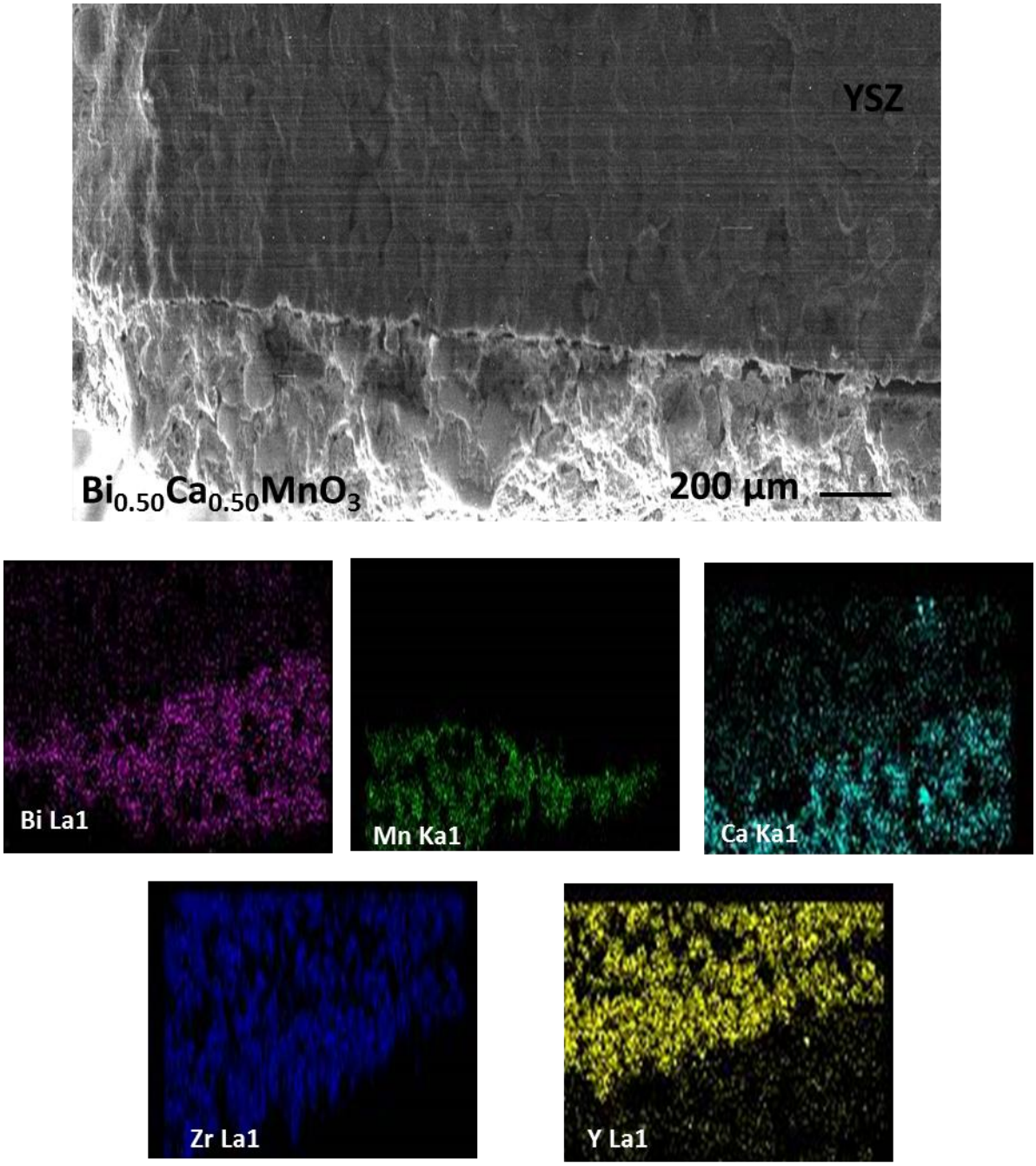

Figure 5.4: SEM and X-ray dot mapping of BCM-50/YSZ after 100 h heat treatment.

discussed above, due to high tolerance factor values, the chances of formation of m-ZrO_2 and $SrZrO_3$ in BSM sample will be more as compared to BCM sample which is further supported by the XRD results. The interface of the BCM-50/YSZ and the X-ray dot mapping of the interface is presented in figure 5.4. It is clear from the micrographs that the interface between the BCM and YSZ show some adherence. However, it is not smooth and shows some pores also. The X-ray dot mapping clearly indicates the diffusion of different ions on both sides.

The bismuth and calcium have diffused up to the entire length of YSZ. Whereas, diffusion of Zr, Y and Mn has occurred up to certain distance near the interface and decreases as one move away from the interface. Whereas, in BSM system, the diffusion length is uniform for all the cations. This difference can also be attributed to the different unit cell volume and tolerance factor of both the systems as discussed in XRD study [8].

5.4 BSF-50/YSZ system

The XRD patterns of BSF-50/YSZ system obtained after 1, 50 and 100 h of interaction at 800 °C is presented in figure 5.5. The XRD patterns confirm the presence of $SrZrO_3$ and ZrO_2 phases in all the samples exposed to different treatment cycles. The volume fraction of all the samples obtained from direct comparison method is given in table 5.1. The values in the table indicate that volume fraction of phases formed increases with the increase in duration of heat treatments. The XRD peaks of BSF in this system also shift to lower diffraction angle side as compared to pristine BSF and YSZ samples. This shift also increases with the increase in duration of heat treatments. This shift indicates towards the unit cell expansion due to the

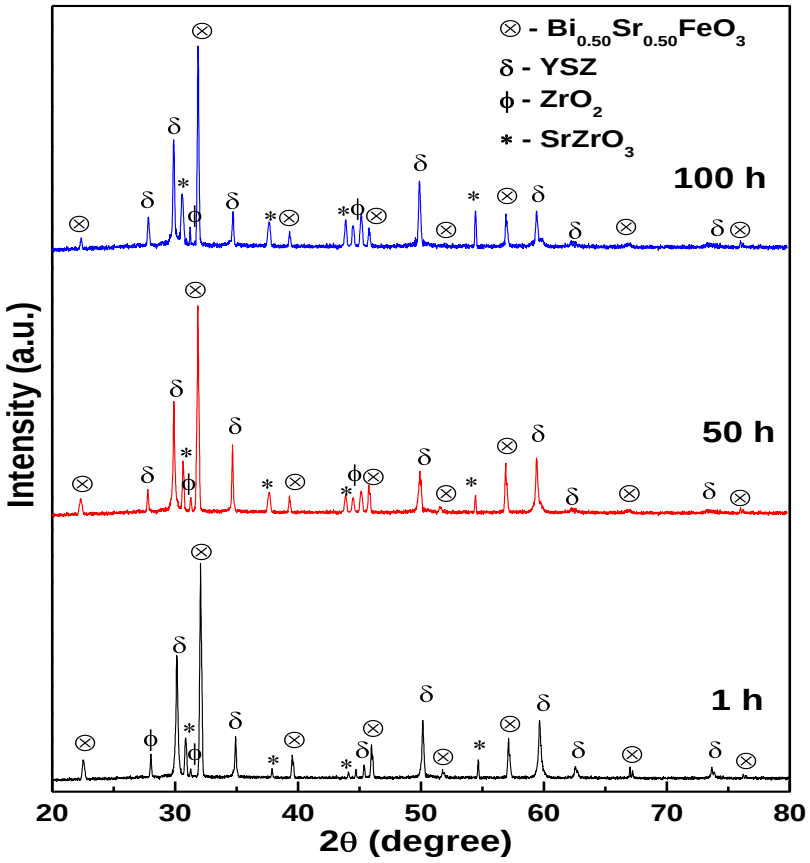

Figure 5.5: XRD patterns of BSF-50/YSZ after 1h, 50h and 100 h heat treatment.

dissolution of Zr ions into BSF lattice. There is also shift in the XRD peaks of YSZ which is quite expected as Zr ions are moving towards the perovskite side (BSF) and because of it fluorite structure becomes Y rich. But it is quite difficult to conclude from these shifts in XRD peaks as XRD patterns of different Zr concentration in YSZ are almost same e.g. YSZ-9 (9 mol % Y_2O_3 stabilized zirconia) has highest peak at 30.068° and unit cell volume 68.03 Å and YSZ-5 (5 mol % Y_2O_3 stabilized zirconia) has highest peak at 30.068° and unit cell volume 67.60 Å. Hence, such small peak variation in XRD peaks is difficult to resolve with accuracy [5, 9].

The volume fraction of $SrZrO_3$ and ZrO_2 is more in this sample as compared to manganite based systems. The tolerance factor of BSF system should be large as ionic radii of Fe^{3+} is small as compared to $Mn^{3+.}$ The oxygen vacancy concentration is quite high which reduces the tolerance factor in these systems. As discussed in BCM-50/YSZ interaction study that the decrease in the tolerance factor also decreases the probability of formation of these undesirable phases. According to this, the formation of these phases should be suppressed in these systems but opposite trend has been observed in this system. So, in this system, other effect must be prominent as compared to low tolerance factor values. It is well reported in literature that stability of B-site cation also affects the reactivity of the perovskite oxides. Higher the stability of B-site cation in the higher oxidation state, lower will be the probability of formation of these phases [3]. The low stable compounds will enhance the formation of $SrZrO_3$ phase in the system. As Fe in higher oxidation is less stable as compared to $Mn^{3+,}$ so, BSF system will be more reactive as compared to manganite based systems after 100 h treatment is also shown in this figure 5.6. Proper adhesion between the BSF-50 and YSZ samples can be seen at the interface. The interface is not smooth and have small pores. The X-ray dot mapping reflects the diffusion of all the cations on the both sides of the interface. Bi, Zr and Y shows maximum diffusion into both sides whereas, the diffusion in case of Sr and Fe is comparatively low. The concentration of diffused ions is maximum near the interface and it gets diluted as one move away from the interface. The X-ray dot mapping clearly reflects the higher diffusion in these samples as compared to BSM and BCM samples which is further supported by the XRD data.

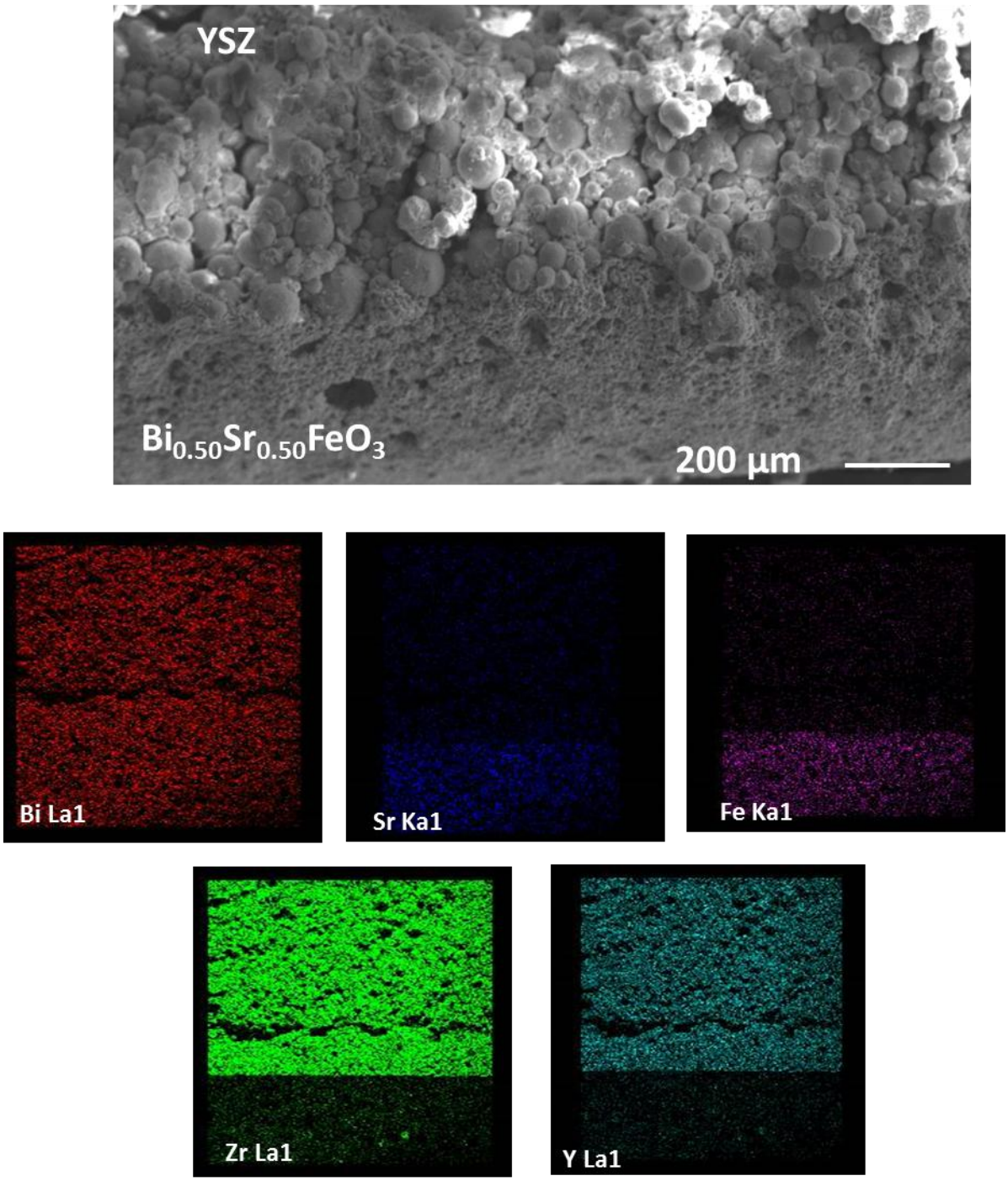

Figure 5.6: SEM and X-ray dot mapping of BSF-50/YSZ after 100 h heat treatment.

5.5 BCF-50/YSZ system

The $CaZrO_3$ (ICDD card No. 01-075-0359) and ZrO_2 phases are present in all the samples as shown in figure 5.7. The volume fraction of these phases is tabulated in table 5.1. The volume fraction of these phases increases with the increase in the time duration of heat treatments. However, the volume fraction of these phases is low as compared to BSF-50 system but still it is high as compared to manganite based systems. The decrease in volume of

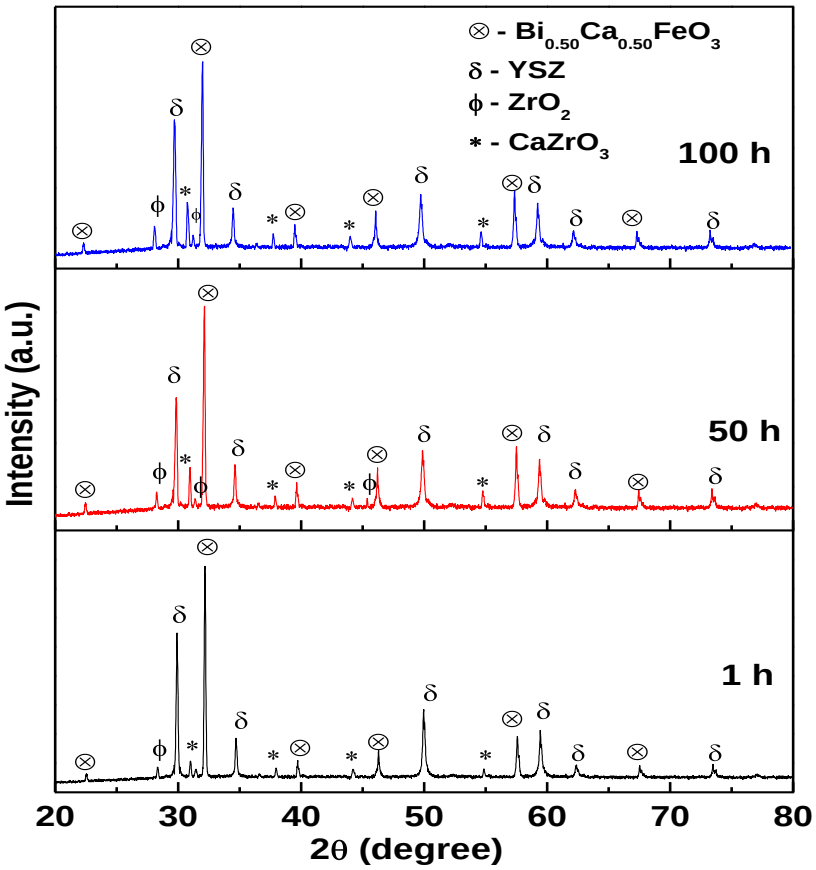

Figure 5.7: XRD patterns of BCF-50/YSZ after 1h, 50 h and 100 h heat treatment.

these phases as compared to BSF-50 can be attributed to the smaller ionic radii and the tolerance factor of BCF samples. As discussed in BCM-50/YSZ section, the smaller tolerance factor values inhibit the formation of these undesirable phases. The high reactivity of these samples as compared to manganite systems can be attributed to the high instability of B-site cation 'Fe' as compared to Mn as discussed in BSF system.

The interface between the BCF-50 and YSZ is shown in figure 5.8 along with X-ray dot mapping results. The micrograph shows very poor adherence between BCF and YSZ surface.

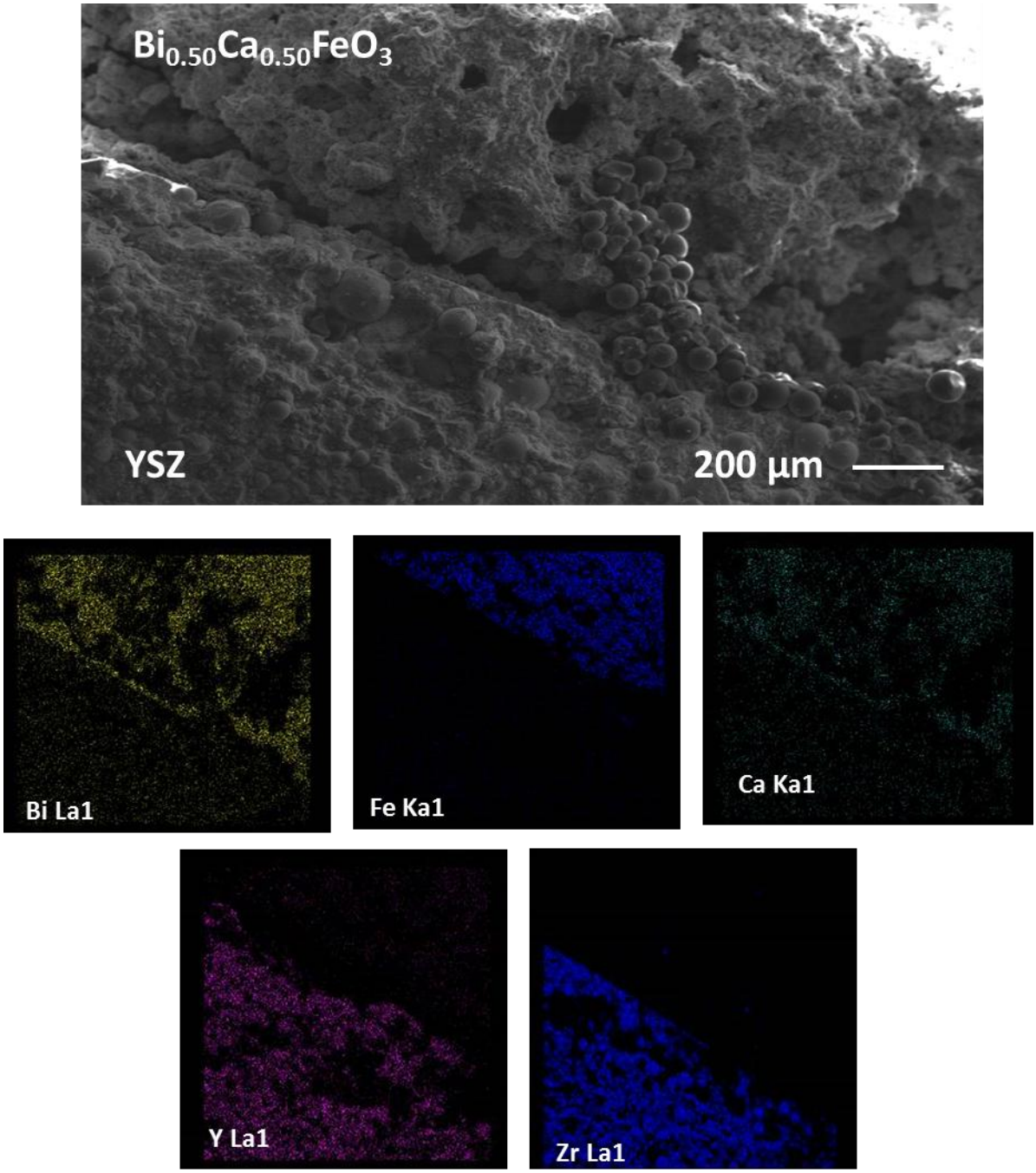

Figure 5.8: SEM and X-ray dot mapping of BCF-50/YSZ after 100 h heat treatment.

The thermal expansion coefficient of BCF (9.04×10^{-6} °C^{-1}) and YSZ (11.01×10^{-6} °C^{-1}) are quite different. The difference in TEC of both the materials generate the thermal stresses and hence results in poor adhesion and formation of pores [10]. The diffusion of all the cations on both the sides of interface is quite clear from the X-ray dot mapping. Even in this particular sample, the interface has been ruptured and the flow of mass from YSZ side to BCF side is quite clear. When this interface is compared with the X-ray dot mapping, it can be concluded

that the zirconium oxide has ruptured the interface and flows from one side to another. In this sample, bismuth and calcium shows maximum diffusion. Yttrium has also diffused from YSZ side to BCF side but the diffusion concentration is low as compared to Bi and Ca. The Zr has also diffused to the other side but its diffusion length is quite small. The X-ray dot mapping clearly shows the diffusion of Zr along the interface but it is not over the entire surface. Fe shows very less diffusion in the YSZ side. These samples show less diffusion as compared to BSF samples which can be attributed to high oxygen ion diffusion energies in these systems due to low tolerance factor of this system [11, 12].

Table 5.1: Volume fraction of different phases formed during the interaction study.

System	**Time duration (h)**	**Volume fraction of different phases (%)**			
		$SrZrO_3$	**ZrO_2**	**$Ca_{0.2}Zr_{0.8}O_{1.2}$**	**$CaZrO_3$**
BSM-50/8 YSZ	1	9.7	2.61	-	-
	50	11.6	3.01	-	-
	100	14.3	4.95	-	-
BCM-50/8 YSZ	1	-	-	7.16	-
	50	-	2.8	9.2	-
	100	-	3.94	11.5	-
BSF-50/8 YSZ	1	12.09	3.21	-	-
	50	18.8	6.7	-	-
	100	24.78	9.37	-	-
BCF-50/8 YSZ0	1	-	2.13	-	4.1
	50	-	3.58	-	11.7
	100	-	5.84	-	18.4

The interaction study performed for the synthesized samples indicates that the interface obtained is not smooth because of difference in TEC of developed cathode material and YSZ. Among the studied samples, the BCM-50/YSZ exhibits the better interface. The volume fraction of crystalline phases increases with increasing heat treatments duration. These phases are very detrimental for SOFC applications point of view.

References

[1] C. Nivot, C. Legros, B. Lesage, M. Kilo, C. Argirusis, Solid state Ionics 180 (2009) 1040.

[2] B. Bochentyn, J. Karczewski, M. Gazada, P. Jasinski, B. Kusz, Phys. Status Slidii A 210 (2013) 538.

[3] L. Kindermann, D. Das, H. Nickel, K. Hilpert, Solid State Ionics 89 (1996) 215.

[4] V. Kumar, S. Sharma, O. P. Pandey, K. Singh, Solid State Ionics 181 (2010) 79.

[5] M. D. Anderson, J. W. Stevenson, S. P. Simmer, J. Power Sources 129 (2004) 188.

[6] M. Gazada, P. Plonczak, S. Molin, B. Kusz, P. Jasinski, Acta Phys. Polonica A 114 (2008) 135.

[7] J. A. Alonso, M. J. MartInez-Lope, M. T. Casais, M. T. Fernandez-DIaz, Inorg. Chem. 39 (2000) 917.

[8] L. Kindermann, D. Das, D. Bahafdur, R. Weib, H. Nickel, K. Hilpert, J. Am. Cer. Soc. 80 (1997) 909.

[9] M. Yashima, S. sasaki, S. Kakihana, M. Yamaguchi, H. arashi, M. Yoshimura, Acta Cryst. Sec. B Struct. Sci. 50 (1994) 663.

[10] G. Kaur, D. Homa, K. Singh, O.P. Pandey, B. Scott, G. Pickrell, J. Power Sources 242 (2013) 305.

[11] M. Cherry, M. S. Islam, C.R. A. Catalow, J. Solid State Chem. 118 (1995) 125.

[12] Alexander Chroneos, Bilge Yildiz, Albert Tarancón, D. Parfitta, J. A. Kilner, Energy Environ. Sci. 4 (2011) 2774.

Chapter 6

CONCLUSIONS AND FUTURE SCOPE

Overview

The effect of different substituents and the different B-site cations has been summarized and concluded in this chapter. The results of interaction study with YSZ electrolyte has also been compared and summarized. At the end of this chapter, the future scope of this work has been given on the basis of the results obtained from the present study.

6.1 Conclusions

In the present system, bismuth based perovskite structured materials were synthesized and characterized for their potential application as cathode materials in IT-SOFC. The work was planned on the theme that mixed ionic electronic conductors are the best possible solutions for the IT-SOFCs as in these materials the triple phase boundary can be extended to the entire cathode surface which reduces the polarization resistance and enhances the overall cell output.

Polycrystalline perovskite oxides of $Bi_{1-x}A_xMO_3$ (A=Sr, Ca; $0.40 \leq x \leq 0.50$; M=Fe, Mn, Cr) and $Bi_{1-x}A_xYO_3$ (A=Sr, Ca; $0.0 \leq x \leq 0.20$) have been synthesized by solid state reaction method and characterized to study the variation in their structural, thermal and electrical properties. The selected samples are also characterized for their chemical interaction with YSZ electrolyte. The outcomes of the entire study are concluded below:

In the $Bi_{1-x}A_xMnO_3$ (A=Sr, Ca; $0.40 \leq x \leq 0.55$) system, the substitution of Sr^{2+} and Ca^{2+} leads to more symmetric tetragonal and orthorhombic structures as compared to monoclinic structure of undoped $BiMnO_3$. Raman and FT-IR results also support the XRD results where the disappearance/shifting of bands clearly reflect the disordering in the substituted samples. XPS and iodometric results reveal that the substitution of cations change the oxidation state of B-site cations in addition to oxygen vacancies The microstructures of the samples show that all the samples have equiaxed grains with very low porosity which leads to good experimental density. The present samples undergo two phase transitions around 300 and 600 °C due to the charge ordering and phase transition from tetragonal/orthorhombic to orthorhombic/rhombohedral structures, respectively. The TEC of all the samples lies in the range of 9.50-10.60 $\times 10^{-6}$ $°C^{-1}$ which is in the required range for SOFC applications. The maximum conductivity 0.09 S cm^{-1} is observed in BSM-50 sample which can be attributed to the more symmetric crystal structure, appropriate concentration of oxygen vacancies/Mn^{4+} and uniform grain size distribution in this sample.

$Bi_{1-x}A_xFeO_3$ (A=Sr, Ca; $0.40 \leq x \leq 0.55$) samples exhibit tetragonal structure with *p4mm* symmetry for both Sr^{2+}/ Ca^{2+} substituted systems up to x=0.50. For x=0.55, the BSF sample exhibit superstructure with *pnma* symmetry which can be attributed to the ordering of oxygen vacancies, whereas in BCF system, the secondary phase Ca_2FeO_5 starts appearing for x=0.55 sample. The iodometric results indicate that concentration of Fe^{4+} is quite low and the charge

compensation in these systems is mainly through the oxygen vacancies. Presence of only eight bands in the Raman spectra of present studied samples clearly indicates the evolution of tetragonal structure as compared to rhombohedral structure of the undoped $BiFeO_3$. The grains in these systems exhibit faceted structure due to the presence of defects and disordering. The DTA curves exhibit two reversible peak one around 370 and another around 730 °C which corresponds to Neel and Curie temperature, respectively. The transformation of Fe^{3+} into Fe^{4+} leads to weight gain in TGA. The TEC of this series varies in the range of 9.3 - 10.1 $\times 10^{-6}$ $°C^{-1}$. The conductivity in both BSF and BCF system increase with increase in substituent concentration up to x=0.50 after that decreases. The BSF system exhibits high conductivity as compared to BCF system due to the high specific free volume and more disordering of the oxygen vacancies in this system.

$Bi_{1-x}A_xYO_3$ (A=Sr, Ca; $0.0 \leq x \leq 0.20$) system exhibit single phase cubic structure but only up to x=0.05 concentration for both Sr^{2+} and Ca^{2+} substitution. In this series, the neutrality is maintained only by creation of oxygen vacancies after aliovalent substitution. Absence of any band in Raman spectra of these samples confirms the cubic symmetry of BSY-05 sample. The FT-IR spectra of BSY system exhibit higher number of bands which clearly indicates that BSY system is more disordered as compared to BCY system. The secondary phases act as the grain inhibitors and also increase thermal stability. The TGA curves show the weight loss above 450 °C due to the sublimation of bismuth oxide and the generation of oxygen vacancies. The conductivity of the samples increase for Ca^{2+}/Sr^{2+} substituted $BiYO_3$ up to x=0.05 concentration and after that decreases for higher concentrations. The Arrhenius curves of these samples also exhibit two different slopes. The change in slope can be explained on the basis of intergrain-intragrain model and dissociation-migration energy model. The conductivity of these systems is lowest among all the studied samples i.e. 10^{-4} S cm^{-1} at 800 °C. The Cr doped series could not form the single phase even at very low concentration of substitution.

Overall, among all the series, it can be concluded that manganite and ferrite based systems exhibit the best properties for x=0.50 concentration of the substituents. The BSM-50 sample exhibits the highest conductivity 0.099 S cm^{-1} with CTE of 9.40 $\times 10^{-6}$ $°C^{-1}$. The maximum conductivity in this system can be attributed to the appropriate concentrations of electrons/holes and oxygen vacancies.

The interaction study between best conducting samples and most common electrolyte i.e. YSZ has also been carried out for different time periods. The XRD results show the presence of $SrZrO_3$ and ZrO_2 in BSM, $Ca_{0.8}Zr_{1.2}O_2$ and ZrO_2 in BCM, $SrZrO_3$ and ZrO_2 in BSF, $CaZrO_3$ and ZrO_2 in BCF systems. The volume fraction of these phases increases with the increase in the duration of heat treatment. The ferrite based systems are more reactive than manganite based systems due to the less stability of Fe in its higher oxidation state. The Ca^{2+} substituted systems are less reactive and show low diffusion as compared to Sr^{2+} substituted systems due to their smaller unit cell volume. The BCM sample show good adhesion with YSZ as compared to other systems.

6.2 Future Scope

After analyzing the results presented in this work, the following suggestions are recommended for the further investigations:

- The sample preparation plays very important role for obtaining the desired properties of the systems. Therefore, the effect of different atmospheres and temperature can be further investigated on the synthesis of these systems.

- The performance of the present studied systems should be tested in the variable oxygen partial pressures.

- The present studied samples should also be tested for their compatibility with other ceria and $LaGO_3$ based electrolytes.

- The interaction study between interconnects and present studied materials (cathode) should be performed to know their applicability as cathode materials.